POLITECNICO DI MILANO
School of Industrial Engineering and Information

Master of Science in Materials Engineering and Nanotechnology

Additive Manufactured Piezopolymer-Based Inertial Sensor

Supervisors: Prof. Alberto Corigliano
Dr. Valentina Zega
Dr. Roberto Bernasconi
Prof. Luca Magagnin

A Thesis Presented by:
Davood Hatami, matricola 897807
Hossein Nouri Hosseinabadi, matricola 895277

Academic Year 2020-2021

I am dedicating this thesis to all my beloved family members who have meant and continue to mean so much to me.
First and foremost, to my father who taught me the value of hard work. Although he is no longer of this world, his memories continue to regulate my life.
Next, to my mother. There is no any word to express my feeling about you just thanks for your endless love, sacrifices and prayers.
Last but not least, dedicating to my siblings with all love and appreciation especially to my sister having never left my side and provided her moral, spiritual and emotional supports.

ABSTRACT [ENG]

Nowadays additive manufacturing technologies are replacing the conventional subtractive based ones due to being more environmentally friendly, cost and time effective as result of donating the freedom to engineers to come up with optimal designs significantly reducing the materials consumption and the steps required in conventional processes to assemble different parts. Moreover, the dream of on-demand manufacturing is coming into reality by the recent developments in AM technologies. However, it has still remained a long pass for AM to be used also in micro-fabrication world due to the restrictions mainly caused by the minimum feature size achievable, the employed material diversity as well as the microstructure and the surface quality of the printed parts. In case of micro-functional device fabrication, it is faced with further limitations due to the fact that 3D printing technologies of functional materials, whereby the interaction with environment is achieved, have not been well developed so far. In this project, the main goal is, at least from curiosity point of view, to introduce the AM technologies as possible fabrication ones in MEMS world which is now mostly relied on silicon-based microelectronic industry where manufacturing of 3D structures is of difficulties and the designs should be restricted to planar ones.

To this end, proper designs for Z-axis and three-axis piezoelectric accelerometers as functional devices are introduced enabling us to combine stereolithography and inkjet printing to fabricate such devices. In fact stereolithography is used to print the designed prototypes to which functional layers of conductive electrodes along with a piezoelectric polymer are added by inkjet printing.

An experimental procedure is defined to verify the reliability of fabrication process by printing some preliminary samples with stereolithography on which all the functional layers are added. In addition, the materials and processes compatibility especially in post processing steps like annealing and polling are verified. Finally some suggestions for the future activities based on the experiences gained in this project are provided.

ABSTRACT [ITA]

Al giorno d'oggi le tecnologie di produzione additiva (Additive Manufacturing, AM) stanno sostituendo quelle convenzionali basate sulla sottrazione perche sono piu rispettose dell'ambiente, economicamente vantaggiose e piu efficienti in termini di tempo, grazie alla liberta che hanno i progettisti di elaborare progetti ottimali riducendo significativamente il consumo di materiali e le fasi richieste nei processi convenzionali per l'assemblaggio delle differenti parti. Inoltre, la produzione su richiesta sta diventando realta grazie ai recenti sviluppi nelle tecnologie AM. Tuttavia, e ancora molto difficile utilizzare tecniche di AM nel mondo della micro-fabbricazione a causa delle restrizioni causate principalmente dalla dimensione minima delle caratteristiche ottenibili, dalla diversita dei materiali impiegati, nonche dalla microstruttura e dalla qualita della superficie delle parti stampate. Nel caso della fabbricazione di dispositivi che utilizzano materiali funzionalizzati, si devono affrontare ulteriori limitazioni dovute al fatto che le tecnologie di stampa 3D di tali materiali non sono state finora ben sviluppate. In questo progetto di tesi, l'obiettivo principale e contribuire allâintroduzione delle tecnologie AM nel mondo dei MEMS che ora e completamente affidato all'industria microelettronica basata principalmente sul silicio dove la produzione di strutture 3D e molto difficile ed i progetti dovrebbero essere limitati a quelli planari. A tal fine, vengono progettati accelerometri piezoelettrici uni-assiali e tri-assiali come dispositivi funzionali che consentono di combinare la stereolitografia e la stampa a getto d'inchiostro per la loro fabbricazione. Il processo di stampa stereolitografico viene utilizzato per stampare i prototipi progettati a cui vengono aggiunti strati funzionali di elettrodi conduttivi insieme a un polimero piezoelettrico mediante stampa a getto d'inchiostro. Prima di passare al dispositivo finale, viene definita una procedura sperimentale per verificare l'affidabilita del processo di fabbricazione mediante la stampa di alcuni campioni preliminari con stereolitografia su cui vengono aggiunti tutti gli strati funzionali. Inoltre viene verificata la compatibilita dei materiali e dei processi soprattutto nelle fasi di post-elaborazione come la ricottura e il poling. Infine vengono forniti alcuni suggerimenti per le attivita future sulla base delle esperienze acquisite.

ACKNOWLEDGEMENT

We would like to thank the following people, without whom we would not have been able to complete this research, and without whom we would not have made it through our master degree! First and foremost, our supervisor Prof. Alberto Corigliano, whose insight and knowledge into the subject matter steered me through this research. We are forever indebted to you for your unwavering support.
Special thanks to Dr. Valentina Zega and Dr. Roberto Bernasconi, whose supports allowed our studies to go the extra mile. We can never pay you back for all the help you have provided us, the experience you have helped me gain by working for you and the precious time you spent making sure our thesis is always on track. Thank you so much!
We would also like to express my gratitude and appreciation to Dr. Raffaella Suriano and Fabio Segala who have supported us throughout this research project.

Contents

Abstract i

Acknowledgement v

1 INTRODUCTION 1

2 STATE OF THE ART 3
2.1 Accelerometers . . . 3
2.1.1 Capacitive Accelerometers . . . 3
2.1.2 Piezoresistive Accelerometers . . . 5
2.1.3 Piezoelectric-based Sensors/Actuators . . . 7
2.1.4 Thermal convective accelerometers . . . 13
2.2 Additive Manufacturing . . . 14
2.2.1 Stereolithography . . . 15
2.2.2 Inkjet Printing . . . 16

3 PROPER DESIGNS AND SIMULATION OF 3D-PRINTED ACCELEROMETERS 19
3.1 Mechanical Design and Simulation of Accelerometers . . . 20
3.1.1 Design Concept . . . 20
3.1.2 FEM simulation using COMSOL Multiphysics . . . 25

4 METHODOLOGY AND EQUIPMENT OF EXPERIMENTS 33
4.1 Materials . . . 33
4.2 Equipments . . . 34
4.2.1 Stereolithography 3D-Printer . . . 34
4.2.2 Fujifilm Dimatix Inkjet Printer . . . 35
4.2.3 Laser Profilometer . . . 36
4.2.4 Contact Angle Measurements . . . 36
4.2.5 Corona Surface Treatment Device . . . 38
4.2.6 Furnace . . . 38
4.2.7 Stereo-microscope and Scanning Electron Microscope (SEM) . . . 38

4.3 Methodology (of experiments) 38

5 RESULTS AND DISCUSSION 43

6 CONCLUSION AND FUTURE PROSPECTIVE 67

6.1 The Design Procedure 67

6.1.1 Designing a Cantilever 68

6.1.2 Z-axis Accelerometer 68

6.1.3 Three Axis Accelerometer 69

6.2 Fabrication Steps 69

6.2.1 Inkjet Printing of the Silver Electrodes 69

6.2.2 Inkjet Printing of the Piezoelectric Polymer 70

6.3 Prospective of the Project 71

Bibliography 73

List of Figures

2.1 Schematic picture of an accelerometer 4
2.2 Comb finger configuration of an accelerometer. 5
2.3 Schematic representation of how a Piezo-resistive transducer output signal is generated. 7
2.4 Polarization hysteresis of a normal ferroelectric polymer (dashed line) and a relaxor ferroelectric polymer (black line) [21] 9
2.5 The conformations of the P(VDF-TrFE) copolymer [21]. 9
2.6 Light emission from a cellular polymer during micro-plasma discharges [25]. 10
2.7 a) PVDF b) a simple model for a solid piezelectric material with positive and negative charges c) cellular ferroelectric polymer [25]. 11
2.8 Schematic diagrams of various piezoelectric ceramic/polymer composites [30]. 12
2.9 a) Schematic view of a thermal accelerometer [42], b) temperature distribution with and without acceleration [43]. 13
2.10 Classification of micro-AM processes [46] 14
2.11 Schematic of Stereolithography process [48] 15
2.12 a) schematic of bend mode print head, b) schematic of squeeze mode print head, c) schematic of push mode print head d) Schematic of shear mode print head [52]. 17

3.1 Cantilever Dimensions 20
3.2 Four-layers structure of cantilever beam. 21
3.3 Z-axis Accelerometer Geometry 22
3.4 Preliminary design of Z-axis accelerometer. 22
3.5 Conventional design [56]. 23
3.6 Position of the top electrodes on beams. 24
3.7 Tri-axial Accelerometer geometry and preliminary dimensions 24
3.8 a) first natural frequency = 403.72 KHz, b) second natural frequency = 734.6 KHz and c) third natural frequency= 734.86 KHz of preliminary designed tri-axial accelerometer. 25
3.9 First and second natural frequencies of Z-axis accelerometer with 250 um beam thickness 26
3.10 First and second natural frequencies of Z-axis accelerometer with 300 um beam thickness 26
3.11 First and second natural frequencies of Z-axis accelerometer with 350 um beam thickness 27
3.12 First and second natural frequencies of Z-axis accelerometer with 310 um beam thickness 27

3.13 Variation of Floating potential vs Beam width. 28
3.14 Variation of Natural frequency vs Beam width. 28
3.15 Variation of Displacement (Deflection) vs Body Load. 29
3.16 Variation of Floating potential vs Body Load. 30
3.17 Floating potential of 3.63 mV obtained for the first1st mode shape under a base excitation of 1g along Z direction 31
3.18 Floating potential of 1 mV obtained for the first1st mode shape under a base excitation of 1g along Z direction 31

4.1 Schematically process chains for fully 3D-printed piezoelectric polymer-based accelerometers. a) Substrate fabricated by SL, b) profile analysis via laser profilometer, c) Corona surface treatment and wettability behavior, d) printing bottom electrode, e) annealing of the bottom electrode, f) printing P(VDF-TrFE) film, g) annealing of the P(VDF-TrFE) film, h) printing top electrode, i) annealing of the top electrode. 34
4.2 Digital Wax Systems (DWS) 028J+ 35
4.3 FUJIFILM DIMATIX DMP-2850 INKJET PRINTER 36
4.4 CONTACT ANGLE MEASUREMENTS 37
4.5 a) Vertically SL 3D-printing, b) Horizontally SL 3D-printing of substrate. 39
4.6 Camera views of silver nanoparticle ink droplets. 40

5.1 Surface roughness parameters of horizontally printed sample. 44
5.2 Representing (a) Content and size of the reinforcing particles and (b) Elemental composition employed in THERMA DM500 resin. 44
5.3 (a) untreated sample CA= 81.9°(b) treated sample CA= 49.9°(c) treated sample CA= 27.6°(d) treated sample CA= 13.4° 45
5.4 Images obtained by Stereomicroscope for droplet arrays of silver ink on un-Treated substrate surface. 45
5.5 SEM images of continuous films boarders of (a) 1 layer and (b) 2 layers printed with 10KHz frequency and d=20 um on un-Treated substrate surface 46
5.6 Images obtained by Stereomicroscope for droplet arrays of silver ink on un-Treated substrate surface. 46
5.7 Images obtained by Stereomicroscope for droplets array of silver ink on Treated substrate surface. 47
5.8 The SEM images of continuous films boarders of 1-layer printed on (a) un-Treated and (b) Treated substrate. 47
5.9 Surface coverage for 1-layer of silver nanoparticle printed with 20 um and 40 um drop spacing for both un-treated and treated samples. 48
5.10 Surface coverage for 2-layers of silver nanoparticle printed with 20 um drop spacing for both un-treated and treated samples. 49
5.11 Effect of presence of large particles on the creation of micro-cracks. 49

5.12 SEM images comparing severity of micro-cracks on 1-layer and 2-layers printed films with 20 um drops spacing for both un-treated and treated samples. 50
5.13 Surface coverage for 3-layers of silver nanoparticle printed with 20 um drop spacing. . 51
5.14 Elemental composition employed in silver nanoparticle inkjet-printed. 51
5.15 a) Physical Properties of the 3 different solvents, b) Mixture of solvents with different P(VDF-TrFE) concentrations [55]. 52
5.16 Jetting waveform for printing PVDF solution. 54
5.17 Camera views of P(VDF-TrFE) solution droplets. 54
5.18 Measurements of the thickness, width and length of the P(VDF-TrFE) layer inkjet-printed on silicon-gold substrate after inkjet-printing 10 layers. 57
5.19 Measurements of the thickness, width and length of the P(VDF-TrFE) layer inkjet-printed on silicon-gold substrate after inkjet-printing 20 layers. 57
5.20 Inkjet-printed PVDF-TrFE layer cured at 140 °C for one hour and half. 58
5.21 Dimensions of 3-layers bottom silver electrode. 59
5.22 Dimensions of 3-layers bottom silver electrode. 59
5.23 Touched area by printhead due to upwards deflection of the beam. 61
5.24 a) Bottom supporter (3D view), b) Top holder (3D view) 61
5.25 Representing strange unpredictable area. 62
5.26 a) Beam A without scratch b) Beam B with scratch 63
5.27 Images of the printed first layer of bottom electrode taken by Fucial Camera of Dimatix device. 64
5.28 Images of the printed second layer of bottom electrode taken by Fucial Camera of Dimatix device. 64
5.29 Images of the printed third layer of bottom electrode taken by Fucial Camera of Dimatix device. 65

Chapter 1

INTRODUCTION

The history of MEMS, acronym of Microelectromechanical systems, goes back to the 50th decade when Richard Feynman gave a pervasive presentation at California Institute of technology trying to introduce a public challenge of fabrication of an electrical motor smaller than 0.015 of an inch by offering 1000 dollars to the first person. Microelectromechanical systems (Microsystems in Europe and Micromachines in Japan), known in US or micmachines, known in Japan, are both referred to multitask devices made of electrical and mechanical components, whose size ranges from some micrometers to some millimeters, which can interact with the external environment and create proper responses. In other words, from the functionality point of view, such micro-devices not only can sense mechanical, thermal, electrical, magnetic or even chemical inputs but also can affect the environment by providing the same controlled outputs. That is why in a single microdevice, there is the possibility of taking the advantage of having transducers, sensors and actuators. Such a complexity although makes it utilize experts from a wide variety of engineering disciplines, from design to manufacturing ones, donates it a power to find its way in overwhelming industrial and consumer applications from automotive, medical, communication to defense ones. Apart from the definition of the MEMS originating from its components nature, some regard the MEMS as a manufacturing process borrowed from microelectronic industry using IC-based batch fabrication technology. This conventional silicon-based micromachining process possesses its own pros and cons. Miniaturization is one the most important factors in MEMS industry in order to allow us embed many, in a general sense, functional components in a single micro-device, the thing which has been the human dream for decades. Relying on the developments in microelectronic industry, the manufacturing process which is based on bulk and surface micromachining to add layers or to remove selectively part of the silicon, reaching such tiny mechanical devices is well-known making the dream come into reality. In addition, the structural (mechanical for eg) and functional (electrical for eg) properties of the materials used, mostly silicon, suit well the MEMS

requirements. However, the silicon batch processing requires many steps including mask lithography, physical and chemical deposition/etching techniques done in clean rooms making it time consuming and costly. Besides, the fabrication of the real 3D objects is not possible, or better to say, is faced with many restrictions. That is the reason why the design of such devices should be restricted to be almost planar inducing complex structures when multifunctional devices are of interests. So why should not people think of emerging manufacturing technologies known nowadays as additive manufacturing or generally 3D printing to be employed in MEMS industry? In additive manufacturing technologies in contrast with conventional subtractive processes, the 3D objects could be obtained by adding material layer by layer. The power of additive manufacturing donates the designers a freedom to think of 3D objects without any concern regarding the geometrical complexities. Moreover, thanks to the technological developments in this area, restrictions in terms of materials are being overcome continuously. Therefore, using different 3D printing technologies like Stereolithography(SL), Fused Deposition Modeling(FDM), Selective Laser Melting(SLM), Electronic Beam Melting(EBM) and so on, a wide variety of materials from Thermosets, Thermoplastics, Metals, Glasses to Ceramics could be thought of for 3D-printing. However, in MEMS industry, additive manufacturing has not been well considered due to some reasons. First of all, in AM world, fabrication of submillimetric components with precise geometries is hard to achieve. In addition, the poor surface and microstructure of the fabricated parts make them almost useless when accurate functionalities are required which are the case in MEMS. Furthermore, 3D printing technologies of functional materials like piezoelectric polymers or ceramics, shape memory alloys and so on, considerably used in MEMS, have not been reliably developed. Therefore, in the few works in which people have tried to employ AM to fabricate sensors or actuators, further steps were required to add active layers to the components of the device.

In the present project, the aim is to introduce possible designs and manufacturing process making it possible to fabricate one type of the most pervasive MEMS in market called accelerometers by a proper combination of SL and inkjet printing technologies which could be called a fully printed accelerometer. The most challenging stage of this work is the design stage in which the restrictions originating the SL and inkjet processes in terms of compatibility of the two technologies, printed materials stability in post processing steps and minimum printable components in size, made it time consuming and tricky to design a prototype with a proper sensitivity and functionality. This project is one of the first to try to introduce AM in MEMS industry which could revolutionize both industrial and consumer products by significant reduction of the time and cost of the fabrication process although a long way there exist to replace conventional fabrication process with additive manufacturing to fabricate real micro-devices.

Chapter 2

STATE OF THE ART

MEMS and Additive Manufacturing

2.1 Accelerometers

Accelerometers are sensors used in widespread applications from, aerospace, defense, automotive, navigation, industrial to biomedical ones [1]. Accelerometers are able to sense static or dynamic accelerations via different transduction mechanisms leading to classification of such device to capacitive, piezoelectric, piezoresistive, tunneling and thermal convection based ones [2] which are discussed in details separately. The resolution and sensitivity of such micro-machined inertial sensors have always been taken the most important consideration [3].

2.1.1 Capacitive Accelerometers

In all capacitive accelerometers, the transduction mechanism is based on the displacement measurement of a large proof mass suspended with some beams, caused by application of an external acceleration which could be treated as an inertial force acting on the proof mass using the relative dynamics (Eq.2.1), leading to capacitance changes of a capacitor made of electrodes of movable plates connected to the mass (sometimes the proof mass itself plays the rule of one electrode) and fixed plates [4] (Fig.2.1).

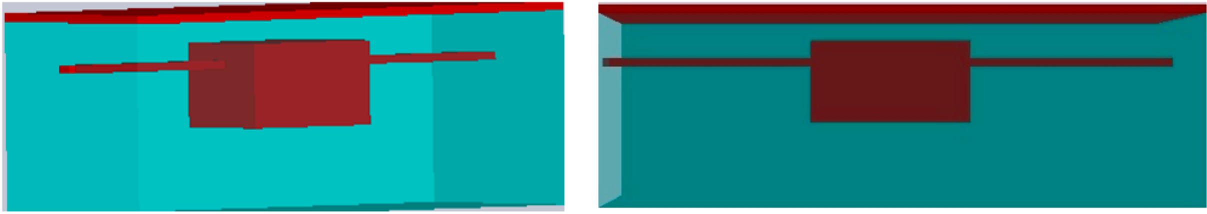

Figure 2.1: Schematic picture of an accelerometer

$$m\ddot{x} + c\dot{x} + k\dot{x} - F_{elec} = -ma \qquad (2.1)$$

x represents the displacement of the proof mass with respect to the MEMS box, k and c are the equivalent stiffness of the beams and dissipation coefficient respectively. Fig.2.1. is just a simplified schematic to show the working principle of capacitive accelerometer however the real devices need to be far more complex, in term of the design, due to the restrictions originating the micromachining fabrication process especially when multi-axis sensing is required [5,6]. The Fig.2.1. represents so called parallel plates sensing in which the capacitance change is the consequence of gap (between the two electrodes making the capacitor) variation. If a low displacement of the movable electrode is assumed when external acceleration is applied, the eq.1 could be linearized by defining an equivalent electrostatic stiffness (Kelec). Therefore, it can be shown that the sensitivity of a parallel plate capacitive accelerometer is given by (Eq.2.2):

$$\frac{\Delta C}{a} \alpha \frac{mS}{(k - k_{elec})d^2} \qquad (2.2)$$

In which S and d are the overlapping surface of the two electrodes and gap values respectively. However, due to the fact that the electrostatic force is a nonlinear function of the gap value, the eq.2.1 is not linear. Therefore, pull-in instability and consequent reliability issues related to the sticking problem should be considered in the design stage. In order to avoid the pull-in instability during the use, apart from the idea of using an electronic feedback [7,8], one might think of comb-finger capacitive accelerometers design [9] in which the gap between the electrodes making the capacitor is constant while the overlapping surface changes as the result of movable electrode displacement (Fig.2.2).

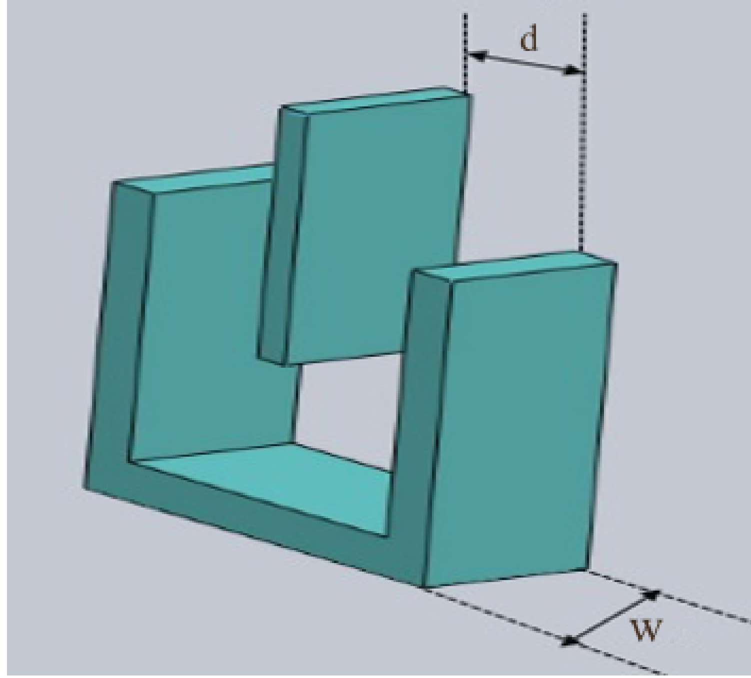

Figure 2.2: Comb finger configuration of an accelerometer.

For comb finger configuration, it can be shown that the electrostatic force, when a constant potential difference ϕ is applied between the capacitor plates while the middle plate is moving, is constant and given by:

$$F_{elec} = \frac{\varepsilon_0 \varepsilon_r w \varphi^2}{d} \tag{2.3}$$

Therefore nonlinearity is not involved in eq.2.1 avoiding the pull-in instability.

2.1.2 Piezoresistive Accelerometers

Generally, piezoresitance could be used as the basic concept for the design of many MEMS devices including sensors like tactile sensors, pressure sensors, accelerometers, and so on. Before going to the applications, a brief introduction of what piezoresistance concept is, could be beneficial.

2.1.2.1 Piezoresistance

Piezoresistance is defined as the change in electrical resistance of a part from which an electrical current is passing when it is subjected to mechanical deformation. Generally the electrical resistance of a conductive component, which is a function of both material properties and geometry, is equal to:

$$R = \rho \frac{L}{A} \tag{2.4}$$

ρ is the bulk resistivity, L and A are the length and cross section area with respect to charge flow direction respectively. From this simple well-known equation it could be deduced that the stress/strain application leads to resistance variation with so called two modes. Mode 1 represents the resistance variation due to dimensions changes. In second mode the resistance variation is due to the variation of resistivity with the applied strain. Generally speaking, the resistivity of the materials is a nonlinear function of strain however for small strain applications it could be assumed to have linear dependency. Although for all materials both modes are active, which one is dominant is the material specific. For instance in the case of metals the first mode and in crystals which are mostly used as piezoresistors in MEMS devices the second mode are dominant in such a way that the contribution of the other mode is neglected. For single crystal doped silicon piezoresistors the general relationship between resistivity and stress is express as:

$$\begin{bmatrix} \Delta\rho_{11}/\rho_0 \\ \Delta\rho_{22}/\rho_0 \\ \Delta\rho_{33}/\rho_0 \\ \Delta\rho_{23}/\rho_0 \\ \Delta\rho_{13}/\rho_0 \\ \Delta\rho_{12}/\rho_0 \end{bmatrix} = [\pi] \begin{bmatrix} \sigma_{11} \\ \sigma_{22} \\ \sigma_{33} \\ \tau_{23} \\ \tau_{13} \\ \tau_{12} \end{bmatrix} \tag{2.5}$$

In which π is a 6*6 matrix called piezoresistive matrix, σ and τ are normal and shear stresses respectively and ρ_0 is so called the isotropic resistivity of unstressed crystal. For 1 dimension resistance change, it can be derived that:

$$\frac{\Delta R}{R} = (1 + 2\nu + \pi E)\varepsilon \tag{2.6}$$

$$G = 1 + 2\nu + \pi E \tag{2.7}$$

ν , E, π are the Poissons ratio, modulus and piezoresitive coefficient respectively. ϵ is the applied strain and G is called gauge factor.

2.1.2.2 Application of Piezoresistors

Generally, in all MEMS devices and sensors whose design is based on piezoresistive tranducers, a piezoresistor is strained as a result of applied force or stress leading to change in the resistance of the piezoresistor. Usually in such devices the electrical resistance of the resistor is not sensed directly. Instead, the piezoresistors are parts of an electrical circuit configuration called Wheatstone bridge which is connected to a constant voltage [10]. When a mechanical input is applied, the current in the bridge circuit changes producing an output voltage which is proportional to the applied force/stress (Fig.2.3).

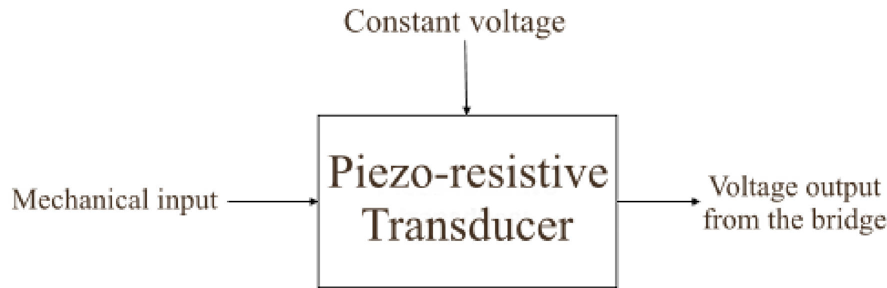

Figure 2.3: Schematic representation of how a Piezo-resistive transducer output signal is generated.

The piezoresistive concept has been considered in a wide variety of studies to design and fabricate accelerometers, to sense static or dynamic loads for different applications, due to reliability, acceptable resolution and sensitivity, low cost well-known silicon-based fabrication process as well [11, 12, 13, 14]. Apart from devices based on doped silicon piezoresistors, in some studies other piezoresistors, like SiC, have been used to fabricate accelerometers for specific demands like improved performance in extreme impact, high temperature and high electromagnetic field environments [15]. Due to outstanding material properties in harsh environment silicon carbide is being considered as an alternative for Si to design MEMS [16].

2.1.3 Piezoelectric-based Sensors/Actuators

Generally, due to achievements in miniaturization of piezoelectric components during the last decades and the possibility of piezoelectric materials integration in thin film forms along with metals and semiconductors, there have been a growing trend in design and fabrication of MEMS actuators and sensors based on such materials [17]. Before going to the application of piezoelectric materials in MEMS devices, it is noteworthy to have a brief introduction of what is piezoelectricity and the piezoelectric materials.

2.1.3.1 Piezoelectricity

Piezoelectricity that is the character of some specific materials, is a direct transduction mechanism in which mechanical and electrical signals are converted to each other. In other words, piezoelectric materials are described by constitutive laws in which the elastic and dielectric contributions are coupled to each other which are in contrast with non-piezoelectric materials for which separate elastic and dielectric constitutive laws should be considered. Hence, if the material is strained, electrical charges on opposite faces of the material are created, called direct piezoelectric effect, and under an electric field application the material is strained, indirect piezoelectric effect. Most of the piezoelectric materials are crystalline solids with non-symmetric perovskite structure in which, in unit cell, the center of positively and negatively charged elements do not coincide. The standard form of constitutive equation for piezoelectric material in a compact matrix form is represented as follows:

$$\begin{bmatrix} S \\ D \end{bmatrix} = \begin{bmatrix} s^E & d^t \\ d & \varepsilon^T \end{bmatrix} \begin{bmatrix} T \\ E \end{bmatrix} \tag{2.8}$$

S and D are strain-charge displacement respectively. T and E are the stress and electric field tensors respectively. d is called coupling third rank tensor whose elements determine how strong the electro-mechanical coupling is, in a given piezoelectric material. The direct and converse piezoelectric d tensor is defined as [18]:

$$d_{ij} = {}^{\partial D_i}\!/_{\partial T_j} = {}^{\partial S_j}\!/_{\partial E_i} \tag{2.9}$$

In general there are four ways to define piezoelectric tensors d, g, e and h used for specific purposes which can be defined as follow;

$$e_{ij} = {}^{\partial D_i}\!/_{\partial S_j} = -{}^{\partial T_j}\!/_{\partial E_i} \tag{2.10}$$

$$g_{ij} = -{}^{\partial E_i}\!/_{\partial T_j} = {}^{\partial S_j}\!/_{\partial D_i} \tag{2.11}$$

$$h_{ij} = -{}^{\partial E_i}\!/_{\partial S_j} = -{}^{\partial T_j}\!/_{\partial D_i} \tag{2.12}$$

2.1.3.2 Piezoelectric materials

Some piezoelectric materials even could be found in nature going under the name of naturally-occurring crystals like Quarts, tourmaline, sodium potassium tartrate. Also there are piezoelectric ceramics sintered from fine powder mixture made of ferroelectrics of the oxygen-octahedral type like PZT (PbZrTiO3), PT (PbTiO3). The main focus is going to be taken to the piezoelectric polymers due to the fact that one type of piezoelectric polymers has been used in this project to fabricate a printed accelerometer.

2.1.3.3 Piezoelectric polymers

Although the technology of piezoelectric polymers has been dominated by ferroelectric PVDF (polyvinylidene fluoride) and its copolymers, there are other less-known polymer based piezoelectric materials investigated in literature and even commercialized in real devices by industry discussed in the following [19]:

Relaxor ferroelectric polymers: The concept of relaxor ferroelectrics was introduced in 1998 in a seminar by Q. M. Zhang [20]. Introduction of relaxor ferroelectrics aimed to overcome the limitations in traditional ferroelectric polymers in terms of low responses to external stimulus such as low strain level (below 0.1) and low sensitivity to mechanical excitation making them practically inefficient to be used in real devices. Although for the most ferroelectric materials such responses considerably increase if working near ferroelectric-paraelectric transitions, the temperature range for such transitions is relatively narrow and often large hysteresis is involved. Zhang observed that by introducing defects

into the P(VDF- TrFE) copolymer by electron irradiation the normal ferroelectric behavior is turned into the relaxor ferroelectric behavior (Fig.2.4) [21].

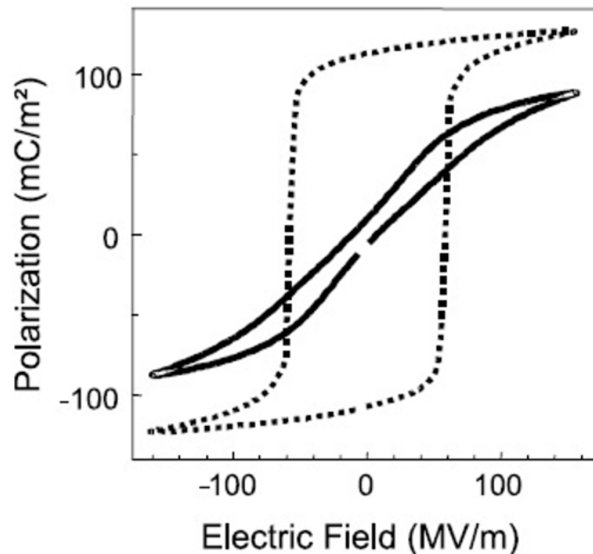

Figure 2.4: Polarization hysteresis of a normal ferroelectric polymer (dashed line) and a relaxor ferroelectric polymer (black line) [21]

In fact, although ferroelectric-paraelectric phase transition (all trans chains to trance gauche ones) (Fig.2.5) occurring in P(VDF-TrFE) copolymers involves large lattice strain, it is always faced with large hysteresis originating the energy barrier required to overcome when polarization direction change is needed [22, 23], the phenomenon which can be suppressed by introducing defect into the copolymer.

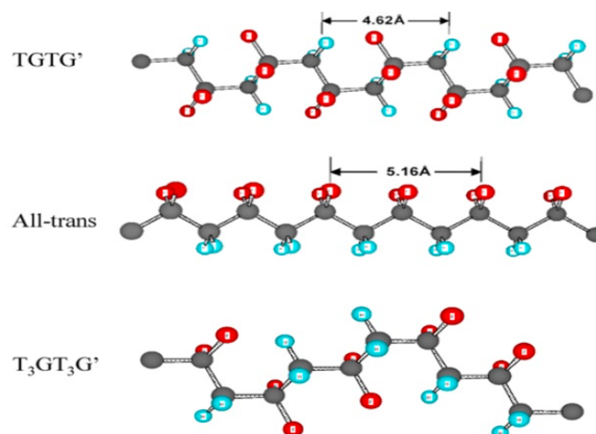

Figure 2.5: The conformations of the P(VDF-TrFE) copolymer [21].

Recently, a new type of relaxor ferroelectric polymers has been introduced, terpolymers of P(VDF-TrFE-CFE) and P(VDF-TrFE-CTFE), in which modification of the defects is achieved by randomly inserting a third monomer inducing the relaxor ferroelectric behavior to the polymer [24]. For terpolymers the electrostrictive strain can reach more than 7 percent making them very effective materials to be used in sensors and actuators.

Cellular polymers electrets: Conventionally, the polymeric foams were used as mechanical dampers, packaging materials due to being soft, light weight and perfect insulating character [25]. However, surprisingly it was found that such foams could be used as functional materials and electromechanical transducers if they are internally charged by micro-plasma discharges inside the voids [26]. In Fig.2.6, light emission from internally charged cellular polymers can be observed.

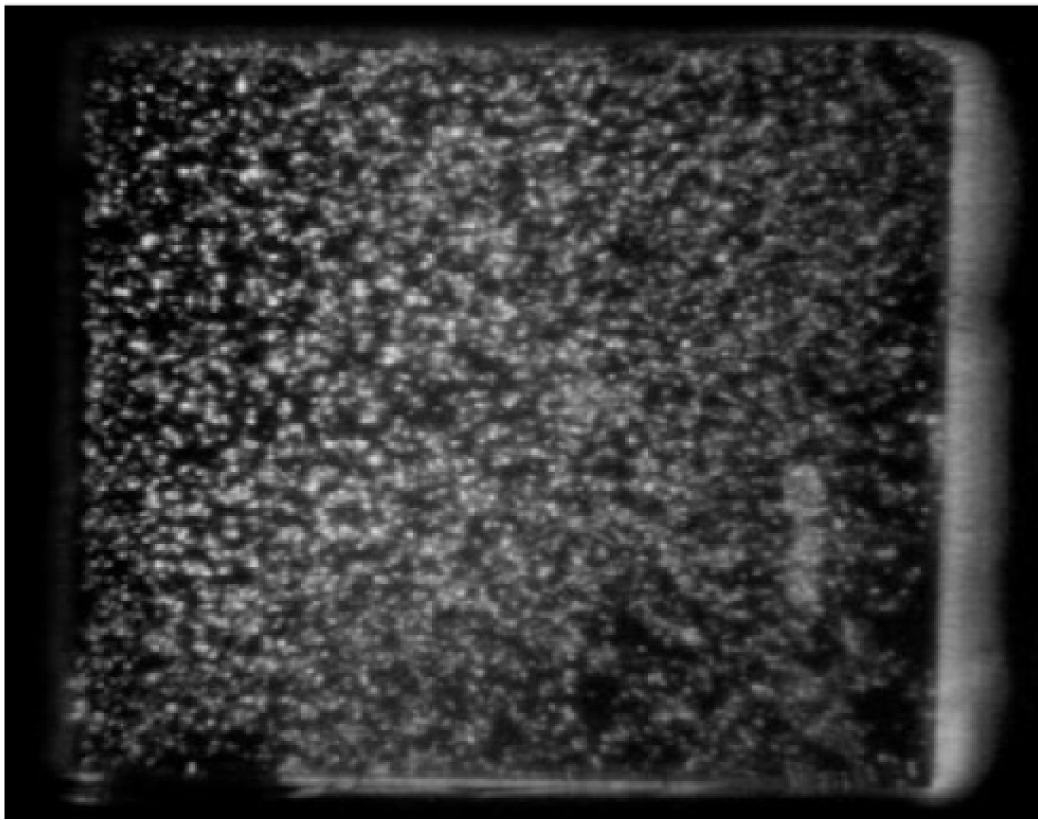

Figure 2.6: Light emission from a cellular polymer during micro-plasma discharges [25].

Surprisingly enough, the behavior of the charged polymeric foams is very similar to ferroelectric materials characterized by having permanent dipoles expressing piezoelectric character. With a simplified model (Fig.2.7.), it can be shown where the piezoelectric property of the charged cellular polymer originate.

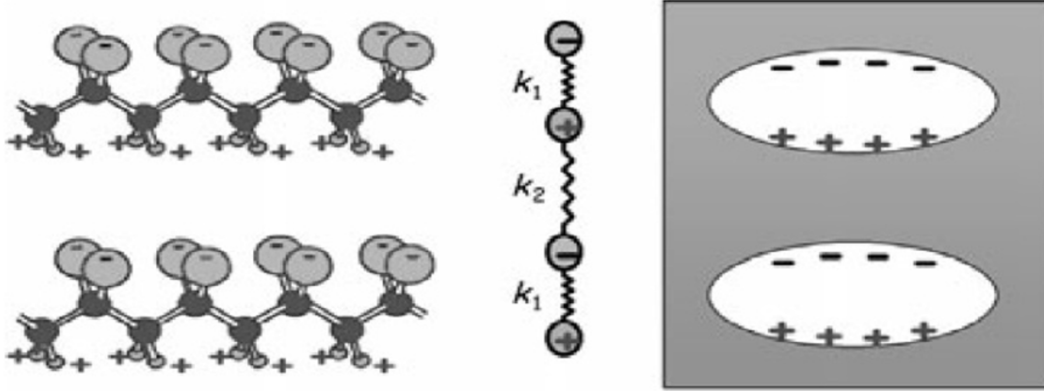

Figure 2.7: a) PVDF b) a simple model for a solid piezelectric material with positive and negative charges c) cellular ferroelectric polymer [25].

In a real ferroelectric material, it could be assumed that the negative and positive charges are connected to each other via springs with different force constant. Taking into account the definition of the piezoelectric coefficient e, it could be shown that it is equal to:

$$e = \frac{\partial T}{\partial E} = \frac{nqa(k_2 - k_1)}{2(k_2 + k_1)} \tag{2.13}$$

In which n, q, and a are the density of dipoles, charge of the particles and the unit cell length respectively. K1 and K2 are the force constant. Therefore, using this simplified model the presence of the piezoelectric coefficient is a consequence of difference in force constant of the springs connecting the charged particles. In polymeric materials this difference could be justified as the presence of different bonds in chains and inter-chains for example covalent bond and van der Waals interactions. The same model could be realized for cellular polymers due to the presence of voids in the matrix. If a tensile stress normal to the void direction is applied to the polymer, they are deformed more than the matrix leading to increase of the macroscopic dipole moment whereby the d33 coefficient can be understood. The other piezoelectric coefficients like d31 and d32 are also present due to unisotropicity involved by unisotropic voids. Using internally charged cellular polymers giant piezoelectric d33 coefficient of hundreds of PC/N could be achieved [27, 28, 29].

Piezoelectric polymeric composites: In real applications, the use of piezoelectric materials is faced with considerable restrictions due to conflicting desires in terms of mechanical and electromechanical properties expected from a transducer. That is why people started thinking of piezoelectric ceramic/polymer composites providing sufficiently high electromechanical coupling coefficients along with flexibility. The most important parameter in these composites is microstructural arrangement of the different phases [30]. Therefore, different structures have been investigated to try to reach the best favorable parameters some of which are schematically shown in Fig.2.8.

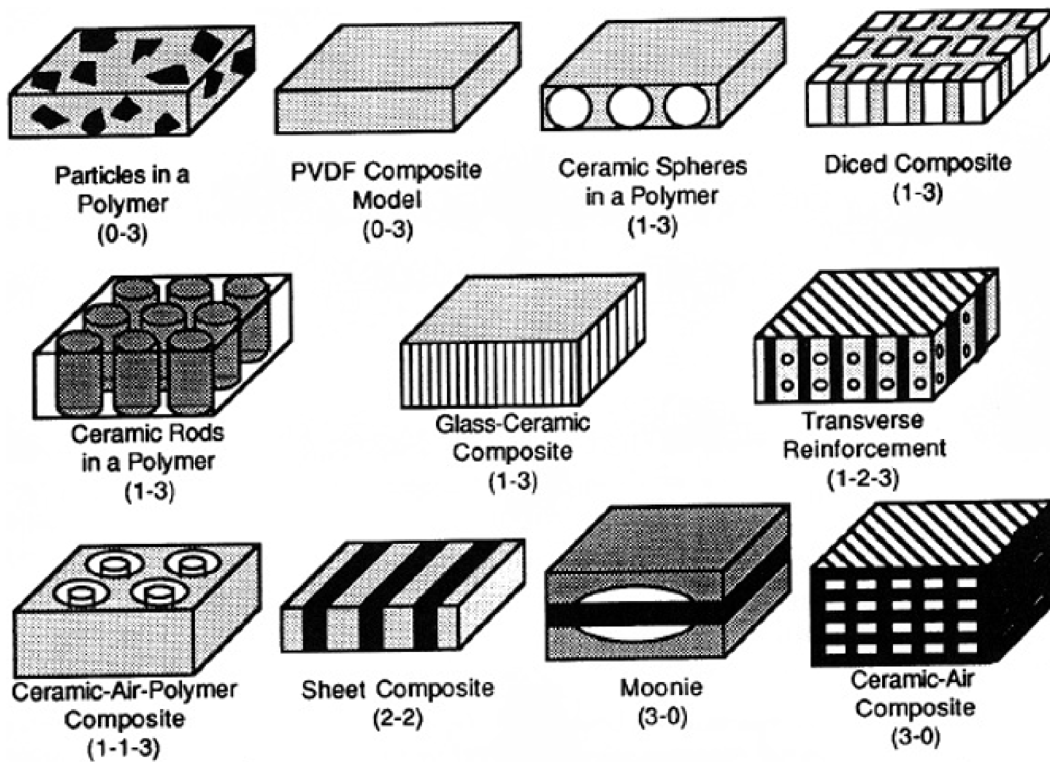

Figure 2.8: Schematic diagrams of various piezoelectric ceramic/polymer composites [30].

Furthermore, sometimes fillers are used to modify the properties of ferroelectric polymers. For instance in some studies ceramic particles are added to PVDF or its copolymers matrix to enhance the electromechanical coupling coefficients by inducing a polar phase to the polymer (so called beta phase) and to increase the thermal stability of the polymer [31,32,33].

Piezoelectric polymers in MEMS: MEMS devices based on polymeric transducers are of huge consideration due to flexibility, biocompatibility, low cost and easy processability compared to silicon based devices. That is why a long endeavor and investigations have been made to replace the inorganic piezoelectric materials with piezoelectric polymers. However, when use of piezoelectric polymers comes to reality different limitations should be considered. First of all, the life time of the devices is an important parameter restricting the use of polymers especially when working at elevated T is required. Furthermore, the electromechanical coupling in piezoelectric polymers is far less than that of inorganic piezoelectric materials [34]. In addition, pyroelectric coupling coefficients are an order of magnitude higher in piezoelectric polymers than that of inorganic ones making the device very sensitive to temperature variation. That is why if piezoelectric polymers are aimed to be used as sensors or actuators, one possibility is in robotics where precise temperature information is gathered by the machine. Recently, using an innovative method named selective pooling in ceramic/polymer

composites, people have tried to increase one effect (piezoelectricity for example) with respect to the other one (pyroelectricity) which is an important step to broaden the use of piezoelectric polymers [35]. Apart from the discussed limitations the flexibility and biocompatibility donated by use of polymeric materials to the device have motivated researches to design and fabricate sensors like force/pressure sensors, tactile sensors [36, 37, 38], inertia sensors [39] and harvesters [40] with polymers.

2.1.4 Thermal convective accelerometers

One the most important drawbacks of the discussed type of the inertia sensors is the need to incorporate a proof mass to the structure to tune the natural frequency and to increase the sensitivity of the device. The need to have a large proof mass not only gives rise to the device size increment but also introduce susceptible sites for crack creation and propagation especially in the regions where the proof mass is attached to the structure strictly restricting the life time of the device. At least from a curiosity point of view and for understanding of how interestingly different physics and transduction mechanisms have been employed in the MEMS world, it is noteworthy to have a brief introduction of so called thermal convective accelerometers working principle. The design of the thermal convective accelerometers is based on convective heat transfer done by a heated gas in a closed cavity which was first introduced by Leung [41]. So in principle there is not any need to have a seismic mass in the design. Moreover, the fabrication process which is based on silicon micromachining can be far more easily emplyed to manufacture thermal convective accelerometers reducing the cost considerably (Fig.2.9.) [42, 43]. From the figure, it is observed that the sensing mechanism is very simple. We have a sealed cavity made in a silicone substrate. The cavity is filled with a gas with a given pressure including two temperature sensors between which a heater is located. If there is not any applied acceleration, an equilibrated temperature profile is created inside the cavity. However when the device undergoes an acceleration, the equilibrium is perturbed and the temperature profile is shifted with respect to the acceleration direction leading to a temperature difference between the two temperature sensors which is proportional to the applied acceleration.

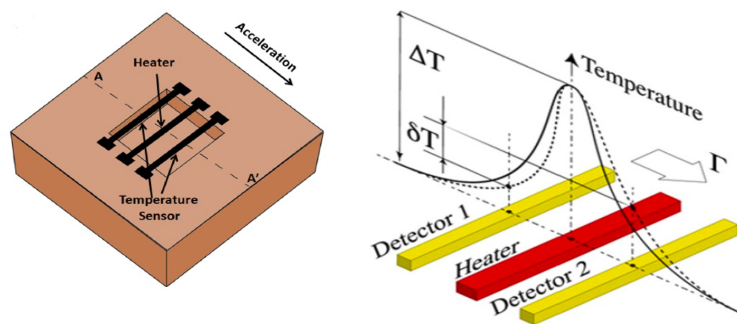

Figure 2.9: a) Schematic view of a thermal accelerometer [42], b) temperature distribution with and without acceleration [43].

2.2 Additive Manufacturing

The history of additive manufacturing goes back to 1980s, when people developed so called rapid prototyping in which 3 dimensional models were manufactured by layer by layer materials joining starting from a computer aided design [44]. In fact combination of three different technologies including computer aided design (CAD), Computer aided manufacturing (CAM) and computer numerical control (CNC) gives rise to additive manufacturing which in turn reminds an idea in contrast with that of conventional subtractive manufacturing processes. Additive manufacturing processes could be considered as more environmentally friendly than conventional manufacturing processes in addition to bringing about considerable time and cost reduction. Being environmentally friendly is deduced from some facts. First of all, AM provides a flexible technology allowing the manufacturers to have optimal designs for their products significantly reducing the material waste. Furthermore, any complex geometry component could be manufactured which implies that consolidation of previously separated parts is possible leading to the elimination of many steps and consequently to less energy consumption [45]. In addition, on-demand manufacturing that is a dream for manufactures gets feasible using AM. There are many studies pertaining to steps required to go from a CAD file to a real 3D manufactured structure including intermediate steps like transforming the CAD file in to a STL file understandable by a 3D printer machine. That is why it is better to directly focus more on the AM technologies which could be adapted or are dedicated to micro-fabrication. In general Micro-AM technologies could be classified into three groups. The process developed for fabrication of both macro and micro parts which are called scalable AM technologies, 3D direct writing technologies (3DDW) having been developed just for micro-parts fabrication and hybrid processes shown in Fig.2.10. [46].

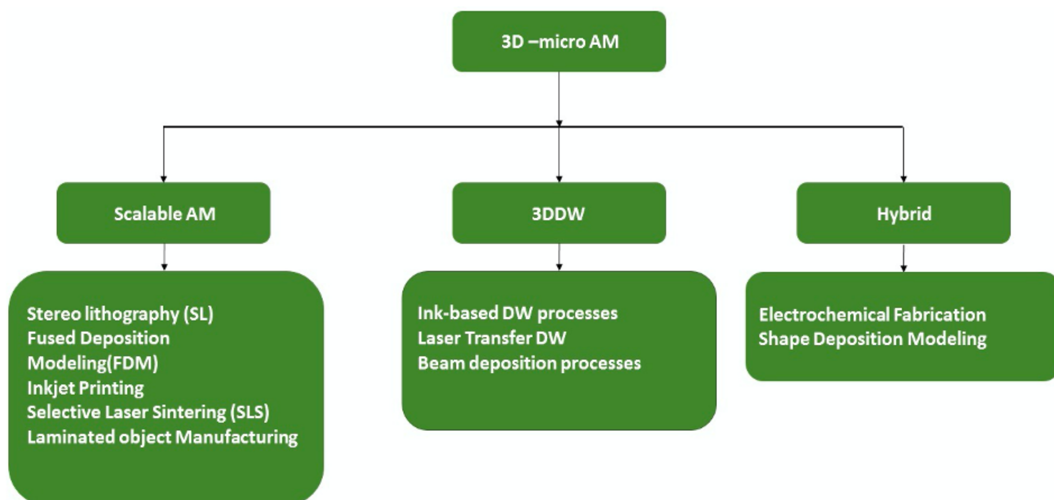

Figure 2.10: Classification of micro-AM processes [46]

Basically Direct Writing technologies were developed to create 2/2.5D patterns but they perfectly

modified then to fabricate real 3D objects of which laser chemical vapor deposition, focused ion beam DW are dedicated to 3D micro-AM. Also hybrid processes are those in which additive and subtractive fabrication methods are involved simultaneously. Here the main attention is taken to stereolitography and inkjet printing technologies which were used in manufacturing of the final accelerometer and in preliminary tests.

2.2.1 Stereolithography

Stereolithography is a powerful scalable AM technique developed in late 80th for rapid prototyping. It can be regarded as the first commercially available solid freedom fabrication technique [47] in which a photosensitive liquid resin is solidified via a spatially controlled photo-polymerization. In fact the polymerization is achieved when an ultraviolet laser is irradiated to the resin breaking the photo-initiator molecules and consequently a radical polymerization process is run. Polymerization is done point by point within a layer till the whole layer is solidified. Afterward the platform on which a layer of resin is supplied goes down and another layer of resin is solidified again until the whole part is fabricated. In Fig.2.11. the main parts of a stereolithography machine are shown [48].

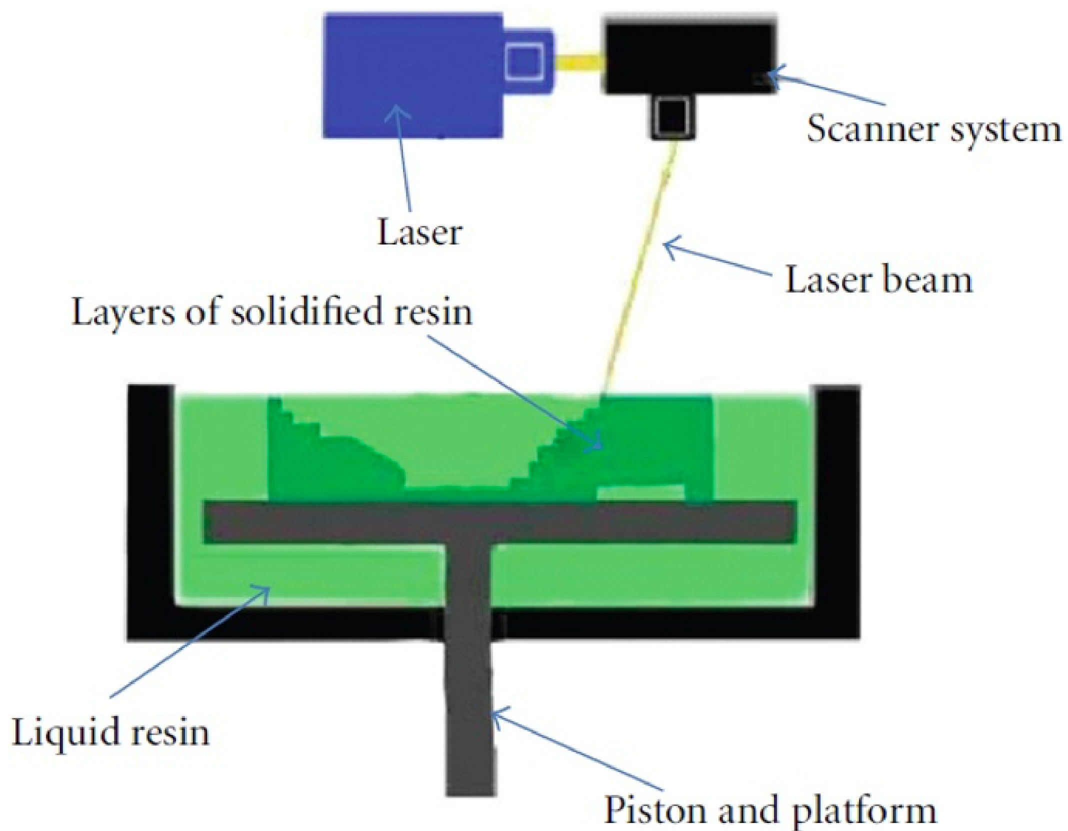

Figure 2.11: Schematic of Stereolithography process [48]

Stereolithography could be adapted to micro-fabrication process which is called micro-stereolithography (MSL) [49]. The MSL possesses the same working principle as SL however use of a laser with smaller spot size and optimized apparatus resulted in far better resolution and lower feature size. Generally there exist two main micro-stereolithography techniques named scanning and projection referring to the methods the UV light reaches photosensitive resin. In scanning MSL, a layer of the resin is built and solidified using point by point approach which is a time-consuming process. Conversely in projection MSL the whole layer is made by a single shot using a designed mask whereby the areas which should undergo solidification could be controlled. So the projection MSL reduces the fabrication time significantly. However, in the first generation of this MSL machines the process was not costly effective due to the needs to fabricate many masks. In order to solve this problem, many attempts were made of which was the possibility of using liquid crystal displays as a dynamic mask [50] whereby on/off pixels could be created. In MSL processes, the resolution achievable is restricted by the laser spot size. In order to reach better resolution people tried to introduce other applicable concepts such as so called two-photon stereolithography [51]. In two-photon SL exactly like SL, a photo-sensitive resin is solidified by light irradiation. However, in this case the photo-initiator requires absorption of two photons to create radicals, the process which is more probable near the center of laser spot where the light intensity is higher. Therefore, the polymerization is limited to very small area significantly increasing the resolution of the polymerization process.

2.2.2 Inkjet Printing

The birth of inkjet printing technology goes back to nineteenth century when Young (1805) and Laplace (1806) showed that formation of repeatable droplets from the liquid is governed by the laws of fluid dynamics. However, it took till 1931 to achieve a satisfactory explanation about droplet formation by application of a transient pressure pulse to a viscous liquid (Weber). The endeavors led to introducing the first commercial inkjet devices in 1952 by Elmqvist which were developed for medical applications [52]. Inkjet printing process as an additive manufacturing technology is based on layer by layer deposition of liquid materials in droplet forms. Then the droplets solidify by solvent evaporation, chemical reactions (crosslinking of the polymer by UV absorption) or cooling (crystallization). In general, there are two main technologies based on which the droplets are formed called drop-on-demand (DOD) and continuous inkjet (CIJ). In CIJ technology a series of droplets is formed by applying a force to the liquid jet. Then the droplets are charged by application of a high electric field and subsequently steered towards the desire location. The uncharged droplets are then recirculated through a defined rout. CIJ technology is more compatible for low viscosity liquids and due to restrictions of this technology, it is not usually used for printing of functional materials [53]. That is why the alternative technology of DOD was introduced in which the droplets are formed exactly when required and the necessary steps of CIJ were considerably reduced. In DOD inkjet technology the droplets ejection from some nozzles connected to the ink reservoir is caused by a pressure wave generated by an actuator. In general, two kinds of actuators could be considered, thermal and piezoelectric [54]. The thermal actuators are based on a resistor located inside an ink reservoir. The fast heating of the ink by the resistors creates a

bubble which expands and insulates the ink from the resistor. The volume increase caused by bubble expansion ejects the droplet from the nozzle. The requirement of having at least a volatile element in ink and also the possibility of materials degradation by thermal cycles, restrict considerably this technology application. However in piezoelectric actuators, there is no need to have a volatile ink and the pressure wave, in different modes (Fig.2.12), is generated by deflection of the reservoir wall caused by a piezoelectric material strain.

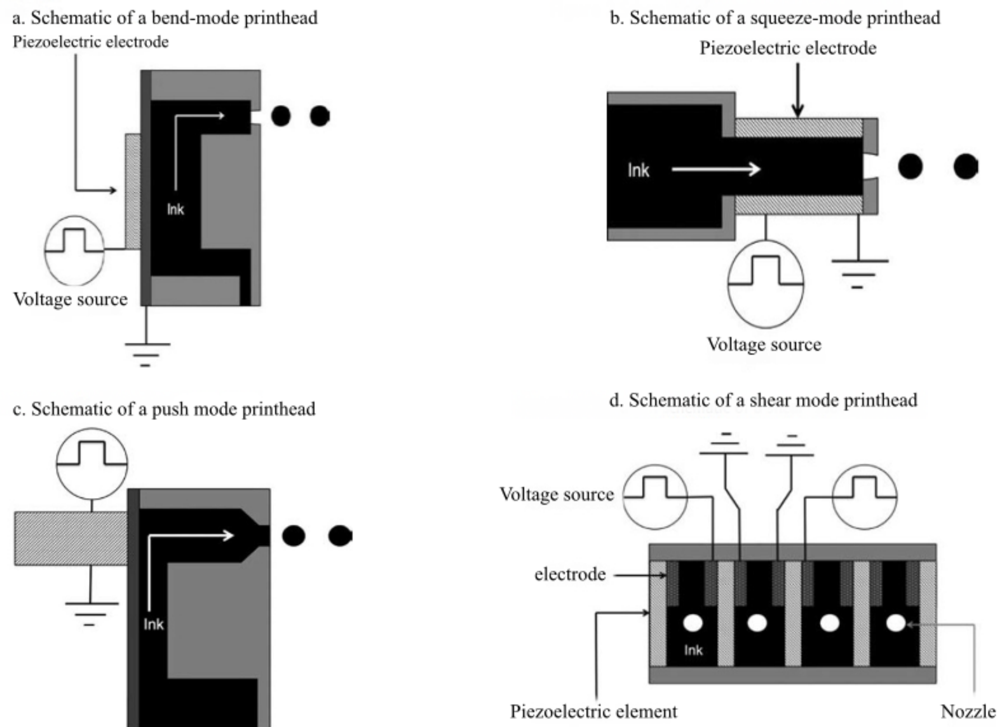

Figure 2.12: a) schematic of bend mode print head, b) schematic of squeeze mode print head, c) schematic of push mode print head d) Schematic of shear mode print head [52].

Inkjet printing technologies enable us to print selectively functional materials including DNA and proteins, Metal nanoparticles, polymer particles and etc making it of at most attention in biosensors, flexible and organic electronic, OLED devices and ETC.

Chapter 3

PROPER DESIGNS AND SIMULATION OF 3D-PRINTED ACCELEROMETERS

The main aim of this research is integration of Polymers and Additive Manufacturing (AM) techniques into Microsystems for sensing applications. Piezoelectric polymer-based accelerometers are supposed to be fabricated by using combination of Stereolithography (SL) 3D-printing and Inkjet Printing techniques. In fact, Stereolithography 3D-printing process is used to print a prototype with a new high working temperature resin and then a piezoelectric polymer thin film sandwiched between two silver electrodes is inkjet-printed to form the functional layers. Although Additive Manufacturing (AM) methods possess numerous advantages as compared with conventional ones, they still have major challenges/limitations including low surface quality and dimensional inaccuracy. In this study, since surface quality of the substrate 3D-printed by Stereolithography (SL) has a crucial role on inkjet printing of upper layers and eventually sensing functionality, coherent experiment chains were designed to verify behavior of the printed layers on the surface in addition to applying post-treatment to the 3D-printed substrates which are compatible with our specific material. In other words, to obtain optimum surface quality of the substrate in terms of both surface roughness and wettability behavior, we have 3D-printed our prototype with different conditions such as printing orientation in SL process and also applying post-treatment on the substrate. Moreover, characterizations for both sensing functionality, chemical analysis and surface morphology are performed. Materialographic characterization of substrate and different inkjet-printed layers is done using Scanning Electron Microscopes (SEM) in two study cases, untreated and treated substrate surfaces. SEM analysis shows the wettability behavior of silver nanoparticles ink (electrodes) and piezopolymer layers onto substrate surface in different timespan of corona surface treatment and also created cracks on inkjet-printed silver layers during heat treatment process. Finally, fabrication processes of the specific accelerometers based on the best experimental results are discussed. Before all, in order to assess reliability of the experimental measurements/results, Finite Element Analysis (FEA) is done using COMSOL Multiphysics version 5.5. It is also noteworthy

to declare that CATIA V5 and COMSOL software are used to design different layers and parts and then they are translated to other formats which are readable for Stereolithography (SL) 3D-printing and inkjet printing devices. Following subchapters cover Design and Simulation results. Then, Materials and Equipment are discussed in chapter.4 followed by Experiments Design and Process Preparation.

3.1 Mechanical Design and Simulation of Accelerometers

This section is devoted to the mechanical design and finite element simulation results of an electro-mechanical/piezoelectric Z-axis accelerometer and -most importantly- tri-axis accelerometer that are capable of producing out-of-plane displacements. The Multiphysics simulation and study of the electro-mechanical behavior of accelerometers were run in COMSOL Multiphysics version 5.5. In the Z-axis accelerometer case, it has an out-of-plane displacement 4.856 um in average and corresponding floating potential 5.2 mV for a base excitation of 1g. In the three-axis/tri-axial accelerometer case, floating potentials 3.63, 1 and 1 mV are obtained for the first three natural frequencies under a base excitation of 1g along Z, X and Y axes, respectively.

3.1.1 Design Concept

Both Z-axis and tri-axial accelerometers follow the simple basic concept of piezoelectric effect mechanism. First of all, design of the piezoelectric cantilever beam using piezoelectric polymer Poly(vinylidene fluoride) is described. As shown in Fig.3.1, a cantilever beam is designed in 10000*7000*310 um and anchor is designed in 17000*7000*2000 um with Young Modulus 3 GPa and possoins ratio 0.4.

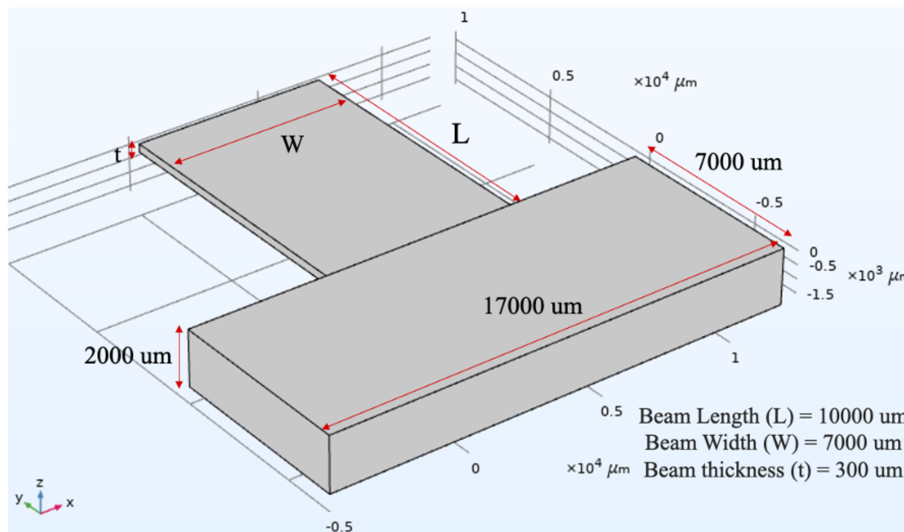

Figure 3.1: Cantilever Dimensions

Then, the bottom electrode, piezopolymer film and top electrode are designed over the substrate layer-by-layer (Fig.3.2).

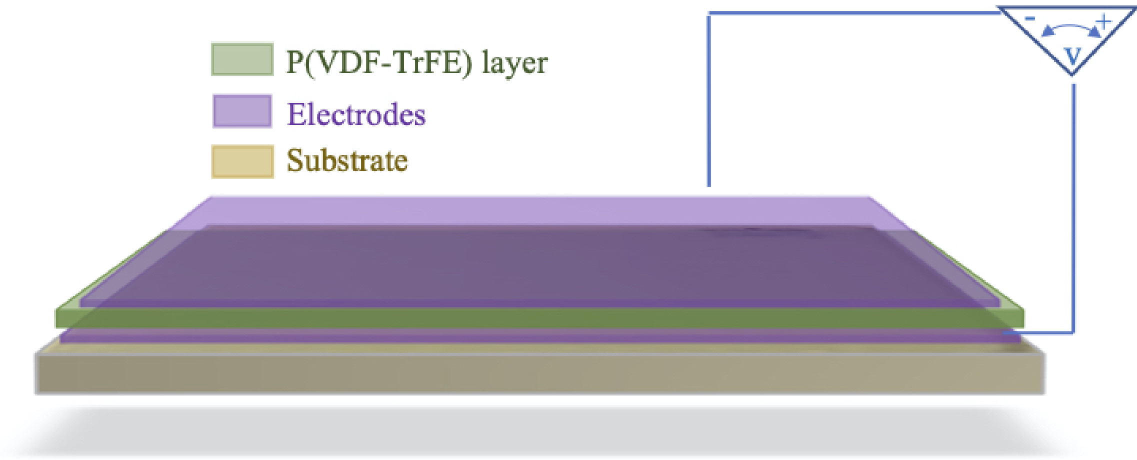

Figure 3.2: Four-layers structure of cantilever beam.

To assess the influence of the cantilever geometry on the achievable response, different cantilever beams with different dimensions were modeled; however, due to restrictions coming from inkjet printing process, optimum/final cantilever geometry is considered as shown in Fig.3.1. One of the main fundamental assessment done for cantilevers and MEMS devices (accelerometers) in finite element analysis is device deflection under its own weight. To this aim, final designed cantilever was analyzed under its own weight and deflection equal to 0.3033 um at room temperature was reported which is acceptable. In order to make a comparison between experimental and simulation results, it is necessary to define the parameters as close as possible to that of experimental ones. To fulfill this aim, material properties of P(VDF-TrFE) and silver nanoparticles are defined in finite element simulation according to material brochure purchased from Sigma-Aldrich and literatures.
In this research, just to check functionality of the printed and polled active layer, it is supposed to actuate manually the cantilever beam and then based on the applied load, an electric potential is obtained. On the way to the best design for Z-axis accelerometer, various designs were investigated/studied. The most important factor kept in mind during design step is compatibility with Stereolithography (SL) 3D-printing and Inkjet Printing processes. Two beams are attached to the proof mass, as shown in Fig.3.3, through two connectors which are capable of producing out-of-plane motion.

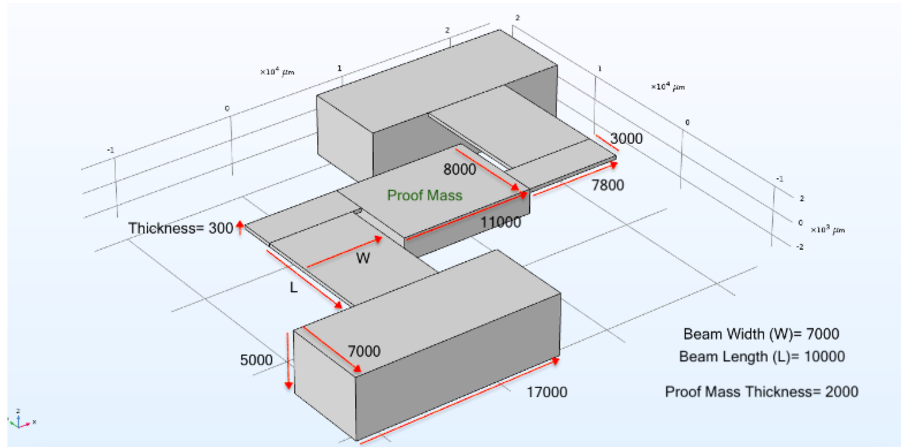

Figure 3.3: Z-axis Accelerometer Geometry

At the first stage of the design, the beams were located/positioned in the middle of proof mass thickness; however, inkjet printhead should have the least allowance distance from the working/printing area on the beams in order not to lose pattern precision. So, as seen in Fig.3.4, due to 850 um gap between top surface of the proof mass and working/printing area on the beams, this design cannot be an appropriate design.

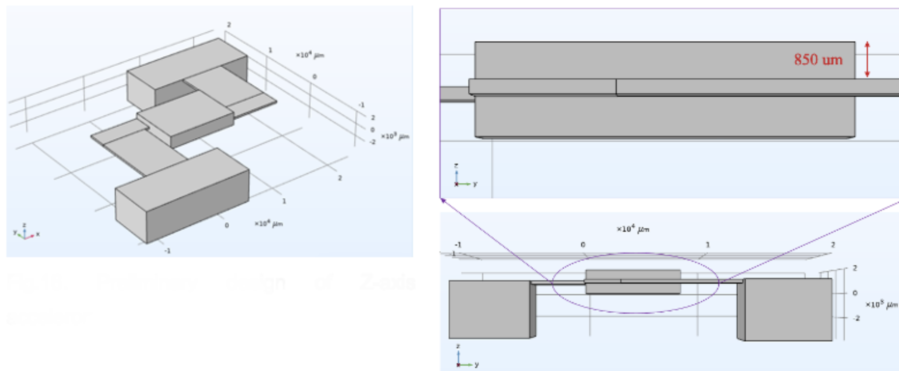

Figure 3.4: Preliminary design of Z-axis accelerometer.

Consequently, although with this design, an ideal natural frequency difference was achieved between first and second modes, accuracy and uniformity of the inkjet-printed layers were sacrificed. In the next stage, it was supposed to place the beams aligned with top surface of the proof mass. Fortunately, with this design not only accuracy and uniformity of the inkjet-printed layers are satisfied but also natural frequency difference between first and second ones is an acceptable value reported in subsection 3.1.2.1. Fig.3.3 illustrates schematically symmetric designed Z-axis accelerometer in its rest mode

and structural dimensions by which the bests results are achieved. One advantage of the presented configuration with respect to the conventional design (Fig.3.5) is that larger beams (almost equal to the length of the proof mass) can be exploited without significantly changing the overal size of the sensing device (accelerometer). Furthermore, larger deflections can be achieved exploiting this presented design in response to a given base excitation.

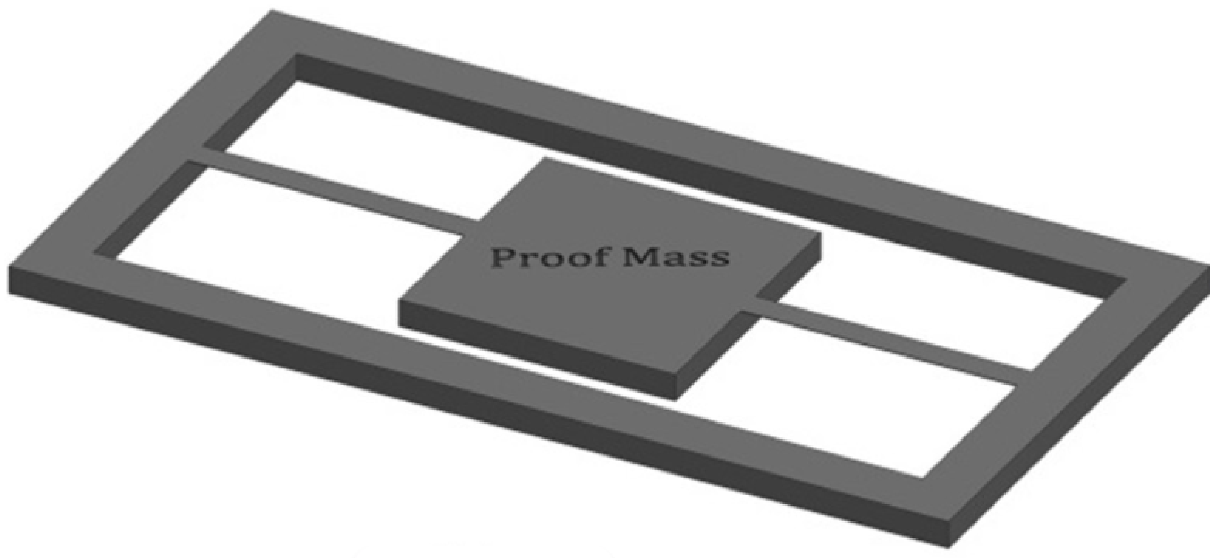

Figure 3.5: Conventional design [56].

The proof mass dimension is designed to be 11 * 8 * 2 mm made of THERMA DM500 resin. The thickness of the piezoelectric P(VDF-TrFE) layer is considered as 3 um. It is necessary to notice that length and width of the bottom electrode are different with respect to that of substrate (beam) and length and width of the top electrode also are different with respect to piezoelectric P(VDF-TrFE) layer from each side. In order to avoid short circuits, a gap of approximately 1000 um is considered in each side. As seen in Fig.3.6, the overall dimensions of the Z-axis accelerometer are 36.6, 32 and 5 mm.

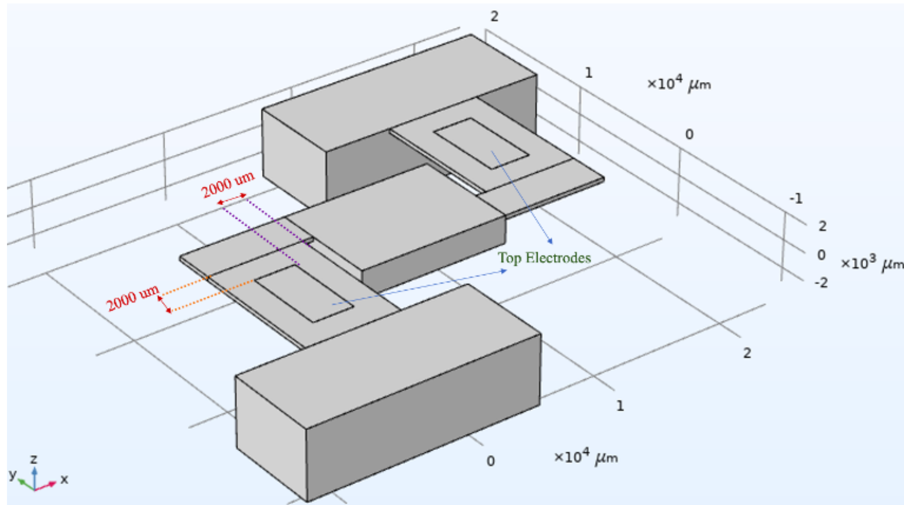

Figure 3.6: Position of the top electrodes on beams.

Also, the same story/explanation is true for the proposed tri-axial accelerometer but in this case/design, as shown in Fig.3.7, the proof mass of the structure is suspended by four cantilever beams.

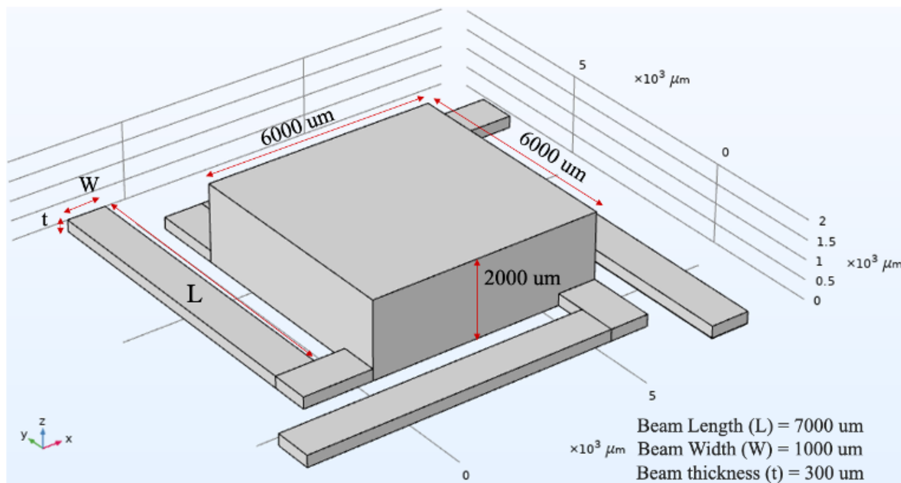

Figure 3.7: Tri-axial Accelerometer geometry and preliminary dimensions

These four beams are attached to the bottom portion of the proof mass. The reason why cantilever beams are attached to the bottom portion of the proof mass is that by this way, the center of mass of proof mass is not placed/levelized in alignment with constrained beams (Fig.3.7). Fig.3.8 (b, c) validate this fact so that second and third natural frequencies are assigned to rotation of the device (tri-axial

accelerometers) around X-axis and Y-axis when the device (tri-axial accelerometers) is stimulated in Y and X axes, respectively.

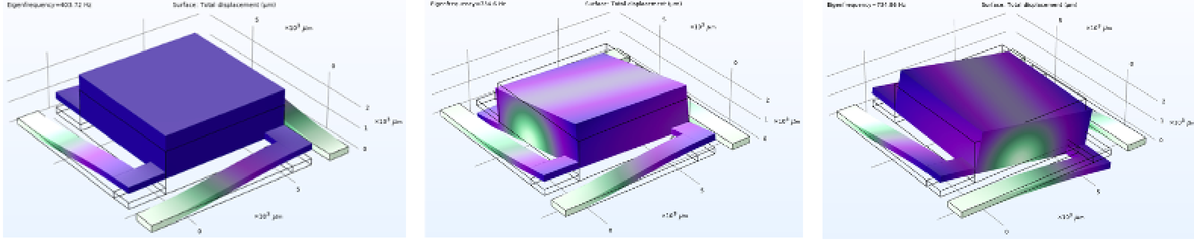

Figure 3.8: a) first natural frequency = 403.72 KHz, b) second natural frequency = 734.6 KHz and c) third natural frequency= 734.86 KHz of preliminary designed tri-axial accelerometer.

Schematically, symmetric designed tri-axial accelerometer (rest mode) and structural dimensions are presented in Fig.3.8. The proof mass is 6* 6* 2 mm. The thickness of the piezoelectric P(VDF-TrFE) layer is designed to be 3 um. Again, length and width of the electrodes have difference (approximately 1000 um in each side) with respect to that of substrate (beam) and piezoelectric P(VDF-TrFE) layer to avoid short circuits, respectively.

3.1.2 FEM simulation using COMSOL Multiphysics

3.1.2.1 OPTIMIZATION OF GEOMETRIC PARAMETERES

In order to obtain high sensitivity, geometric factors/parameters of accelerometers including beams, proof mass dimensions and also thickness of piezoelectric P(VDF-TrFE) thin film are numerically optimized taking into account fabrication process restrictions using COMSOL MULTIPHYSICS 5.5. It is proved that increasing the beam length, the displacement of the proof mass for a given acceleration increases; however, what determine the maximum length of beam in sensing devices is maximum authorized/allowable overall size of sensing/MEMS device and the time of inkjet-printing process of functional material. Hence, considering all the factors, the length of beam, in this study, is fixed to be 10 mm. Furthermore, since in-plane dimensions of the proof mass is almost equal to the length of beam, the dimensions of the proof mass are designed to be 11, 8 and 2 mm. The thickness of the beam strongly depends on fabrication process. Based on the Stereolithography process specifications, beam thickness was studied in range between 250-350 um to check if first natural frequency of the device (the desired one) has an acceptable difference with the second natural frequency. The results show that for 250 um beam thickness, first and second natural frequencies are equal to 169.91 KHz and 226.34 KHz, respectively.

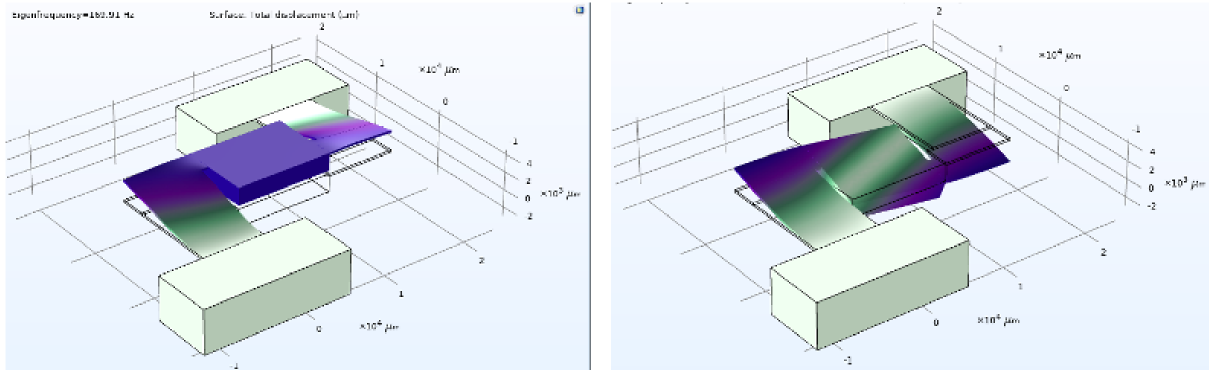

Figure 3.9: First and second natural frequencies of Z-axis accelerometer with 250 um beam thickness

For 300 um beam thickness, first and second natural frequencies are equal to 219.58 KHz and 289.16 KHz, respectively.

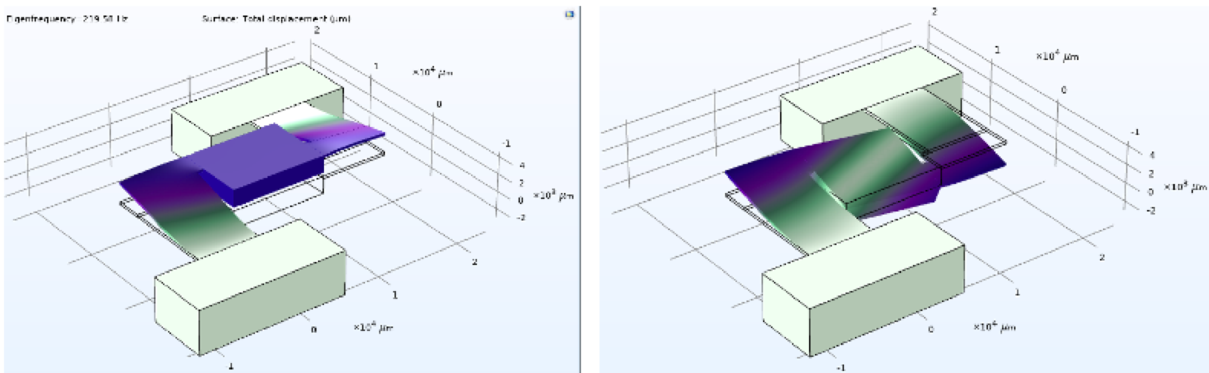

Figure 3.10: First and second natural frequencies of Z-axis accelerometer with 300 um beam thickness

Finally, for 350 um beam thickness, first and second natural frequencies are equal to 272.2 KHz and 354.46 KHz, respectively. Therefore, 56.5 to 82.3 KHz is an acceptable natural frequency difference

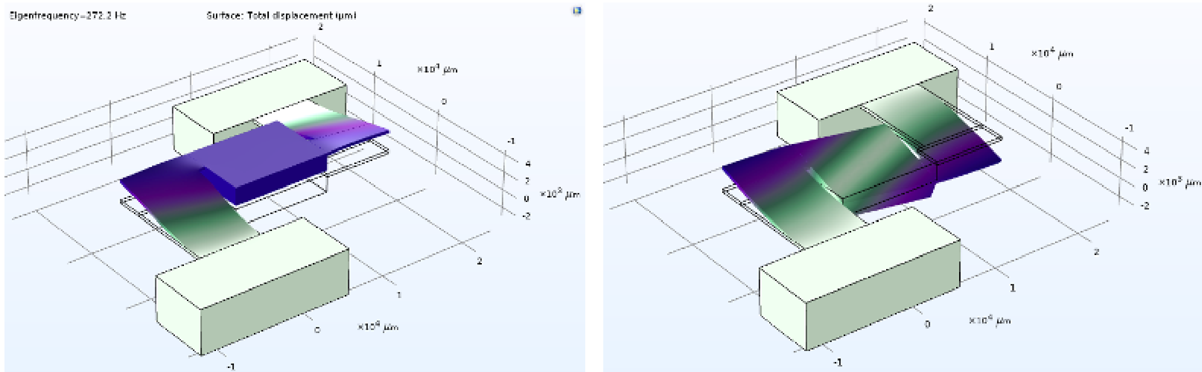

Figure 3.11: First and second natural frequencies of Z-axis accelerometer with 350 um beam thickness

Eventually, regarding the fabricated accelerometers by Stereolithography device, beams thickness is fixed to 310 um. Again, performing the analysis for beams thickness equal to 310 um, first and second natural frequencies were obtained 230.21 and 302.17 KHz.

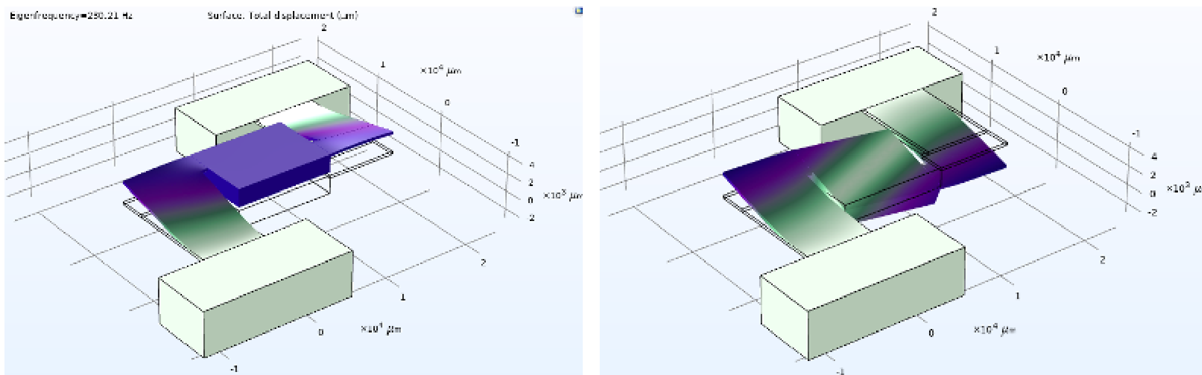

Figure 3.12: First and second natural frequencies of Z-axis accelerometer with 310 um beam thickness

Another geometric factor/parameter of beam required to be studied is beam width. In order to study the impact of beam width on sensing functionality, the length, thickness and width of the cantilever beam were initially designed as 10000, 310 and 5500 um, repectively. When beam width was numerically studied in the range from 5500 to 7500 um, it was found out that when the width of the cantilever beam increases in the range from 5500 um to 7500 um, the sensitivity decreases and the first order natural frequency increases with increase of width of the beam in Z-axis accelerometers.

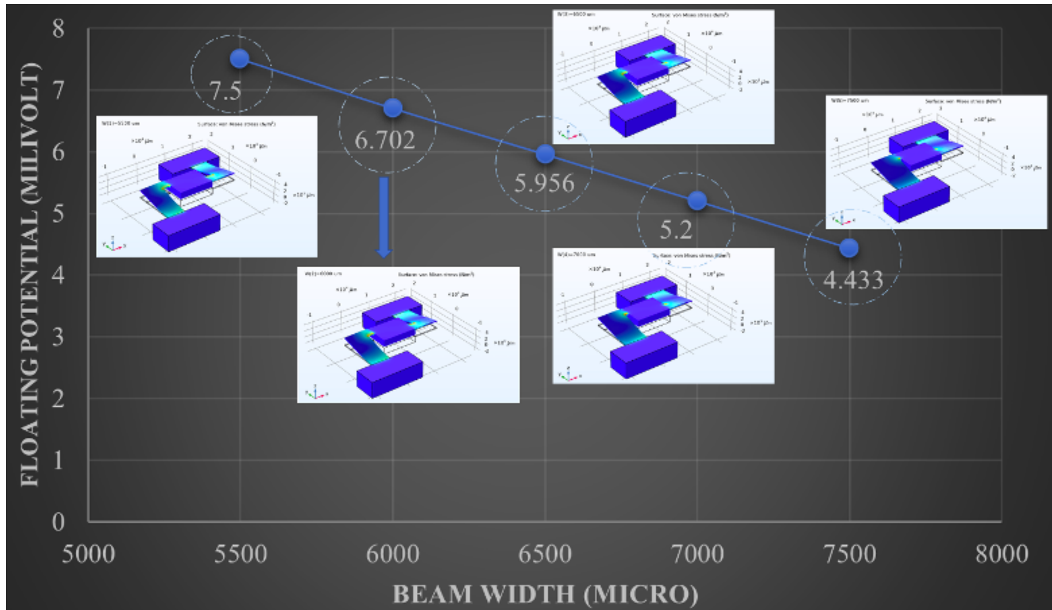

Figure 3.13: Variation of Floating potential vs Beam width.

From Fig.3.14, first natural frequency of Z-axis accelerometer for different beam width can be found out.

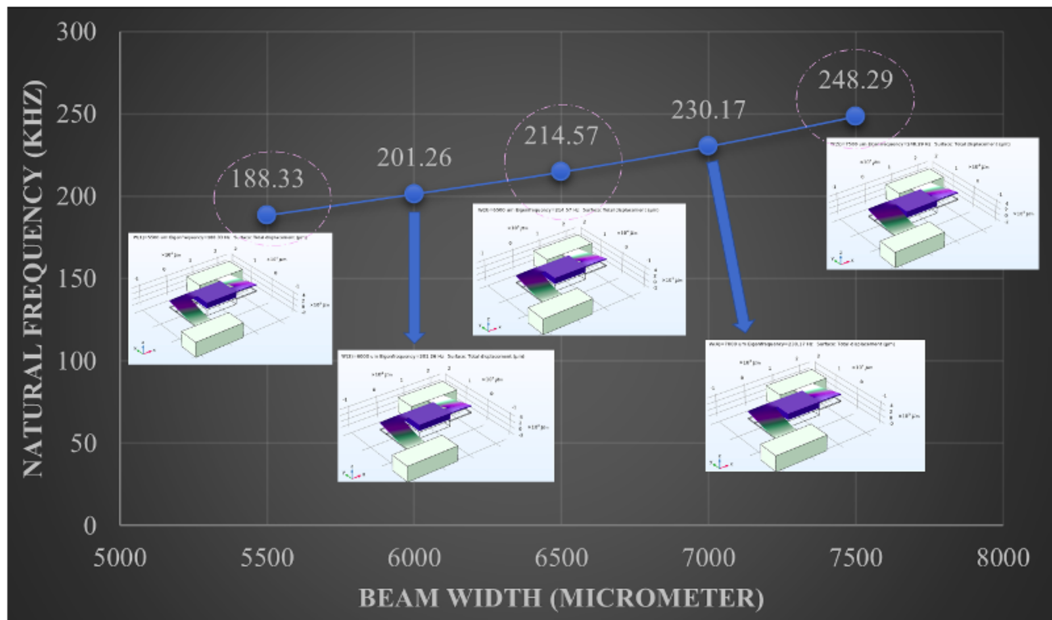

Figure 3.14: Variation of Natural frequency vs Beam width.

Therefore, from sensitivity point of view and device size, it is better to design beams with the least width; however, regarding the restriction of the inkjet printing process, the beams were designed to have width of 7 mm.

3.1.2.2 FEM Analysis of Z-axis Accelerometer

Static Analysis To analyze static behavior of the piezoelectric polymer-based Z-axis accelerometer, COMSOL Multiphysics software is employed. The Multiphysics study -the electrical and mechanical (electromechanical) behavior- is performed using Piezoelectricity physics/ Stationary study of COMSOL Multiphysics MEMS module. For finite element simulation of the designed Z-axis accelerometer, both cantilever beams are fully clamped from the sides which are connected to the anchors and all other boundaries are kept free to move. Body loads are applied knowing material density, whereby the designed Z-axis accelerometer was fabricated, in range between 1g to 5g, and the corresponding deflections (displacements) are calculated using static analysis. The results are shown in Fig.3.15.

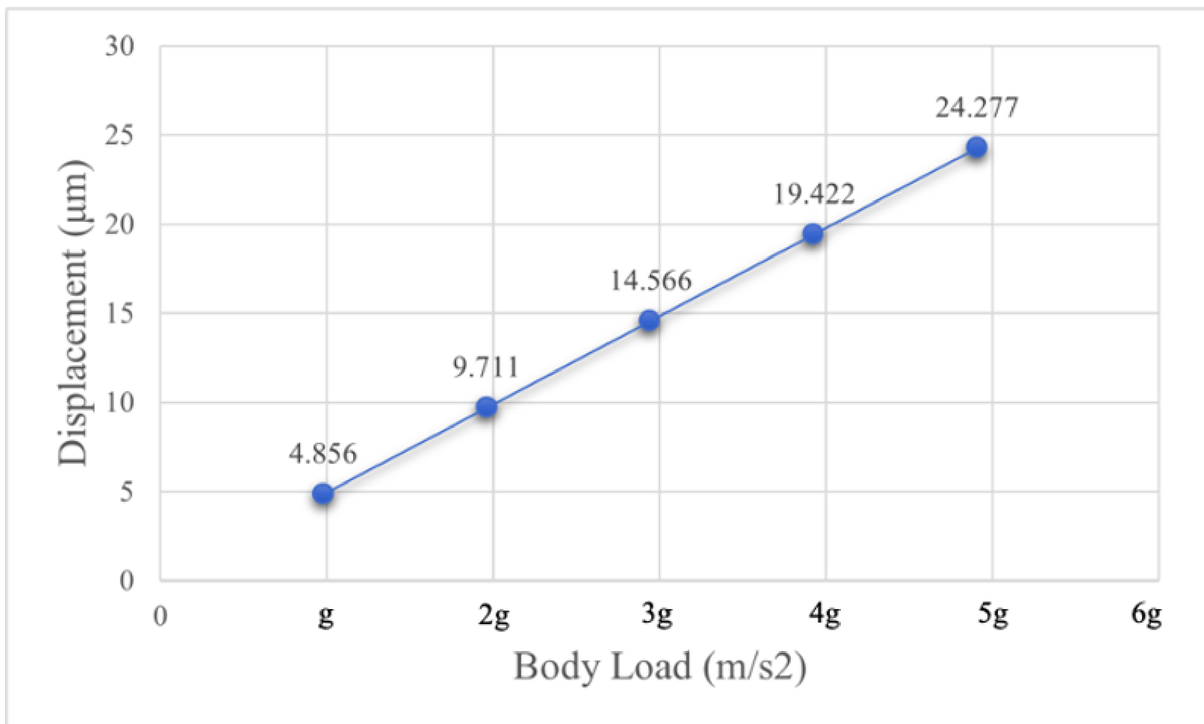

Figure 3.15: Variation of Displacement (Deflection) vs Body Load.

To study the voltage output of the piezoelectric elements of the Z-axis accelerometer, floating potential output results versus body loads are shown in Fig.3.16 and the results can be compared to experiments.

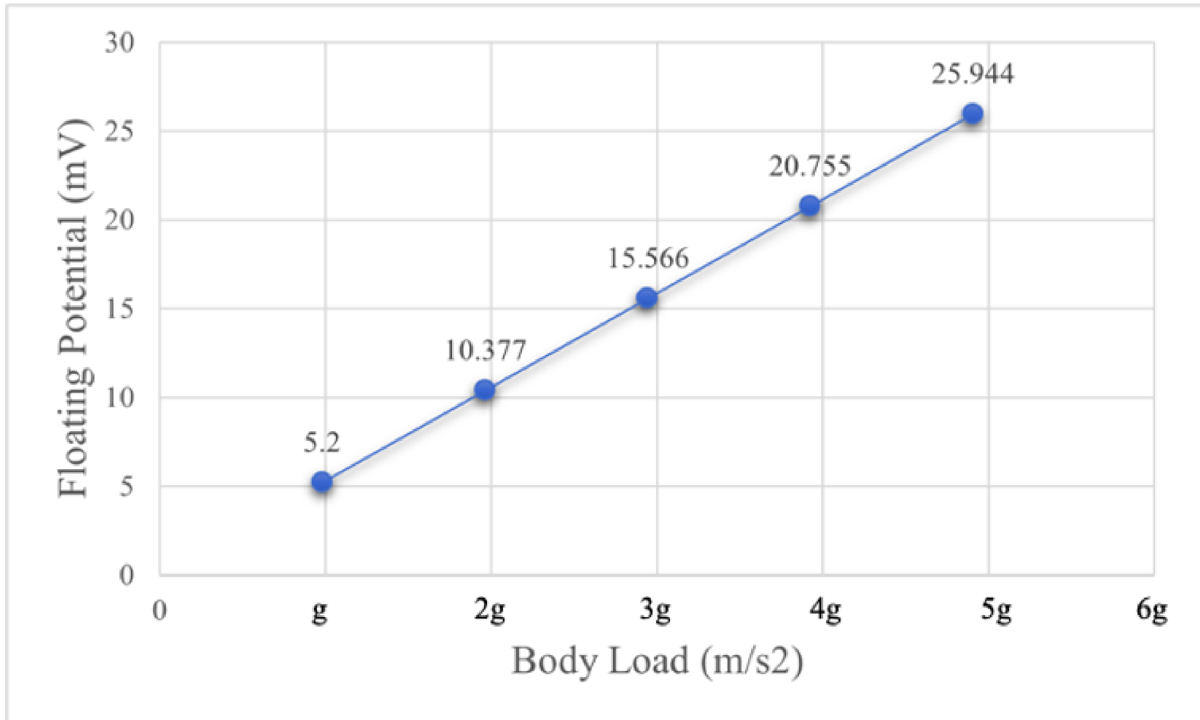

Figure 3.16: Variation of Floating potential vs Body Load.

As shown in Fig.3.15 and Fig.3.16, there is a linear relation between floating potential and displacement versus body load.

3.1.2.3 FEM ANALYSIS OF TRI-AXIAL ACCELEROMETER

Static Analysis To analyze the static behavior of the piezoelectric polymer-based tri-axial accelerometer, COMSOL Multiphysics software is used. The Multiphysics simulation is performed using Piezoelectricity physics/ Stationary study of COMSOL Multiphysics MEMS module. For finite element simulation of the designed three-axis accelerometer, shown in Fig.3.7, the ends of the cantilever beams are mechanically fixed to anchors and all other boundaries are kept free to move. Fig.3.7 shows the simulation results of the upward displacement of proof mass and four attached cantilever beams. Proof mass and four attached cantilever beams simultaneously move upward along Z axis, when the whole MEMS device is stimulated in Z direction (for example when an external acceleration of 1g acts in the z direction). Then, inertial force is applied to the beams and beams are deformed. Then, the piezoelectric polymer layer is strained. Due to electro-mechanical coupling effect, mechanical disturbance is switched to generation of electric field. As shown in Fig.3.17, a floating potential of 3.63 mV is obtained for the first mode under a base excitation of 1g along Z direction.

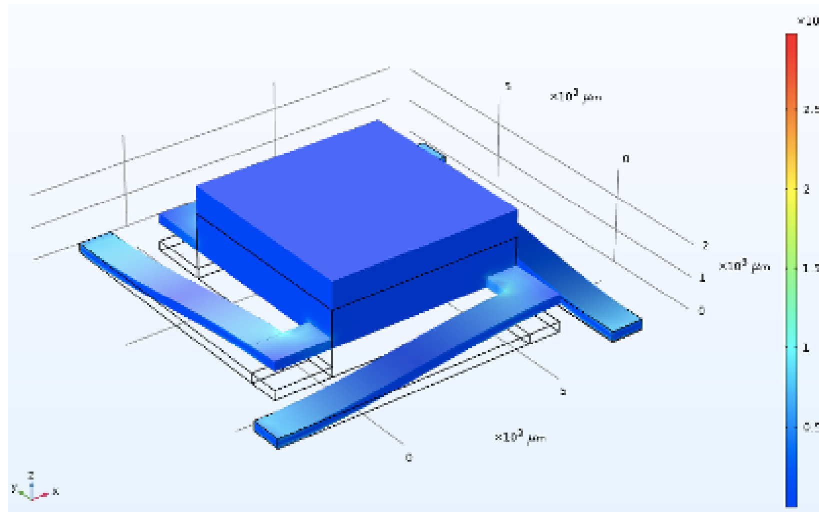

Figure 3.17: Floating potential of 3.63 mV obtained for the first1st mode shape under a base excitation of 1g along Z direction

Fig.3.18 represents simulation results for sensing functionality of the tri-axial accelerometer along X direction. When the whole sensing device is stimulated along X direction, since center of mass of the proof mass is not placed in alignment with respect to constrained elements (beams), proof mass is rotated around Y-axis. By this way, the voltage values obtained from beam B and beam C show the same sign but different from the beam A and beam D.

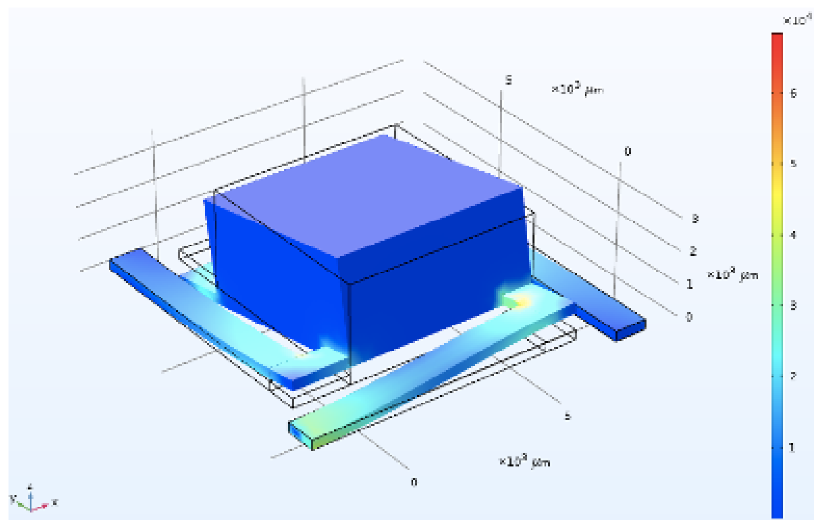

Figure 3.18: Floating potential of 1 mV obtained for the first1st mode shape under a base excitation of 1g along Z direction

Similarly, When the whole sensing device is stimulated along Y direction, since the center of mass of the proof mass is not placed in alignment with respect to constrained elements (beams), proof mass is rotated around X-axis. By this way, the voltage values obtained from beam A and beam B show the same sign but different from the beam C and beam D. As a result, whenever voltage values obtained from the beam B and beam C have the same sign, the whole device is stimulated/ accelerated along X direction otherwise, when the beam B and beam C have different signs, whole device is stimulated/ accelerated along Y direction.

Chapter 4

METHODOLOGY AND EQUIPMENT OF EXPERIMENTS

4.1 Materials

What distinguishes this study from other studies is that a polymer-based piezoelectric accelerometer was fully 3D-printed for the first time. To fulfill this aim, Stereolithography 3D-printing process was used to print a prototype with a new high working temperature resin called THERMA DM500 as substrate. The major material that not only has a crucial role on functionality of the designed accelerometers but also has an impact on selection of the material used as substrate is piezoelectric copolymer. The piezoelectric copolymer selected for this study is P(VDF-TrFE) with 30 weight percent of TrFE and 70 weight percent of VDF due to the fact that this copolymer directly crystalizes into a phase called beta-phase which can show piezoelectric character. The selected copolymer is actually a semi-crystalline polymer needed to apply some post treatments like annealing and poling to increase the degree of crystallinity and aligning the randomly oriented dipoles after the printing and consequently to obtain the effective piezoelectric coefficients. Annealing temperature has a strong effect on the piezoelectric character. Generally, thermal treatment in temperature range between 100-140 °C is suggested. To do such a considerably high thermal treatment (for polymers), the host of the piezopolymer should have high working temperature. The conventional resins which are adaptable to Stereolithography 3D-printer do not have such a high working temp. That is the reason why a new resin called THERMA DM500 which can tolerate up to 220 °C with up to 90 bar of closing pressure was purchased from Sigma-Aldrich. Bottom and top electrodes are inkjet-printed using a silver nanoparticles dispersion in triethylene glycol monomethyl ether with specifications 30-35 weight percent (wt) solid content and 7 micro ohm-cm resistivity.

4.2 Equipments

The process steps for fully 3D-printed piezoelectric polymer-based accelerometers are shown in Fig.4.1. step-by-step. Additive manufacturing processes and measuring equipment are explained for each step in the following subchapters.

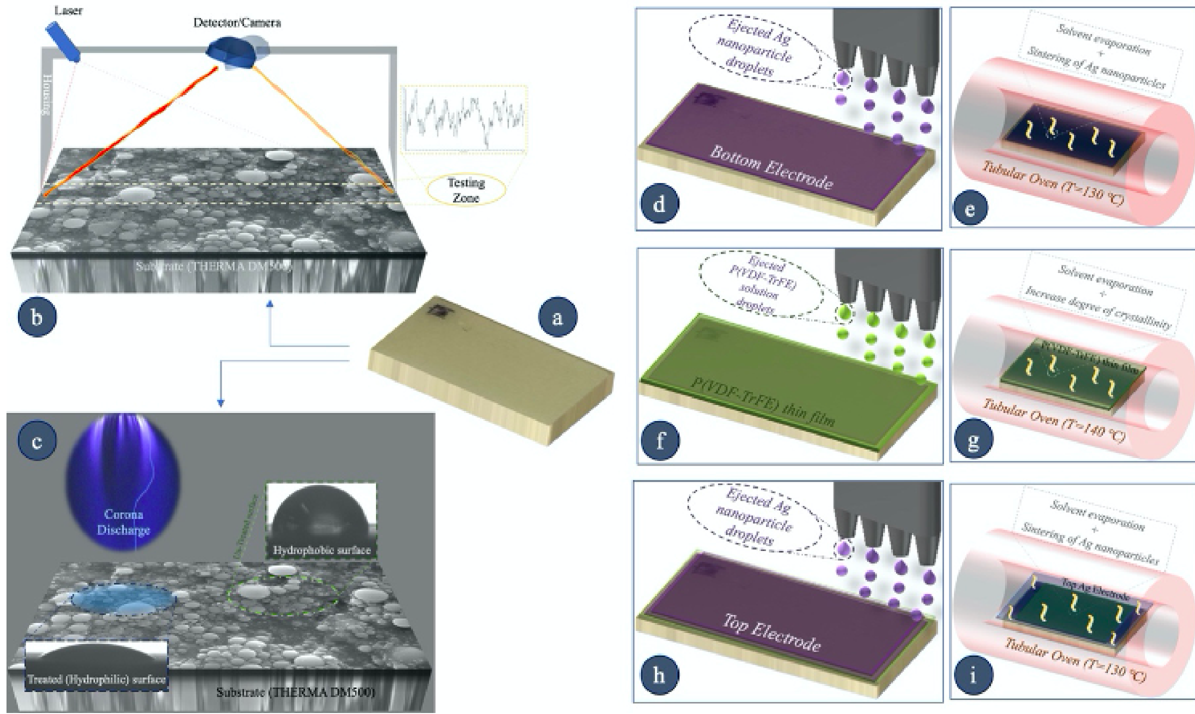

Figure 4.1: Schematically process chains for fully 3D-printed piezoelectric polymer-based accelerometers. a) Substrate fabricated by SL, b) profile analysis via laser profilometer, c) Corona surface treatment and wettability behavior, d) printing bottom electrode, e) annealing of the bottom electrode, f) printing P(VDF-TrFE) film, g) annealing of the P(VDF-TrFE) film, h) printing top electrode, i) annealing of the top electrode.

4.2.1 Stereolithography 3D-Printer

All the samples and parts in the present work were printed with a commercial stereolithography machine available at Politecnico di Milano, model 028J Plus produced by Digital Wax Systems (DWS). This machine mounts a monochromatic actinic laser solid state Bluedge BE-1500A/BE- 1500AHR with galvanometer control, an emitting power of 30 mW, a wavelength of 405 nm and a beam spot diameter of 25 um and a vertical (z-axis) resolution of 10 um. The 3D models were designed with COMSOL Multiphysics software, the output was processed by Nauta+ software, the parametric editor provided by DWS with the printer. Then the output was sent to Fictor software by DWS, that directly controls the printer and execute the slicing operation, accordingly to the input operational parameter setup.

Laser speed was ranged between 258 and 4300 mm/s, the layer thickness around 30 um and a 20 um hatching was used. After the printing step, the samples were washed in ethanol to remove unreacted resin and dried in nitrogen flux. The polymer reticulation was then concluded by further exposure to light for 30 minutes in a dedicated UV-curing unit (wavelength = 405 nm) coupled with the printer. Printing parameters were determined autonomously by +LAB and their full characterization is out of the aim of the present work. For this reason, even though a brief discussion is provided in the results part, they were considered optimal. Mechanical characterization tests show that photocured polymer has not perfectly isotropic mechanical properties but mechanical properties along the layer and its perpendicular direction is almost same with no significant difference.

Figure 4.2: Digital Wax Systems (DWS) 028J+

4.2.2 Fujifilm Dimatix Inkjet Printer

As shown in Fig.4.1 (d, f, h), for inkjet printing the bottom electrode, piezoelectric polymer thin film and top electrode subsequently onto the substrate, Dimatix DMP-2850-Fujifilm Inc., USA, equipped with a droplet volume of 10 pL cartridge is used (Fig.4.3). The Dimatix inkjet printer is suited to print fluids including nanoparticles, conductive polymers as ink materials. The printable materials are injected into disposable cartridges using specific needle and filter. Each cartridge has 16 individually addressable piezo-actuated nozzles through which the fluid is dispensed. The jetting voltage of each nozzle can be individually tuned to optimize the printing of the ink. A typical voltage cycle consists of

three segments: 1) a negative voltage period to fill the cartridge, 2) a positive voltage period to dispense the ink and 3) a segment that allows the nozzles to recover to its original shape. The entire cycle is referred to waveform. A waveform is optimized when it drives the nozzles such that they dispense perfectly ejected droplets at a high speed. The printer uses an array of 16 piezoelectric nozzles with 21.5 um openings to eject the droplets. The fluid used as ink is better to have the following properties: i. Any particle in the fluid should be less than 0.2 um filter in size (100 times smaller than the nozzle opening). To remove large particles aggregate, filter needs to be used just before injection of ink into cartridge. ii. To protect the printing nozzles from drying out, it is strongly suggested to use inks evaporating with slow rate. If an ink evaporates too fast, glycol needs to be added to the ink. Glycol lowers the evaporation rate of aqueous fluids. Furthermore, for safety reasons, solvents with a flash/ignition point below 120 °C are prohibited in the printer. iii. The viscosity of the ink should be between 10-12 cps (10-2 Pa.s). If the viscosity is too high, it is possible to lower it by heating the printhead up to 60 °C. iv. The surface tension of the ink should be between 28-33 dynes/cm2 (2.8-3.3 N/m2). To increase the surface tension, it is suggested to add a surfactant into inks. v. To prevent the formation of bubbles at the nozzles head during printing, it is necessary to degas the aqueous ink.

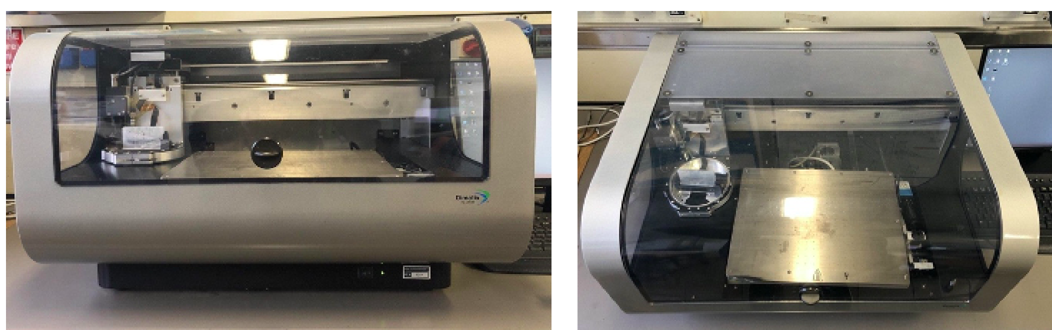

Figure 4.3: FUJIFILM DIMATIX DMP-2850 INKJET PRINTER

4.2.3 Laser Profilometer

Although AM has many advantages over the traditional processes, it has some major drawbacks such as poor surface quality. In our case, since surface roughness of substrate 3D-printed by Stereolithography process has a key impact on inkjet printing of upper layers and eventually sensing functionality, a laser profilometer was used. The instrument used to perform profile analysis for this study is a UBM Microfocus. This device is also used to measure thickness of the printed P(VDF-TrFE) layer.

4.2.4 Contact Angle Measurements

In order to evaluate the wettability characterization of the substrate made of THERMA DM500 resin, the distilled water contact angle (CA) tests were carried out by a Microcamera Stingray produced by Allied vision for both untreated and treated surfaces. In order to study the shape of the distilled water

droplets on substrate surface and contact angle measurements, the Drop Shape Analysis software are used.

Figure 4.4: CONTACT ANGLE MEASUREMENTS

4.2.5 Corona Surface Treatment Device

Polymer films have chemically inert and non-porous surfaces with low surface tensions causing them to be non-receptive to bonding with printing inks. In order to enhance the surface energy of the substrate surface made of THERMA DM500 resin and also improve its wettability behavior, the corona treatment method is used. Fig.4.1 (c) shows schematically the working principle of the Corona surface treatment.

4.2.6 Furnace

During fabrication steps, there are some reasons to do Heat Treatment. First of all, as shown in Fig.4.1 (e, i), in order to obtain high conductive electrodes, sintering of silver nanoparticles which are going to be deposited/inkjet-printed as electrodes should be performed at high temperature. Hence, after inkjet printing of the bottom electrode Fig.4.1 e and top electrode Fig.4.1 i, furnace oven is used. Secondly, copolymer (P(VDF-TrFE)) possesses a semi-crystalline structure. In order to obtain a high beta-phase content which among the other phases of this polymer shows piezoelectric character, Thermal Treatment should be done after inkjet printing of P(VDF-TrFE) ink Fig.4.1 g.

4.2.7 Stereo-microscope and Scanning Electron Microscope (SEM)

Owing to the fact that the new resin (THERMA DM500 resin), employed in this study to fabricate the prototype, is somehow unknown, it was necessary to do chemical and surface morphology analysis before and after inkjet printing of silver nanoparticle solution onto the substrate surface. Materialographic characterizations are performed using SEM to study behavior of silver nanoparticles solution inkjet-printed onto substrate surface as well as behavior of P(VDF-TrFE) inks printed over the bottom electrode. Also, Energy Dispersive Spectroscopy (EDS) is used to assess the compositions. The SEM used for this study is an EVO 50 EP by Zeiss coupled with an Inca Energy EDS unit by Oxford Instruments. In order to observe images of inkjet-printed patterns with low magnification, a Leica DM LM microscope was used. A Wild M8 stereomicroscope by Heerbrugg was employed as well. The measures were performed with Leica software by the camera system.

4.3 Methodology (of experiments)

Due to the fact that the THERMA DM500 resin, employed in this study to fabricate substrate, is somehow unknown, some cubic samples were printed with Stereolithography 3D-printer whereby some characterizations like water contact angle tests, laser profilometry of surface and the most importantly the behavior of silver nanoparticle ink on the samples can be done. It was decided to print the cubic samples by Stereolithography 3D-printer vertically and horizontally, in order to understand effect of different conditions such as printing orientation in SL process on samples geometry and surface quality.

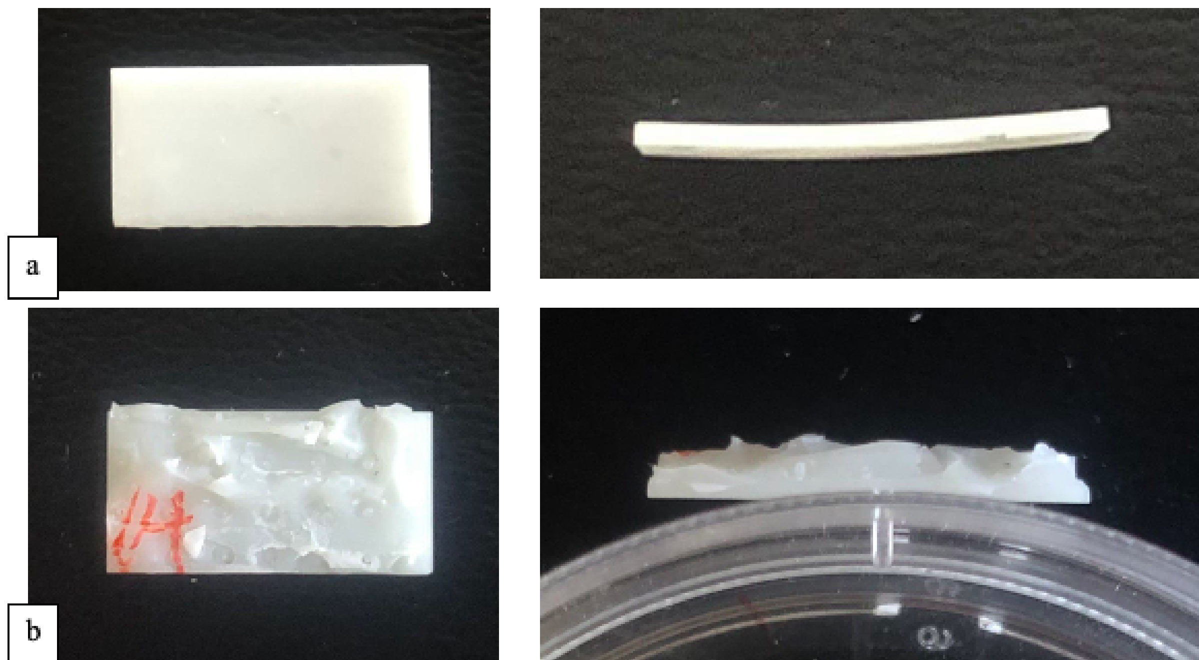

Figure 4.5: a) Vertically SL 3D-printing, b) Horizontally SL 3D-printing of substrate.

Stereolithography 3D-printing process parameters were determined autonomously by +LAB and their full characterization is out of the aim of the present work. Optimal Stereolithography 3D-printing process parameters applied for this study is just reported in section 4.2.1. To achieve a preliminary information/knowledge about wettability behavior/property of substrate surface, it is needed to do distilled water contact angle tests for both untreated and treated samples surface. Surface treatment is carried out using the Corona discharge device. Eventually, in order to determine the best inkjet-printing condition and parameters for printing of silver electrodes, two different patterns (droplet arrays and continuous patterns) with various printing parameters (drop speed V, drop spacing d and jetting frequency) on the untreated (hydrophobic) and treated (super hydrophilic) samples, were printed. For printing of all the patterns, just one nozzle was used with a conventional shape of waveform Fig.4.6 whose parameters were modified to get the best possible droplet shape. As shown in Fig.4.6, the droplets that we obtained were considerably rounded with a short tail that is disappeared quickly for velocities less than 6 m/s but the tail starts extending when the droplet speed increases.

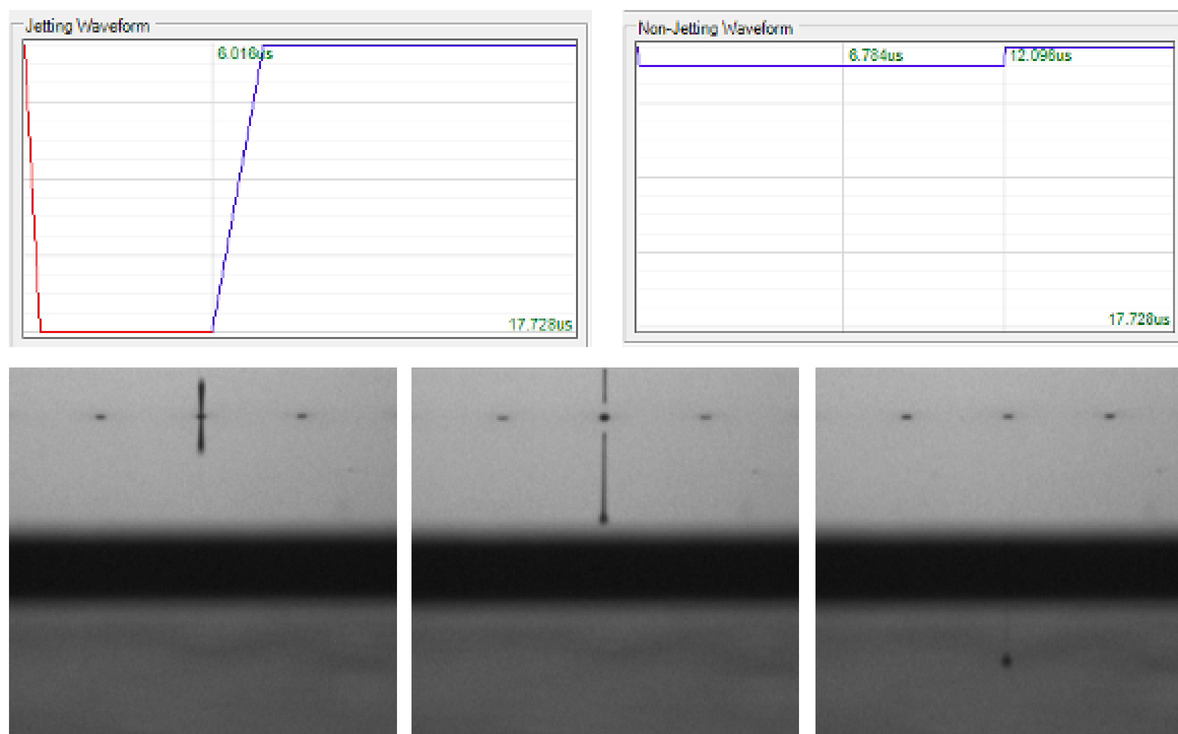

Figure 4.6: Camera views of silver nanoparticle ink droplets.

In the case of jetting frequency, generally speaking the increase of printing frequency leads to a fast printing but loss of precision and quality of printed film. in order to verify this fact, two different jetting frequencies 1KHz and 10KHz corresponding to low and high jetting frequencies, respectively, were set and studied keeping constant other printing parameters. In the drop speed case, we expect that the droplet speed affects the size of the single droplets on the surface and consequently the distribution of materials (film uniformity). In order to verify this fact, two arrays of droplets with the same drop spacing (d=140 um) but different drop speeds (V1=5m/s and V2=8m/s) were printed on untreated and treated samples. Then, in order to compare the behavior of printed silver electrodes on the untreated and treated samples, 3 different rectangular shape patterns (2mm*10mm) with different number of layers and drop spacing (d1=20 um and d2=40 um) on each sample were printed keeping constant the other printing parameters. Then, the films were annealed in 130 °C temperature with 30 °C /min heating rate for one hour to completely remove the solvent and sinter silver nanoparticles. In order to investigate behavior of P(VDF-TrFE) solution with final purpose which is measuring and evaluating thickness of P(VDF-TrFE) printed films, several different layers were inkjet-printed on a super flat surface of Silicon substrate. To this aim, patterns with different process parameters and conditions inkjet-printed onto the super flat surface discussed in Results and Discussion chapter. After all above characterizations tests, optimum inkjet printing process parameters and conditions for

printing silver electrodes and P(VDF-TrFE) film could be achieved. In the next step, based on the optimum inkjet printing process parameters and conditions obtained from the characterizations tests, a 3-layers bottom silver electrode is inkjet-printed onto the cantilever. Then, the films were annealed in 130 °C temperature with 30 °C/min heating rate for one hour to completely remove the solvent and sinter silver nanoparticles. Then, a 37-layers P(VDF-TrFE) film is inkjet-printed over the bottom electrode. Then, the film was annealed in 140 °C temperature with 30 °C/min heating rate for one hour and half to completely remove the solvent. Finally, a 3-layers top silver electrode is inkjet-printed over the P(VDF-TrFE) film and then again the films were annealed in 130 °C temperature with 30 °C/min heating rate for one hour to completely remove the solvent. In order to characterize the performance of the active layer printed onto the cantilever, it is necessary to measure the electric potential achieved from manual deflection/strain applied manually at the free end of the cantilever beam. Measurements for electric potential are taken with a setup consisting of a resistor and an ampere meter trying to measure the current from a circuit. The passing current was observed but the cantilever broke during the test and nothing was recorded. After being sure that the whole fabrication process goes on well, we got ready to take further steps towards fabrication of the real device. In this research, Z-axis accelerometer is fabricated based on a 4-layer structure in which all layers are applied on top of each other sequentially. The layers from bottom to top are the substrate, the inkjet-printed bottom silver electrode, the inkjet-printed P(VDF-TrFE) film, and the inkjet-printed top silver electrode. The electrodes are routed to two contact pads at the base where a voltage supply can be connected. The P(VDF-TrFE) film is only applied to the beam region and not to the base, to allow a conductive contact point with the bottom electrode. In the following, 3-layer structure in which all layers are applied on top of each other sequentially and required steps for electromechanical characterization test are explained.

1) Bottom silver electrode: To fabricate the sensor, the first step is to print the bottom electrode. The pattern desired to be printed is generated and positioned 1000 um away from the edges of the beam as origin point. To achieve proper coverage, it was observed that after 3 inkjet-printed layers, the inkjet-printed region gets fully covered and shows no sign of the substrate surface and even voids or defects. Once each layer is inkjet-printed, it is required to wait for at least 30 min to give enough time to the solvent to be evaporated. Once all the layers are inkjet-printed, the bottom electrode is dried at 130 C for one hour to ensure complete solvent evaporation.
2) P(VDF-TrFE) film: The next step is to inkjet-print the P(VDF-TrFE) solution with formulation of 0.7wt P(VDF-TrFE) dissolved in the mixture of DMSO (70wt) / MEK (30wt) solvents. The pattern desired to be printed is generated and positioned exactly from the beam corner as origin point. Regarding the characterization tests, it is found out that printing 37 layers satisfies the desired thickness considered as Finite Element Analysis (FEA) and also to ensure full insulation between the top and bottom electrodes. Once each layer is inkjet-printed, it is required to wait for at least 10 min to give enough time to the solvent to be evaporated. Once the desired number of layers have been applied, the device is annealed for one hour and half at 140 °C.
3) Top silver electrode: The third step is to inkjet-print the top silver electrode. The top electrode

is inkjet-printed directly onto the dry polymer. The pattern desired to be printed is generated and positioned 1000 um away from the edges of the bottom electrode as origin point. Once the 3-layers top silver electrode have been applied, the device is annealed for one hour at 130 °C. 4) Poling: The final step of preparation is the poling of the active layer. The Z-axis accelerometer beams are connected at their contact pads to a power supply, to do poling in a step-wise procedure in which the voltage is enhanced in each step to reach a maximum of 100V, and placed on a hot plate at 80 °C. Then the power supply is turned on and the samples are allowed to be poled for 10 minutes in each step and total of 50 minutes. Afterwards the hotplate is turned off and the samples are allowed to cool whilst the power supply remains on. When the samples reach ambient temperature, the power supply can be disconnected, and poling is complete.

Chapter 5

RESULTS AND DISCUSSION

Due to the fact that the new resin, used to fabricate the substrate, was somehow unknown, we decided to print some cubic samples with SL so that some characterizations like contact angle tests, laser profilometry of surface and the most importantly the behavior of silver nanoparticle ink on the samples can be done. It was decided to print the cubic samples by SL vertically and horizontally in order to understand the effect of the printing methods on samples geometry and surface roughness. The first observation was that the sample printed horizontally was deformed with the presence of imperfections over one side in such a way that there was not the possibility of printing silver electrodes inkjet printer. The surface profilometry of the horizontally and vertically printed samples, represented in Fig.5.1.a and Fig.5.1.b, illustrates that in consistence with our expectation the vertically printed samples are rougher as compared to horizontally one; however, fortunately the difference is not such a high that significantly affects the bottom silver electrode morphology and consequently other layers.

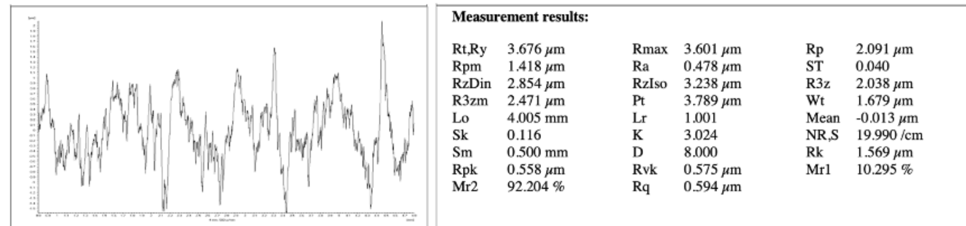

Surface roughness parameters of vertically printed sample.

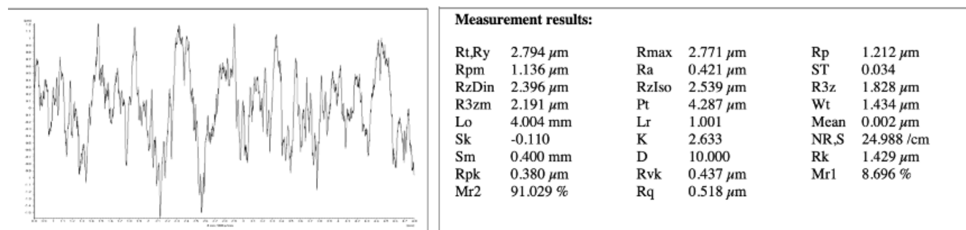

Figure 5.1: Surface roughness parameters of horizontally printed sample.

The SEM analysis of the sample, shown in Fig.5.2, illustrates that high content of reinforcing particles, mostly Silica, with various sizes reaching to 2 um is used which could be explained as a way to induce more thermal stability to the polymer. Hence, apart from the roughness due to the essence of SL printing, presence of large particles could be regarded as another reason why we have a rough surface.

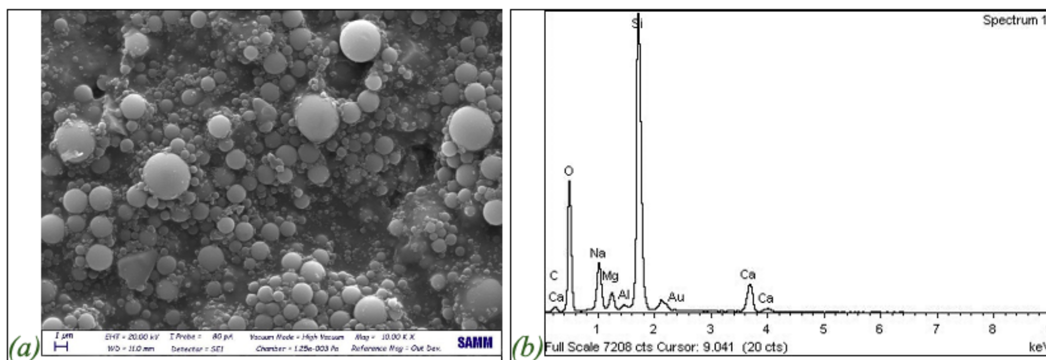

Figure 5.2: Representing (a) Content and size of the reinforcing particles and (b) Elemental composition employed in THERMA DM500 resin.

The water contact angle (CA) tests represent that the surface of the sample is not hydrophilic with mean contact angle of 82.3°(Fig.5.3 a); however, by corona treatment a super hydrophilic surface could be obtained eventually with water contact angle of less than 10°(Fig.5.3.(b-d)).

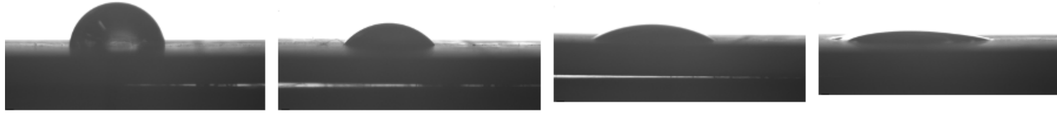

Figure 5.3: (a) untreated sample CA= 81.9° (b) treated sample CA= 49.9° (c) treated sample CA= 27.6° (d) treated sample CA= 13.4°

In order to determine the best printing condition and parameters for printing of silver electrodes, two different patterns (droplet arrays and continuous patterns) with various printing parameters (drop speed V, drop spacing d and jetting frequency v) on the untreated (hydrophobic) and treated (super hydrophilic) samples, were printed. For printing of all the patterns, just one nozzle was used with a conventional shape of waveform whose parameters were modified to get the best possible droplet shape. The droplets that we obtained considerably rounded with a short tail that is disappeared quickly for velocities less than 6m/s. But a tail starts extending when the droplet speed increases (Fig.4.6). Generally, the increase of printing frequency leads to having a fast printing but lose of precision and quality of the printed film. In order to verify this fact, two arrays of droplets of silver ink were printed on untreated sample with two different jetting frequency 1KHz and 10KHz shown in Fig.5.4. (a-b), respectively, and keeping constant of other printing parameters. The images obtained by Stereomicroscope of the two arrays/patterns show that at least for silver nanoparticle ink, the increase of frequency (from 1KHz to 10KHz) does not lead to significant loss of precision. In other words, the shape of droplets on the resin surface and their distances are almost the same for both cases. Besides, the SEM images of continuous films boarders printed with 10KHz frequency (Fig.5.5) shows that a fast printing is possible for silver ink without loss of boarder accuracy.

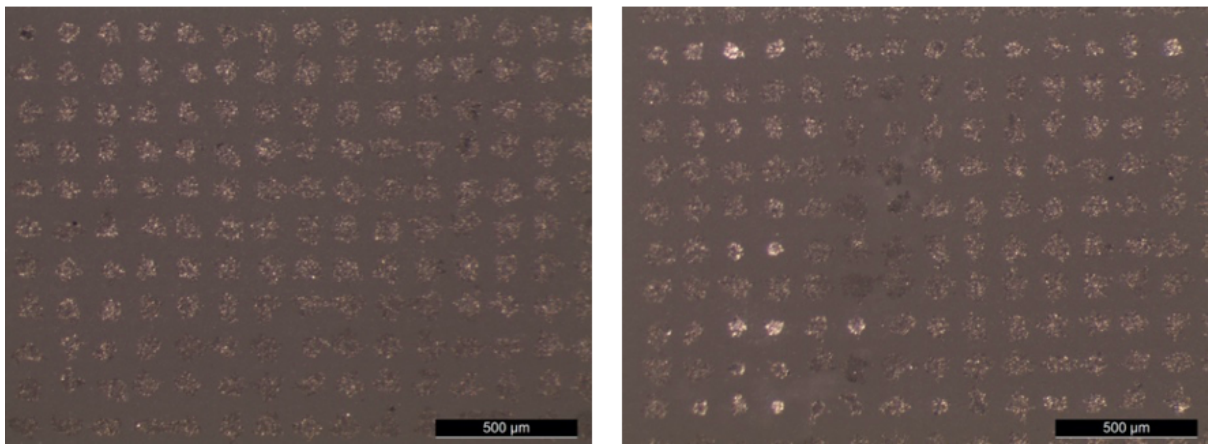

Figure 5.4: Images obtained by Stereomicroscope for droplet arrays of silver ink on un-Treated substrate surface.

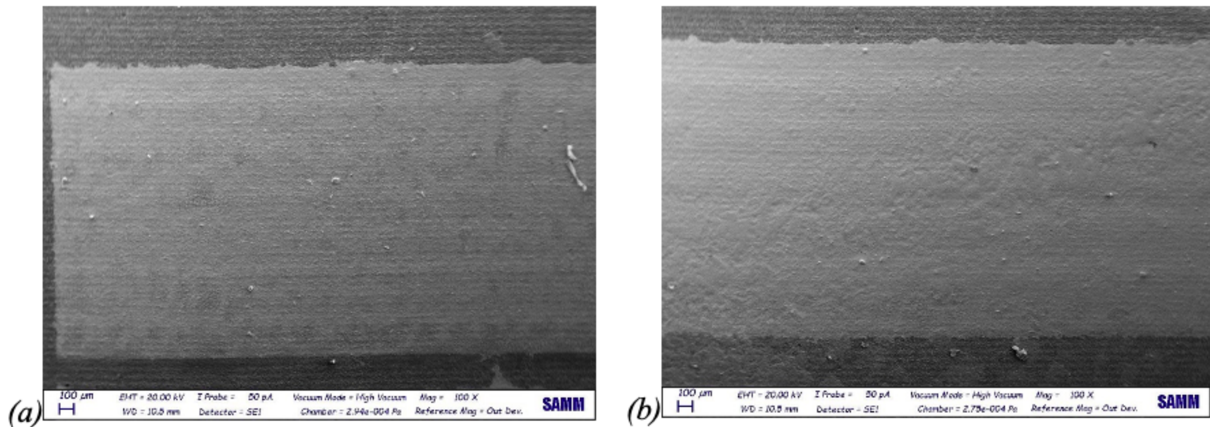

Figure 5.5: SEM images of continuous films boarders of (a) 1 layer and (b) 2 layers printed with 10KHz frequency and d=20 um on un-Treated substrate surface

We expect that the droplet speed affects the size of the single droplets on the surface and consequently the distribution of materials (film uniformity). In order to verify this fact, two arrays of droplets with the same drop spacing (d=140um) but different drop speeds (V1=5m/s and V2=8m/s) were printed on untreated and treated samples. As expected, the droplets with higher speed are larger in size on the surface and coalescence of the droplets in some areas can be observed in Fig.5.6.

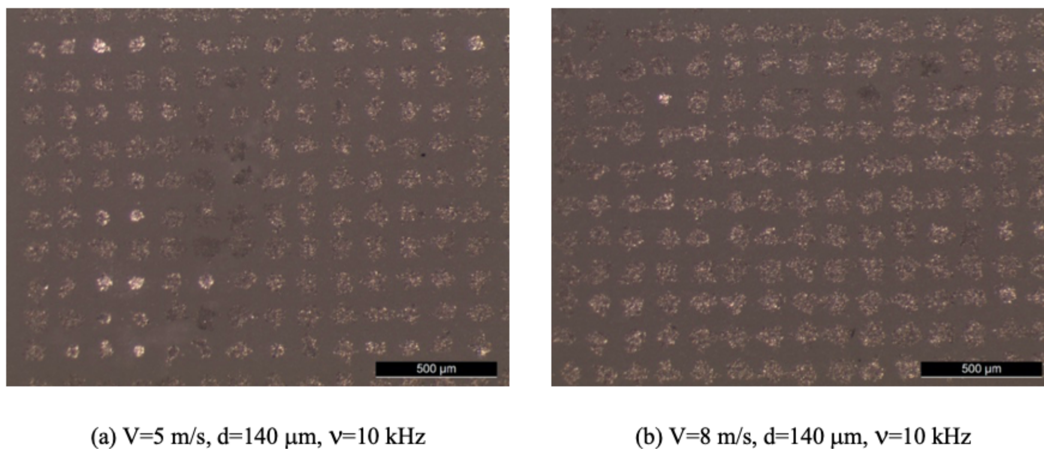

(a) V=5 m/s, d=140 µm, ν=10 kHz   (b) V=8 m/s, d=140 µm, ν=10 kHz

Figure 5.6: Images obtained by Stereomicroscope for droplet arrays of silver ink on un-Treated substrate surface.

The same phenomena is observed for the droplets printed on the hydrophilic treated sample with the difference that in the case of treated surface, the single droplets are larger in size with respect to that of untreated sample and when the drop speed increases from 5m/s to 8m/s, they coalesce completely to each other (Fig.5.7).

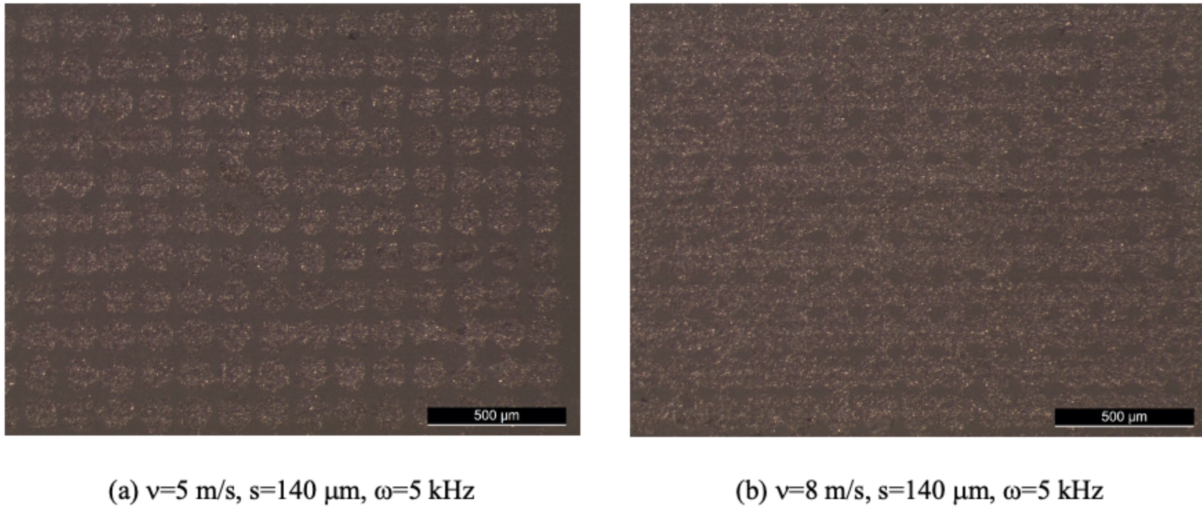

Figure 5.7: Images obtained by Stereomicroscope for droplets array of silver ink on Treated substrate surface.

In order to compare the behavior of printed silver electrodes on the untreated and treated samples, 3 different rectangular shape patterns (2mm*100mm) with different number of layers and drop spacing (d1=20um and d2=40 um) on each sample were printed keeping constant of other printing parameters. Then, the films were annealed in 130 °C temperature with 30 °C/min heating rate for one hour to completely remove the solvent and sinter silver nanoparticles. The first observation is that in the case of treated sample where we have a super hydrophilic surface, we considerably lose the precision of the pattern boarders which can be explained taking into account the fact that by Corona treatment done to reduce the contact angle, a surface with uniform wettability cannot be obtained.

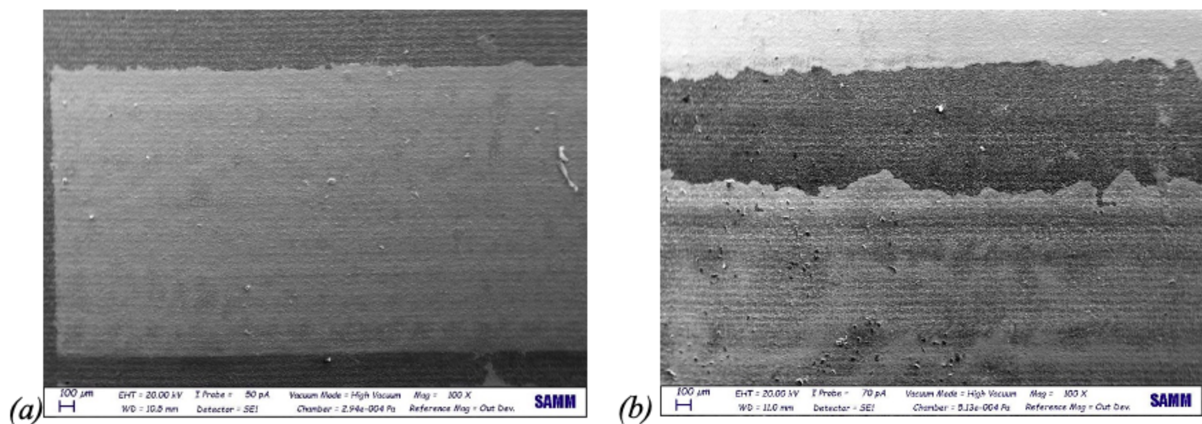

Figure 5.8: The SEM images of continuous films boarders of 1-layer printed on (a) un-Treated and (b) Treated substrate.

Fortunately, from Fig.5.8, it can also be deduced that the surface wettability of the untreated sample is not too low to form isolated islands instead of a continuous film. Second observation, shown in Fig.5.9, is that for neither treated nor untreated samples, with printing of just one layer for both 20 and 40 drop spacings, complete coverage of the surface is possible. Meaning there remain always large uncovered particles. However, with two layers printing in both cases, complete surface coverage can be achieved (Fig.5.10.a, b), and the surface gets somehow levelized (Fig.5.10.c).

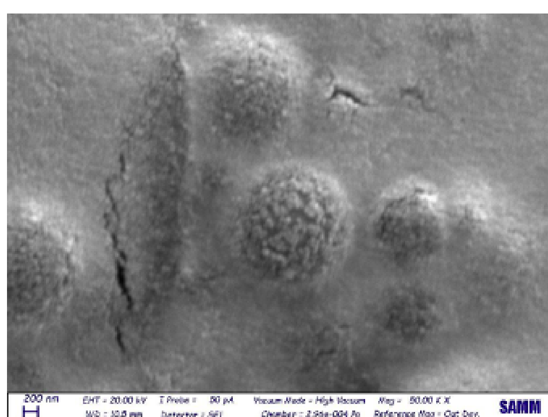

(a) un-treated, d= 20µm

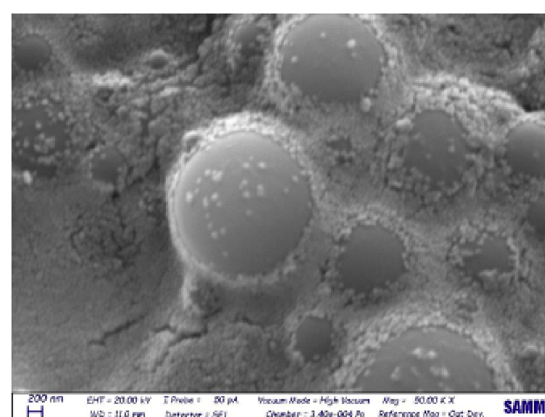

(b) treated, d= 20µm

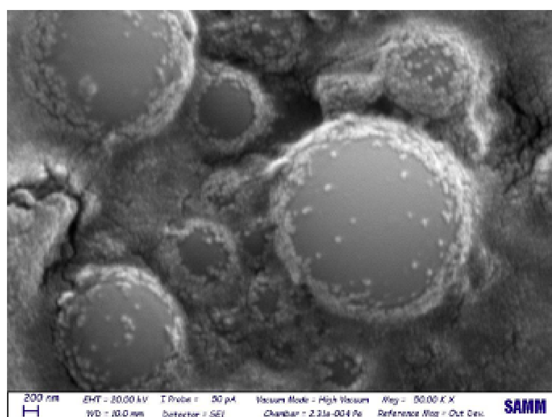

(c) un-treated, d= 40µm

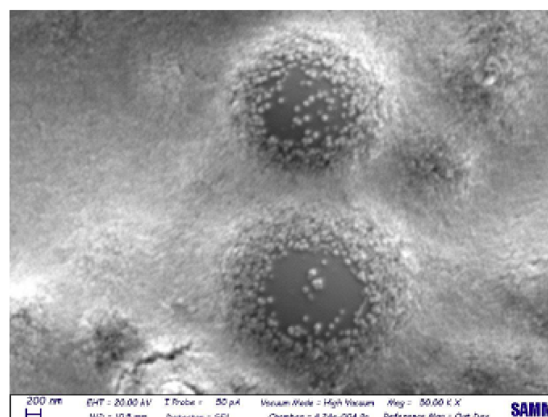

(d) treated, d= 40µm

Figure 5.9: Surface coverage for 1-layer of silver nanoparticle printed with 20 um and 40 um drop spacing for both un-treated and treated samples.

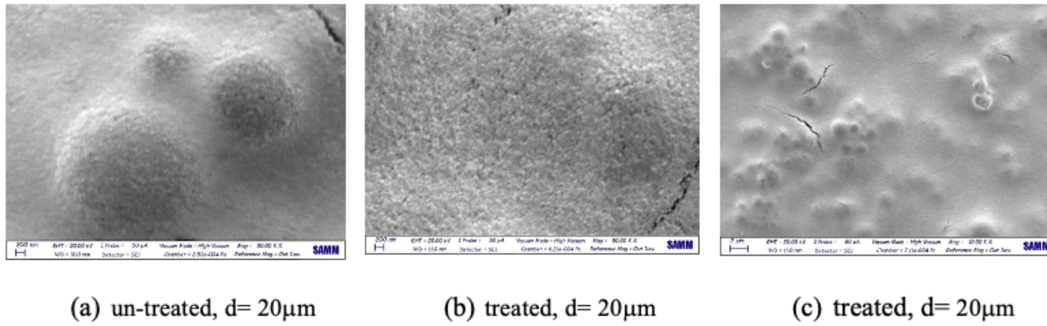

(a) un-treated, d= 20μm (b) treated, d= 20μm (c) treated, d= 20μm

Figure 5.10: Surface coverage for 2-layers of silver nanoparticle printed with 20 um drop spacing for both un-treated and treated samples.

One of the most important features of the printed films is the presence of micro-cracks which can be due to thermal stresses resulted from annealing process and presence of large particles on the surface favoring the accumulation of energy locally leading to cracking (Fig.5.11).

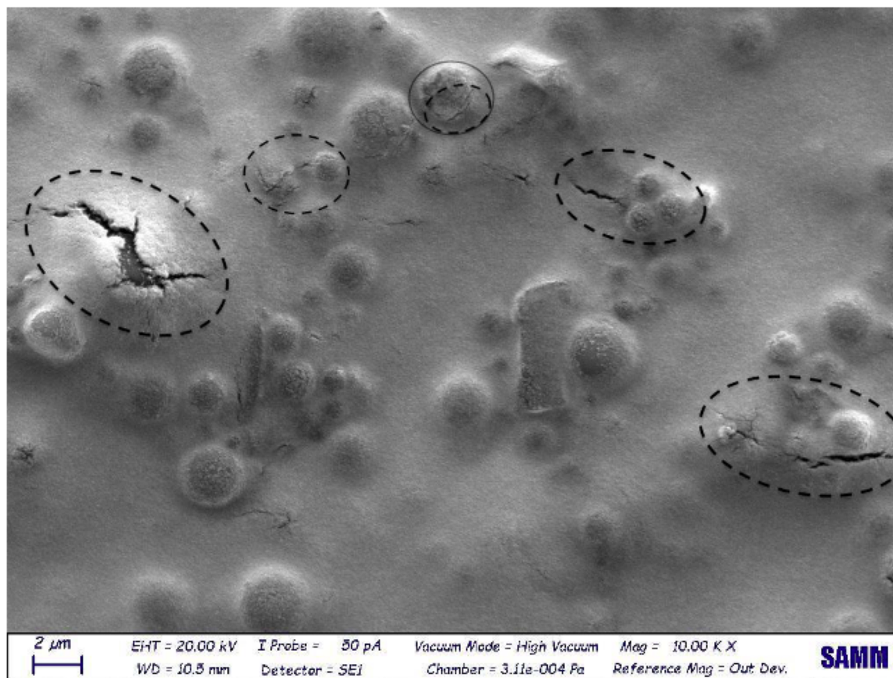

Figure 5.11: Effect of presence of large particles on the creation of micro-cracks.

As seen in Fig.5.12, comparing the SEM images of films on un-treated sample with that of treated one convinces us to claim that the films on the surface with high wettability are less prone to develop cracks and, in addition, the formed cracks are less harsh due to the fact that the silver nanoparticle

ink distributes better on the wettable surface preventing local accumulation of material.

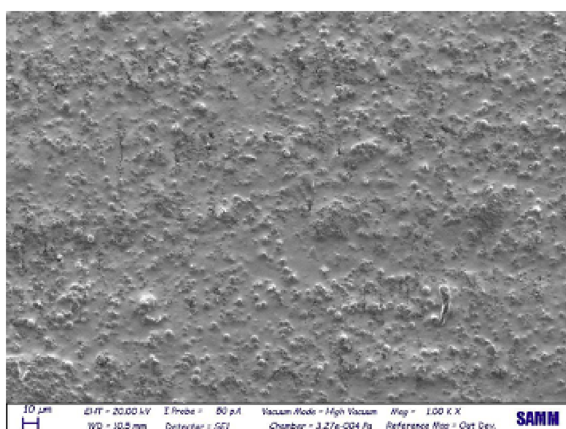

(a) un-treated, one layer (1x)

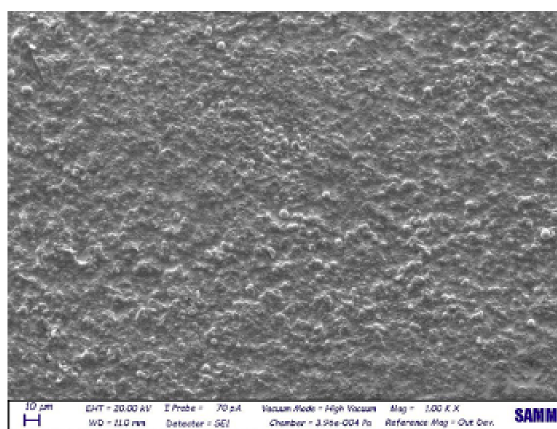

(b) treated, one layer (1x)

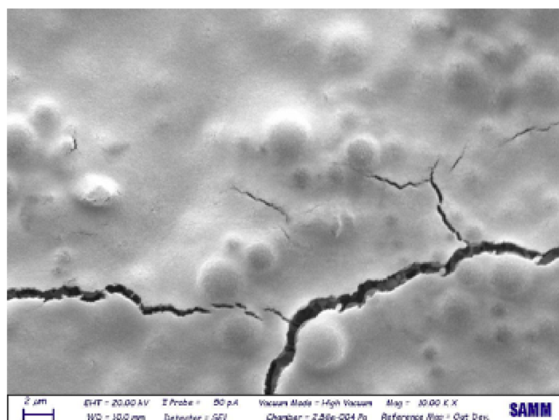

(c) un-treated, two layers (2x)

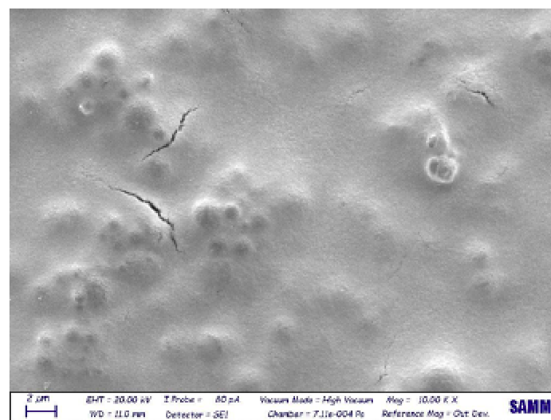

(d) treated, two layers (2x)

Figure 5.12: SEM images comparing severity of micro-cracks on 1-layer and 2-layers printed films with 20 um drops spacing for both un-treated and treated samples.

Based on the experimental results, process parameters need to be set for inkjet-printing of silver nanoparticle ink onto substrat. SEM images show that with drop spacing 20 um, the whole substrate sutrface is not covered, and at least two layers are required. Therefore, three layers are defined/set with drop spacing 20 um (Fig.5.13).

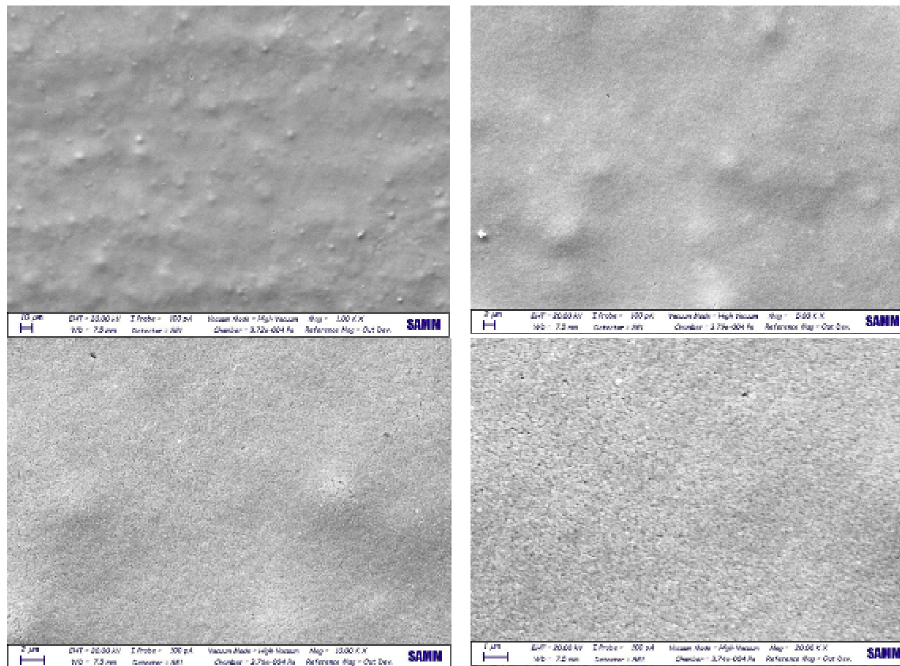

Figure 5.13: Surface coverage for 3-layers of silver nanoparticle printed with 20 um drop spacing.

Furtheremore, from SEM chemical analysis shown in Fig.5.14, it is proved that almost pure silver is inkjet-printed.

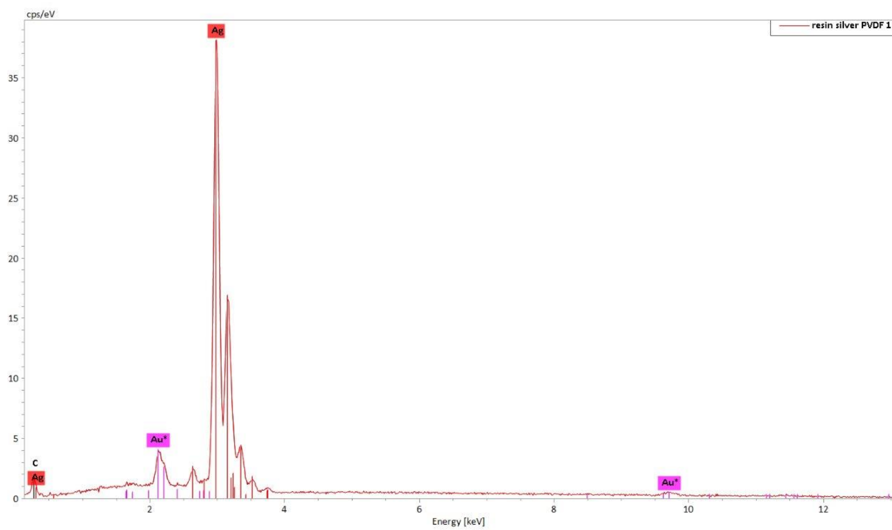

Figure 5.14: Elemental composition employed in silver nanoparticle inkjet-printed.

Besides, jetting frequency and drop speed are set to be equal 5KHz and 6m/s, respectively. Although the substrate surface with high wettability are less prone to develop cracks, we lose significantly the precision of boundaries which can lead to short circuit by connection of bottom and top electrodes. That is the reason why an intermediate contact angle can be set to be approximately 50 degree. After studying the behavior of the inkjet-printed silver nanoparticles ink onto the substrate surface, the next step of fabrication process is assigned to one of the most challenging steps which is inkjet-printing of P(VDF-TrFE) solution. Due to complex rheological behavior of the inks containing polymer and complications in inkjet printing using Dimatix DMP-2850 inkjet printer, it is needed to prepare and study several different types of solvents and mixture of solvents with different P(VDF-TrFE) concentrations. Hence, in order to find the best possible P(VDF-TrFE) solution which are compatible with the Dimatix DMP-2850 Inkjet printer without nozzles clogging during printing, different types of solvents and mixture of solvents with different P(VDF-TrFE) concentrations, described in Fig.5.15, were studied.

Physical Properties	unit	Cyclopentanon	Dimethyl Sulfoxyde (DMSO)	2-Butanon (MEK)
Viscosity	MPa.s	1.29	1.9	0.43
Surface Tension	mN/m	33.31	43.5	24.6
Boiling Point	∘C	130.6	190.8	79.6
Density	g.cm^3	0.95	1.1	0.8

°n	Cyclopentanon	DMSO	MEK	P(VDF-TrFE)	Droplet ejection condition
	wt%	wt%	wt%	wt%	
1	100	0	0	2	Not stable
2	100	0	0	1.5	Not stable
3	0	80	20	0.8	Not stable
4	0	70	30	0.7	YES

Figure 5.15: a) Physical Properties of the 3 different solvents, b) Mixture of solvents with different P(VDF-TrFE) concentrations [55].

At the first try, only Cyclopentanon (100 wt of Cyclopentanon) was formulated/dissolved with/in 2wt P(VDF-TrFE). Then, an agitator was used at 500 rpm for 30 min. Finally, the prepared P(VDF-TrFE) solution was tried to be inkjet-printed but it was unsuccessful. At the second try, we reduced the P(VDF-TrFE) concentration to 1.5wt keeping the same Cyclopentanon concentration; however, again no drop ejection was observed from the nozzles. It can be justified that high evaporation rate and low density, characteristics of Cyclopentanon, can result in nozzles clogging. In fact, high evaporation rate of Cyclopentanon provides/fascilitates a destructive situation for rapid formation of solid polymer membrane at the nozzles head. As a result, Cyclopentanon does not match with the specifications of the Dimatix inkjet printer.
Hence, we decided to change the approach using two stronger solvents instead of only Cyclopentanon. In the third examination/ try, we used 80 wt of Dymethil sulfoxyde and 20 wt of butanon (MEK) with 0.8 wt of PVDF-TrFE. In this case, the inkjet printing situation improved so that drop ejections can be observed but after a few drop ejections, the nozzles were clogged.
Eventually at the last try, DMSO concentration is reduced to be approximately 70wt. Therefore, the optimized P(VDF-TrFE) solution formulation was achieved for 0.7wt P(VDF-TrFE) dissolved in the mixture of DMSO (70wt) / MEK (30wt) solvent so that reproducible continuous/stable droplets are ejected from the printhead nozzles during printing. The reason why the DMSO is not allowed to be reduced so much is that DMSO is a polar solvent which can be regarded a good solvent for P(VDF-TrFE).
After obtaining the optimal P(VDF-TrFE) solution formulation, inkjet printing process conditions and parameters need to be optimized to achieve high-quality printing of P(VDF-TrFE) solution onto the bottom electrode. As predicted, the most important challenges are formation of droplets with long filaments and deviation of droplet trajectory. In order to obtain as much as possible stable droplets generation without formation of long filaments and eventually high-quality printed layers, various printing parameters including drop speed V, drop space d, plate temperature Tplate, nozzle temperature Tnuzzle and cleaning cycles/periods tcleaning were examined.
Thickness of piezoelectric P(VDF-TrFE) film sandwiched between two electrodes plays a crucial role on sensitivity of the accelerometers (according to simulation). Besides, each single P(VDF-TrFE) layer contains many defects and porosity. The effect of defects and porosity available in printed P(VDF-TrFE) layer is that when the top electrode is inkjet-printed onto the single P(VDF-TrFE) layer, the silver nanoparticle ink is permeated through the defects and porosity making contact with the bottom electrode and short circuit occurs. To make sure/guarantee full insulation between the bottom and top electrodes, a minimum P(VDF-TrFE) thickness needs to be printed. In this regard, it is required to inkjet print P(VDF-TrFE) solution onto a super flat surface and then do thickness measurements for various printed layers.
For printing of all the patterns, in some cases just one nozzle and in some cases two nozzles were used with a shape of waveform, represented in Fig.5.16, whose parameters were modified to get the as much as possible stable droplets shape (Fig.5.17).

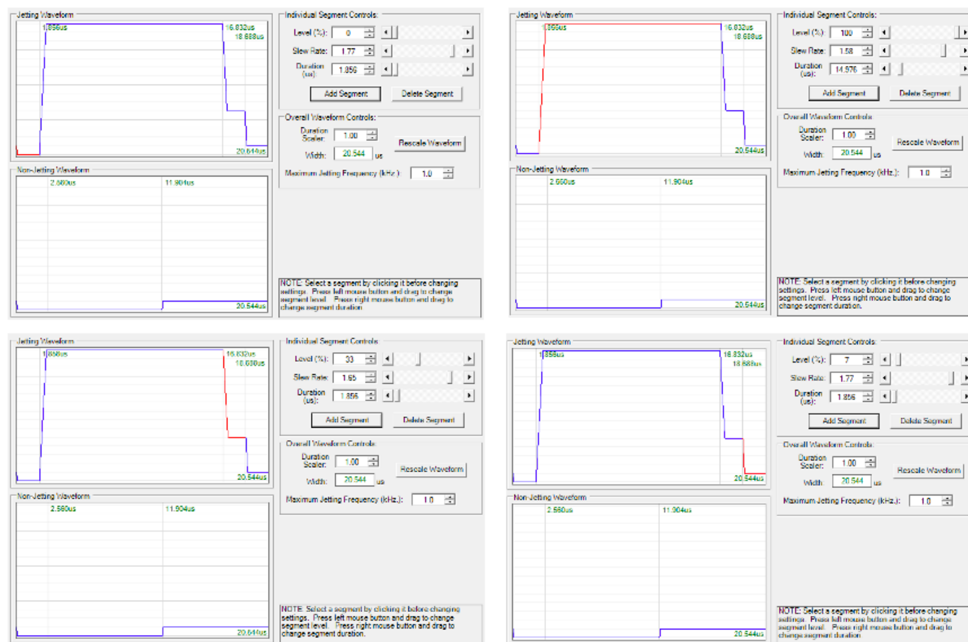

Figure 5.16: Jetting waveform for printing PVDF solution.

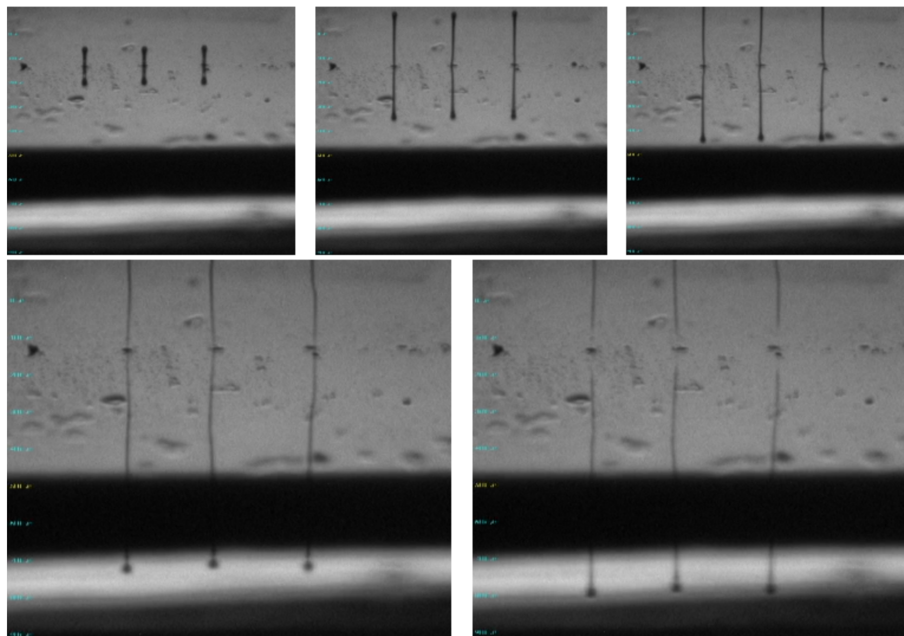

Figure 5.17: Camera views of P(VDF-TrFE) solution droplets.

In order to investigate behavior of P(VDF-TrFE) solution with final purpose which is measuring and evaluating thickness of P(VDF-TrFE) printed films, several different layers were inkjet-printed on super flat surface of Silicon substrates.
To this aim, patterns with different process parameters and conditions inkjet-printed onto the super flat surface. In the first examination, one-layer pattern with one nozzle, drop spacing 20 um, jetting frequency 1KHz, Voltage 40volt and low plate and nuzzle temperature was inkjet-printed onto the gold deposited onto the Silicon film. Images show that low-quality P(VDF-TrFE) layer is obtained in fact not satisfying the requirements of this study.
In order to improve the quality of P(VDF-TrFE) layer printed on Silicon-gold film, the next two examinations were performed to investigate the effect of Voltage, drop spacing, nuzzle and plate temperatures. In this regard, second examination was performed with Voltage 37volt, nozzle temperature Tnozzle= 38 °C and plate temperature Tplate= 60 °C and keeping constant the other process parameters (drop spacing 20 um as the previous case). Images show that reducing/lowering Voltage and increasing plate temperature lead to improvement of quality of P(VDF-TrFE) layer satisfying the requirements of this study.
Then, third examination was performed with drop spacing 10 um and keeping constant other process parameters. Images show that reduced to half drop spacing and high plate temperature lead to achieving high-quality P(VDF-TrFE). However, the only factor/reason not allowing to take into account low drop spacing for the next steps is that using low drop spacing considerably increases the inkjet printing time. so, the printing process parameters, mentioned for pattern n.2, are taken into account for the next steps.
Next steps are performed to check functionality of printhead nozzles during inkjet printing of many different layers meaning for long time printing/working condition. In this regard, in the fourth examination, five-layer pattern with one nozzle, drop spacing 20 um, jetting frequency 1KHz, Voltage 37 volt, nozzle temperature Tnozzle= 38 °C and plate temperature Tplate= 60 °C was inkjet-printed onto the gold deposited onto the Silicon film. Images show that a uniform P(VDF-TrFE) film cannot be obtained after printing 5 layers. It can be justified that printing several layers provides the situation/ provides enough time during which nozzle temperature reaches to plate temperature. Consequently, high nozzle temperature results in solvent evaporation at the nozzles tip leading to nozzles clogging. Therefore, if it is required to employ high plate temperature, cleaning periods must be applied even during inkjet printing of each layer. Hence, fifth examination was performed with applying three cleaning steps between each two layers and keeping constant other process parameters. To compensate the increased printing time due to applying several cleaning steps, two nozzles were activated. Images show a uniform P(VDF-TrFE) film is eventually achieved onto gold deposited onto Silicon film. In the next case, P(VDF-TrFE) solution was inkjet-printed with the same processing parameters but trying to print 25 layers with cleaning timespan 60 sec. It was observed that after printing the >fifth layer, reservoir was empty due to the fact that cleaning step consumes much solution. Therefore, the main challenge is consumption of much solution such that it is not possible to print high number of layers required for the final accelerometer device. In order to solve this challenge, it was supposed to take

advantage of three number of nozzles and just one cleaning cycle during printing.
Hence, 7th and 8th examinations were performed using no cleaning cycle during printing process and one cleaning cycle during printing, respectively, and also using three nuzzles and keeping constant all other parameters as before. Comparing the observed image from morphology of 10-layers printed onto silicon-gold substrate with no cleaning cycle and morphology of 10-layers printed onto silicon-gold substrate with one cleaning cycle, shows that there is no significant difference in uniformity but the problem is that in the case of pattern printed with one cleaning cycle, reservoir was empty upon reaching to 8th layer. So, it was supposed to neglect considering cleaning cycles during printing process. Conversely, in the case of pattern printed with no cleaning cycle, a little bit amount of solution was consumed. Hence, it was decided to consider employing three number of nozzles as a permanent parameter.
9th examination was performed again as similar as the 8th examination but printing 5 layers. Images obtained from fucial camera show that after printing 5 layers, an accumulation was obtained almost in the middle of substrate, so less uniformity is observed on the four corners. Eventually, as final examination, a 10-layers and a 20-layers 2mm*3mm pattern were inkjet-printed. As represented in Fig.5.18 and Fig.5.19, after evaluation of results of characterizations done on PVDF layers over silicon coated with gold, we found out that 10 and 20-layers printed patterns have inhomogeneity such that it is clear that PVDF solution is drawn toward the center such that there is no presence of PVDF solution at the edges of the beam. Actually, as we get closer to center of the beam, concentration of the PVDF solution increases such that thickness in some area is reported to be 3 micrometer (MAX) and in some area 500 nm (MIN) and in average 700-800 nanometer. Fig.5.19. (b). shows that although whole surface area of the sample should have covered by PVDF solution, only 3 mm out of 5 mm of the sample width is covered.

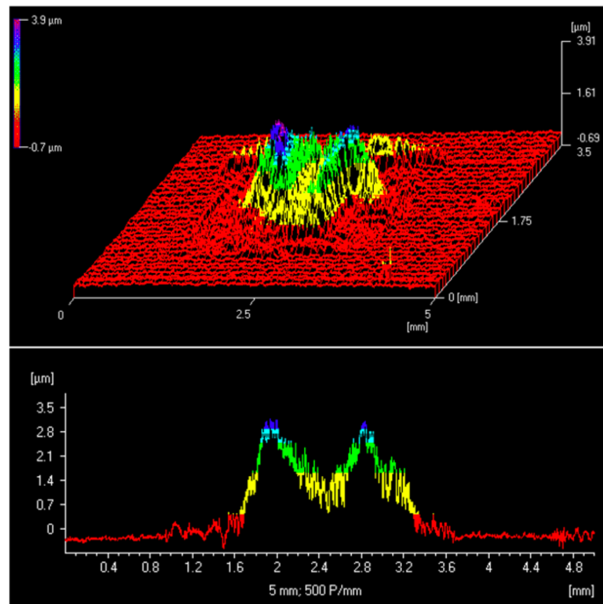

Figure 5.18: Measurements of the thickness, width and length of the P(VDF-TrFE) layer inkjet-printed on silicon-gold substrate after inkjet-printing 10 layers.

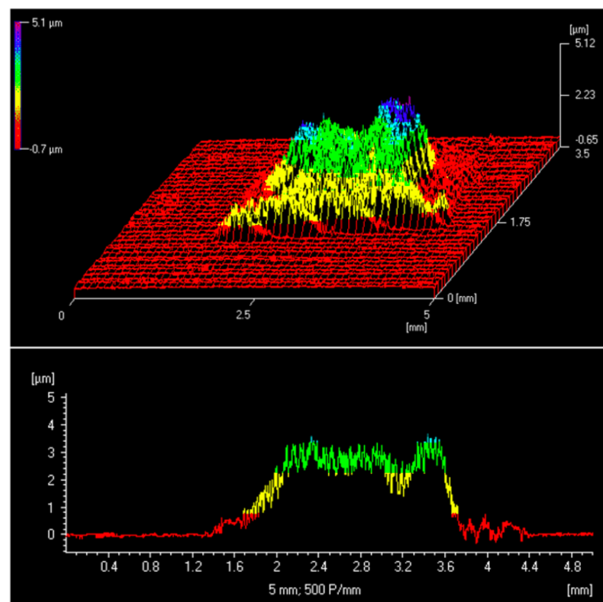

Figure 5.19: Measurements of the thickness, width and length of the P(VDF-TrFE) layer inkjet-printed on silicon-gold substrate after inkjet-printing 20 layers.

To improve this situation, the silicon-gold substrate was substituted with a silicon substrate post-treated by corona treatment and again apply the same conditions and parameters but considering a delay time between printing each layer of P(VDF-TrFE). In this regard, we applied 2 min delaying time and printed again 10 and 20 layers. In this situation, film uniformity is improved.

After thickness measurement of inkjet-printed P(VDF-TrFE) layer, to provide the situation close to final device and investigate the surface morphology of P(VDF-TrFE) layer, it was supposed to inkjet-print P(VDF-TrFE) solution onto already inkjet-printed silver bottom electrode. Then, after curing at 140 °C for one hour and half, morphological assessments of inkjet-printed PVDF- TrFE layer was performed by Scanning Electron Microscope (SEM). Fig.5.20, showing the surface microstructure of the inkjet-printed PVDF-TrFE layers on a printed silver electrode, illustrates that a PVDF-TrFE homogeneous layer with acicular grains (needle-like crystals) is achieved when the layer is sintered at 140 °C for one hour and half. By further investigations of the SEM images, It can be deduced that an acceptable tightly compact fibers are formed for the PVDF-TrFE samples sintered at 140 °C for one hour and half.

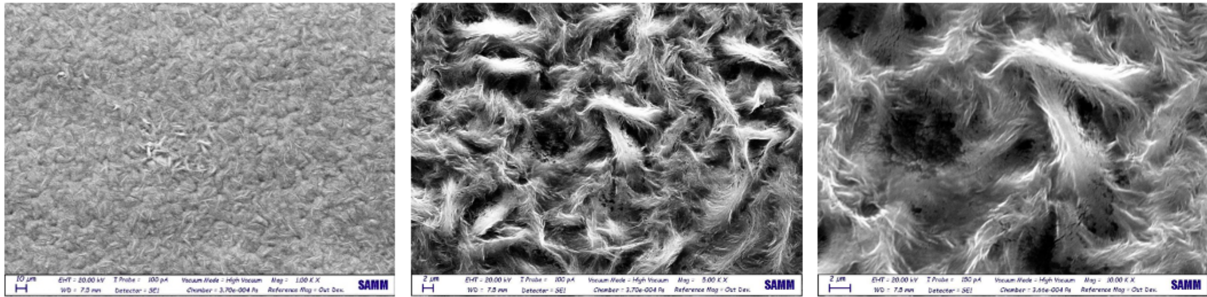

Figure 5.20: Inkjet-printed PVDF-TrFE layer cured at 140 °C for one hour and half.

Getting together all the results obtained from the characterization tests, optimum inkjet printing process parameters and conditions for printing silver bottom electrode, P(VDF-TrFE) film and top silver electrode over beam are achieved.
In the next step, based on the optimum inkjet printing process parameters and conditions obtained from the characterizations tests, a 3-layers bottom silver electrode is inkjet-printed onto the cantilever beam in the dimensions shown in Fig.5.21. The pattern desired to be printed is generated and positioned 1000 um away from the edges of the beam as origin point. The reason why origin point is takenapproximately 1000 um from the edges is referred to the fact that PVDF solution is drawn toward the center such that there is no presence of PVDF solution at the edges of the beam. That is why 1000 um is considered from each side as a safe gap to assure that the whole bottom electrode is covered by the PVDF film and avoid probable short circuit.

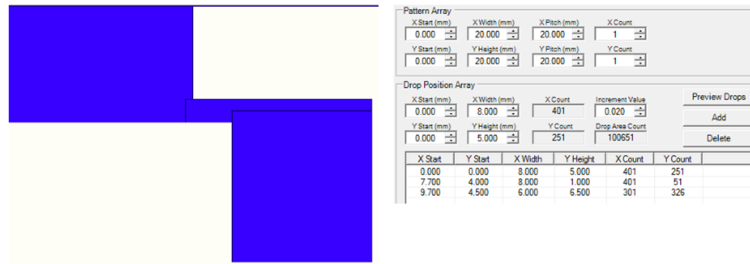

Figure 5.21: Dimensions of 3-layers bottom silver electrode.

Once each layer is inkjet-printed, it is required to wait for at least 30 min to give enough time to the solvent to be evaporated. Then, the bottom silver electrode is annealed in 130 °C temperature with 30 °C/min heating rate for one hour to completely remove the solvent and sinter silver nanoparticles. Then, a 37-layers P(VDF-TrFE) solution with formulation of 0.7wt P(VDF-TrFE) dissolved in the mixture of DMSO (70wt) / MEK (30wt) solvents is inkjet-printed over the bottom electrode. The pattern desired to be printed is generated by and positioned exactly from the beam corner as origin point. Regarding the characterization tests, it is found out that printing 37 layers satisfies the desired thickness considered as Finite Element Analysis (FEA) and also to ensure full insulation between the top and bottom electrodes.

Once each layer is inkjet-printed, it is required to wait for at least 10 min to give enough time to the solvent to be evaporated. Then, the film was annealed in 140 °C temperature with 30 °C/min heating rate for one hour and half to completely remove the solvent.

Finally, a 3-layers top silver electrode is inkjet-printed over the P(VDF-TrFE) film in the dimensions shown in Fig.5.22. The pattern desired to be printed is generated and positioned 1000 um away from the edges of the bottom electrode as origin point. Then, the films were annealed in 130 °C temperature with 30 °C/min heating rate for one hour to completely remove the solvent.

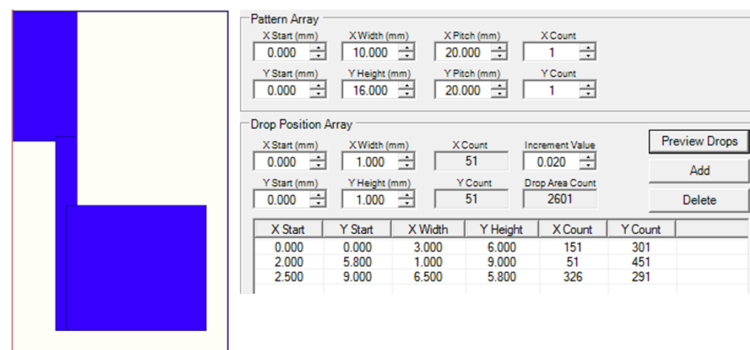

Figure 5.22: Dimensions of 3-layers bottom silver electrode.

In order to characterize the performance of the active layer printed onto the cantilever, it is necessary to measure the electric potential achieved from manual deflection/strain applied manually at the free end of the cantilever beam. Measurements for electric potential are taken with a setup consisting of a resistor and an ampere meter trying to measure the current from a circuit. The passing current was observed but the cantilever broke during the test and nothing was recorded.
After being sure that the whole fabrication process goes on well, we got ready to take further steps towards fabrication of the real device. In this research, Z-axis accelerometer is fabricated based on a 4-layer structure in which all layers are applied on top of each other sequentially. The layers from bottom to top are the substrate, the inkjet-printed bottom silver electrode, the inkjet-printed P(VDF-TrFE) film, and the inkjet-printed top silver electrode. The electrodes are routed to two contact pads at the base where a voltage supply can be connected. The P(VDF-TrFE) film is only applied to the beam region and not to the base, to allow a conductive contact point with the bottom electrode. During inkjet-printing of the functional polymer and the electrodes, two main challenges occurred. First problem/challenge is that during inkjet printing of the three top layers especially inkjet-printing of 37 layers of the functional polymer taking long time, due to very thin thickness of the beam approximately 300 um and reduction of the polymer modulus as a result of temp increase in inkjet printer chamber, the beams are deflected downwards and upwards due to asymmetric connection of the beams to proof mass.
Furthermore, during printing of the functional polymer and the electrodes, it is necessary to increase the temperature up to 60 °C to increase film uniformity and fasten the printing process (solvent evaporation). As a result, we are facing with considerable deflection of the prototype upwards in such a way that after a while the inkjet print head touches the surface and destroy our work (Fig.5.23). Although a working distance (gap between nuzzles of printhead and top surface of the beams) is 1500 um, the inkjet print head touched the surface during the printing process due the fact that. First idea is to increase the working distance but still there are two issues. First of all, substrate made of THERMA DM500 resin is a viscoelastic material that is why during the printing process taking more than four hours, it seems that the polymer transforms from glassy state to rubbery state even at 60 °C which is 40 °C less than its glass transition temp so there is no guarantee that it would not touch the printhead again. Secondly, the more working space increases, the less dimension accuracy is achieved. That is why it was supposed to have a supporter for the device so that we can use it during inkjet-printing and also annealing processes.
As shown in Fig.5.24, we have designed a support acting like a package for the device whereby we could control the device deflection in such a way that to avoid downwards deflection, a negative fixture (bottom supporter) of the Z-axis accelerometer, as shown in Fig.5.24. (a), is designed and fabricated to fix and hold the Z-axis accelerometer in its position without any movement and deflection downwards. The negative fixture is fabricated with Aluminum using Metal CNC milling machine. Furthermore, top supporter was designed and fabricated to avoid upwards deflection of the beam not leading to touch between printhead and surface during inkjet-printing of the functional polymer. Now the question is that why use of top supporter is essential when using top supporter leads to increase of the working

distance? The answer is that top supporter is just employed during inkjet-printing of functional polymer not inkjet printing of the bottom and top electrodes because inkjet-printing of the 3-layer bottom and top electrodes do not take long time and also dimension accuracy of the bottom and top electrodes are very important and essential. However, due to the fact that one the one hand, inkjet printing of the functional polymer takes long time and on the other hand, dimension accuracy of the printed P(VDF-TrFE) film is not essential, working distance can be increased using top supporter.

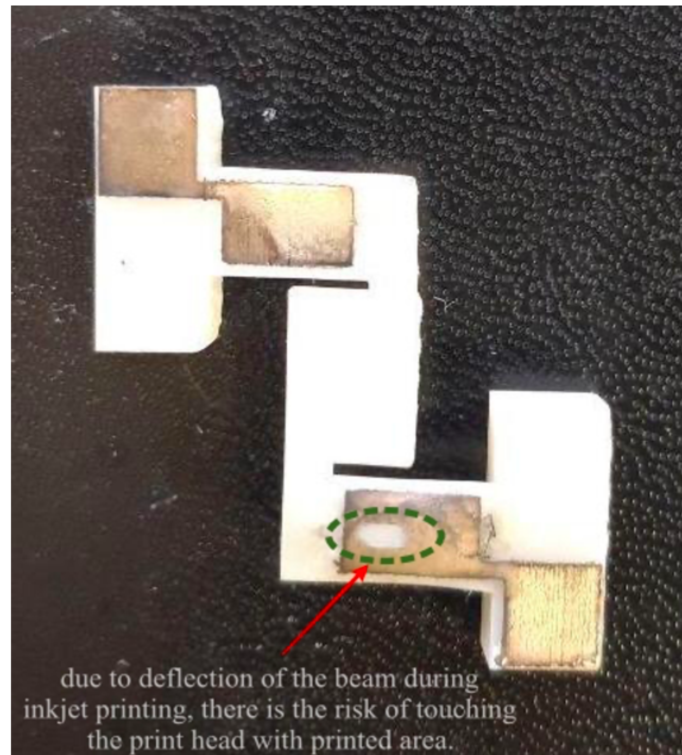

Figure 5.23: Touched area by printhead due to upwards deflection of the beam.

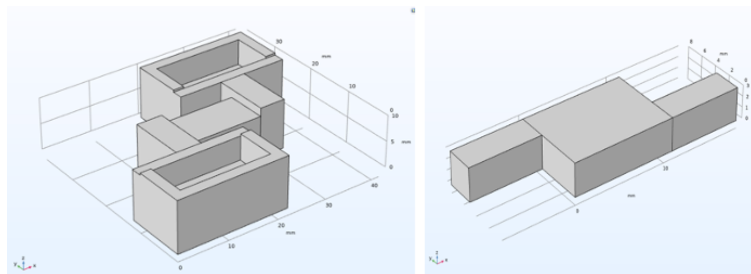

Figure 5.24: a) Bottom supporter (3D view), b) Top holder (3D view)

Another important point needed to be mentioned is that due to presence of a gap approximately 5 mm filled by air between the inkjet-printer plate (Tplate= 60 °C) and beam, solvent evaporation rate is low due to significant temperature difference. Use of the negative fixture, made of Aluminum, can be also useful for heat transfer from the inkjet-printer plate to beam and consequently solvent evaporation. Second problem/challenge is that during printing of the electrodes, there is a very strange area on which silver ink can not be printed. As seen in Fig.5.25, this area is, almost not exactly, located where the beams are connected to the anchor. This area is a straight line crossing the whole length of the anchor with a width of around 200 um. It is necessary to mention that this problem happens just for one beam. Fig.5.25. shows the printed three layers on one of the beams on which that strange area does not appear and the electrode is fully printed; however, shown in Fig.5.25, that strange area appears.

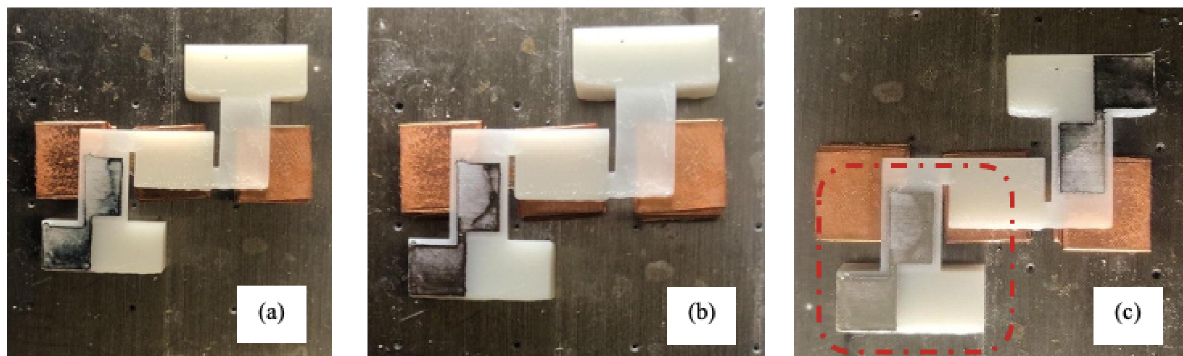

a) printed 1st layer of bottom electrode, b) printed 2nd layer of bottom electrode, c) printed 3rd layer of bottom electrode.

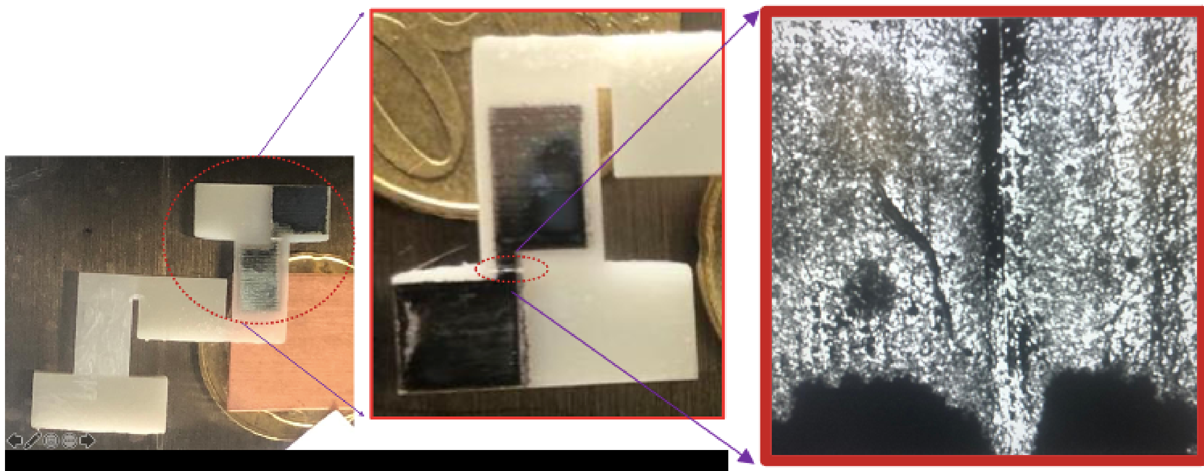

Figure 5.25: Representing strange unpredictable area.

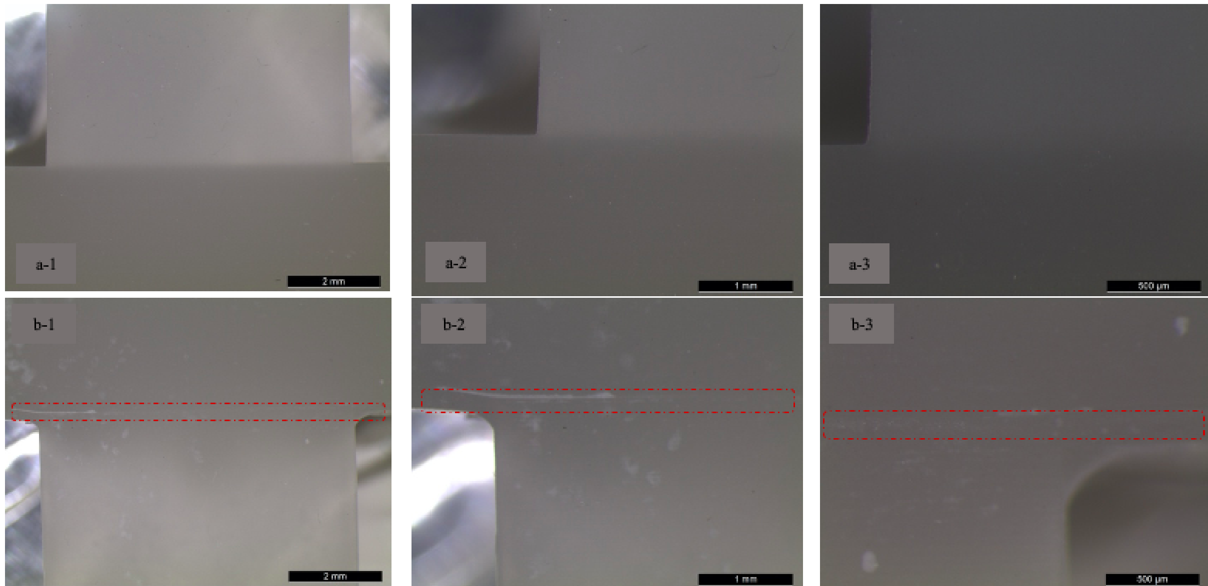

Figure 5.26: a) Beam A without scratch b) Beam B with scratch

We tried to fill this area by increasing the number of layers but surprisingly no material could be deposited on it. This area exists in all prototypes fabricated by SL and located exactly in the same position. This area is parallel with SL layers. We guess, in some of the layers connecting the beams to the anchors something is happening in SL process.

In the following, 3-layer structure in which all layers are applied on top of each other sequentially is explained. 1) Bottom silver electrode: To fabricate the sensor, the first step is to print the bottom electrode over the substrate. The pattern desired to be printed is generated and positioned 1000 um away from the edges of the beam as origin point. To achieve proper coverage, it was observed that after 3 inkjet-printed layers, the inkjet-printed region gets fully covered and shows no sign of the substrate surface and even voids or defects. Once each layer is inkjet-printed, it is required to wait for at least 30 min to give enough time to the solvent to be evaporated (Figs.5.27-5.29). Once all the layers are inkjet-printed, the bottom electrode is dried at 130 °C for one hour to ensure complete solvent evaporation.

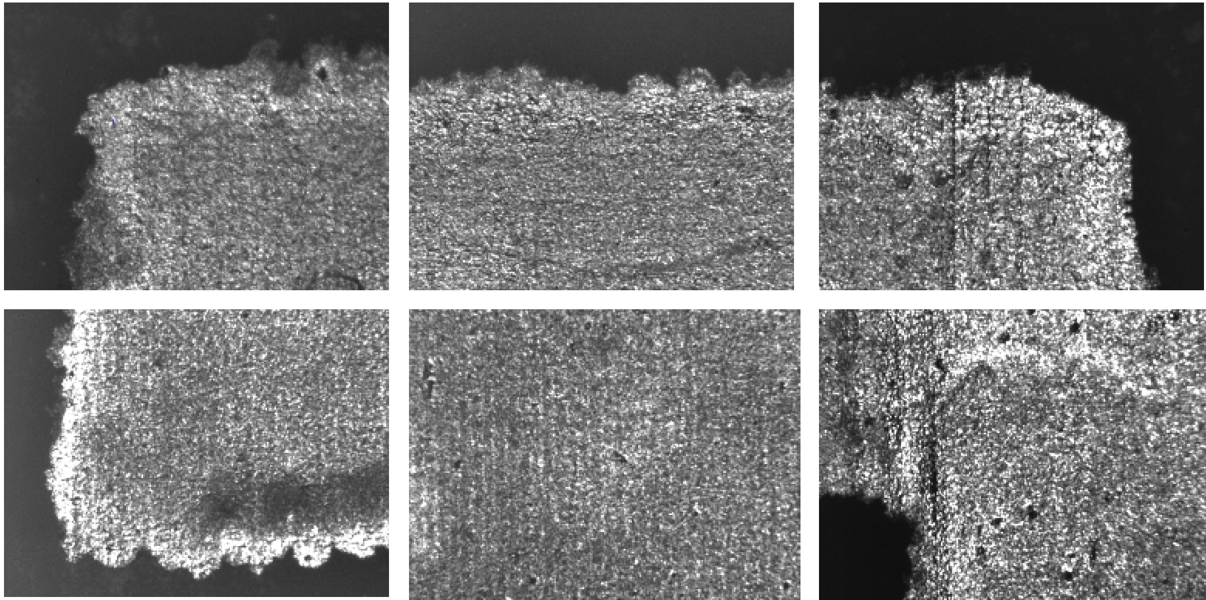

Figure 5.27: Images of the printed first layer of bottom electrode taken by Fucial Camera of Dimatix device.

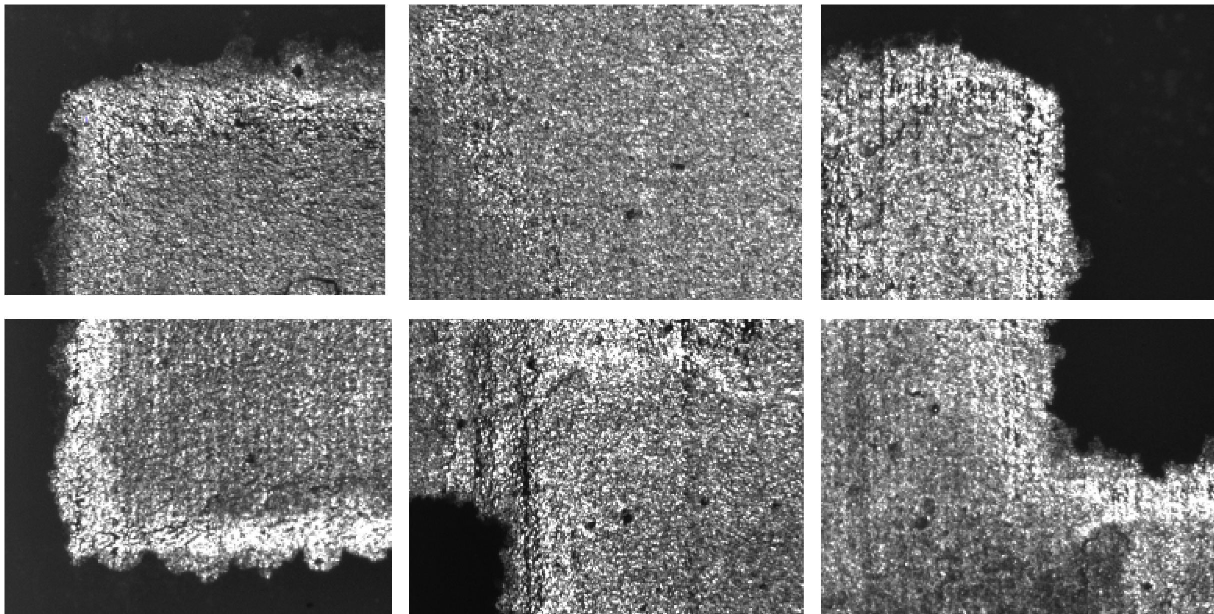

Figure 5.28: Images of the printed second layer of bottom electrode taken by Fucial Camera of Dimatix device.

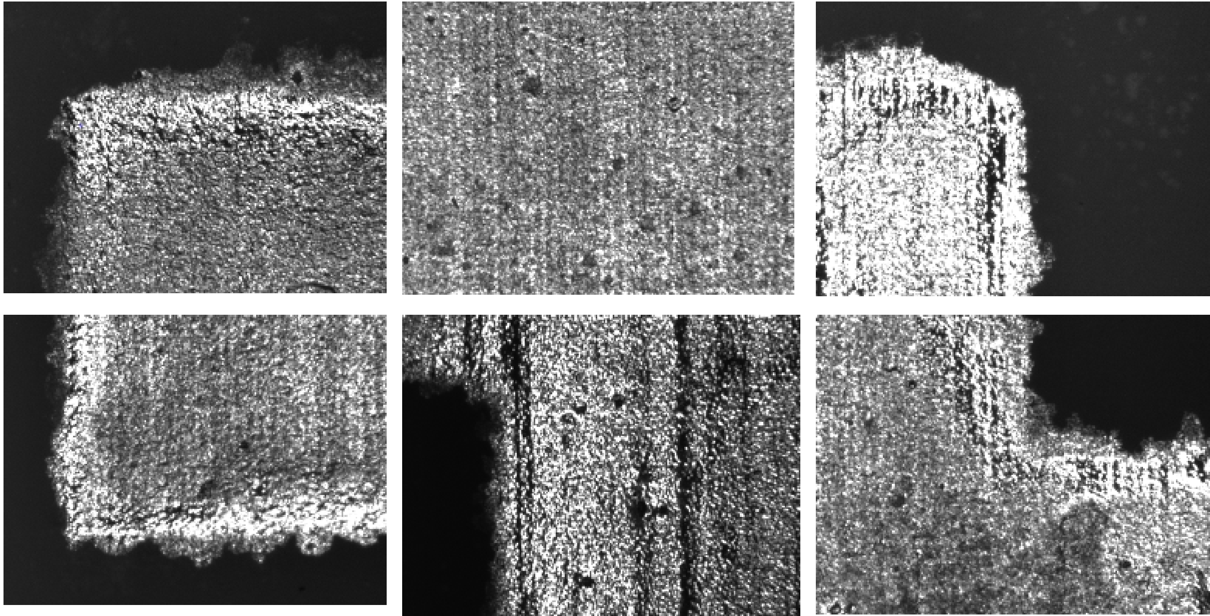

Figure 5.29: Images of the printed third layer of bottom electrode taken by Fucial Camera of Dimatix device.

2) P(VDF-TrFE) film: The next step is to inkjet-print the P(VDF-TrFE) solution with formulation of 0.7wt P(VDF-TrFE) dissolved in the mixture of DMSO (70wt) / MEK (30wt) solvents. The pattern desired to be printed is generated and positioned exactly from the beam corner as origin point. Regarding the characterization tests, it is found out that printing 37 layers satisfies the desired thickness considered as Finite Element Analysis (FEA) and also to ensure full insulation between the top and bottom electrodes. Once each layer is inkjet-printed, it is required to wait for at least 10 min to give enough time to the solvent to be evaporated. Once the desired number of layers have been applied, the device is annealed for one hour and half at 140 °C.

3) Top silver electrode: The third step is to inkjet-print the top silver electrode. The top electrode is inkjet-printed directly onto the dry polymer. The pattern desired to be printed is generated and positioned 1000 um away from the edges of the bottom electrode as origin point. Once the 3-layers top silver electrode have been applied, the device is annealed for one hour at 130 °C.

4) Poling: The final step of preparation is the poling of the active layer. The Z-axis accelerometer beams are connected at their contact pads to a power supply at 140 V and placed on a hot plate at 85 °C. Once the samples reach temperature, the power supply is turned on and the samples are allowed to pole for 20 minutes. After the 20 minutes has elapsed, the hotplate is turned off and the samples are allowed to cool whilst the power supply remains on. When the samples reach ambient temperature, the power supply can be disconnected, and poling is complete.

Chapter 6

CONCLUSION AND FUTURE PROSPECTIVE

As it has been discussed, the fundamental idea of the current project is assessing the possibility of introducing new materials and fabrication technologies to MEMS industry which currently relies mostly on silicon-based batch processing in microelectronic industry. Of the best fabrication processes which could be very beneficial for MEMS, if some restrictions like achievable feature size and surface-related quality also materials availability are overcome in future developments, is additive manufacturing technologies mainly due to the freedom donated to the designers to develop new 3D structures. However not all AM technologies are currently applicable for printing of functional materials as integral part of all MEMS devices in which Sensing/Actuating and generally interaction with the environment is achieved through these materials. Regarding all the studies we did in literature and assessing different possibilities, the idea of fabricating an accelerometer with proper combination of Stereolithography and Inkjet printing bear to our mind. The idea was to print prototypes with stereolithography and then selective addition of functional layers by inkjet printing. The patterning possibility of polymeric piezoelectric materials from a solution led us to more focus on PVDF and its copolymers as a piezopolymer with acceptable electromechanical coefficients which has been sufficiently studied in the literature.

6.1 The Design Procedure

The next step was to introduce suitable designs for one-axis and three axis accelerometers taking into account all the restrictions of stereolithography and inkjet printing. Normally what people think of in designing an accelerometer is somehow connection of some beams to a proof mass to get maximum sensitivity while considering the reliability issues and controlling the total size of the device. In our

case, due to being faced with a piezoelectric polymer with not so high electromechanical coefficient with needed lengthy beams so that we can strain as high as possible the piezo layer, which aimed to be printed on the beams, in order to keep the output signal in the range of MV when the device undergoes an external acceleration. Having lengthy beams induced by the fact that, regarding the stereolithography apparatus in Polimi, fabrication of the beams with thicknesses less than 300 micrometers might be faced with difficulties. So, 300 micrometer thickness for the beams and output electrical signals higher than 1MV were the reference numbers according to which we developed the whole design.

6.1.1 Designing a Cantilever

Before designing the accelerometers, we needed to be sure if our materials selection and fabrication process are reliable enough so that we can apply the same procedure for fabrication of the real device. That is why a cantilever was designed with a beam connected to an anchor. In order to check all the printing parameters, the dimensions of the cantilever beam were assumed to be the same as that of the accelerometer. However also this right selection did not tell us everything and the problems we might encounter during the fabrication of the final device that will be discussed in this chapter.

6.1.2 Z-axis Accelerometer

After running some simulations for some preliminary designs taking into account the electromechanical coefficients reported in the literature for PVDF and other estimated parameters including the density and modulus of polymeric materials, thickness of the films which could be inkjet-printed and so on we understood we have to insert a large proof mass, regarding having 300 micrometer thick beams, or think of beams with length higher than some millimeters to have deflections enough to achieve output signals in MV range. Of course, folded beams are normally used to enhance the proof mass displacement in capacitive accelerometers. However, we required to design flat beams so that functional layers could be inkjet printed on them. Inserting a large proof mass requires significant increase of the dimensions, due to having low density materials, resulting in shift of the vibration mode in Z direction to second or third modes in terms of natural frequencies of the different modes. So, the only way to keep low the natural frequencies was to increase the beams length (to decrease the equivalent stiffness of the beams). In this situation the design prototype size was an issue. That is why we decided to design a device in which the beams are in parallel with the proof mass. In our preliminary design before going to the fabrication process, the beams were connected to the proof mass in a position aligned with the center of mass of the proof mass to control the modes resulted from rotation of the proof mass. Although theoretically this design also was compatible with Dematix inkjet (Of Polimi LAB) we decided to change the position of the beams during the fabrication due to some considerations of inkjet printing process that will be discussed. Also, it is noteworthy to mention that the total dimensions of the device we designed before the beginning of the fabrication procedure were considerably less than those of the device introduce in chapter. inkjet printing process restrictions and materials compatibility, which also will be discussed, lead us to think of a larger device.

6.1.3 Three Axis Accelerometer

In the design stage of the three axis accelerometer addition to the same restrictions of the Z-axis one, there were also other barriers including the possibility of printing of the functional layers on just one side of the beams making it difficult to introduce a proper design for the device to be able to sense the acceleration in three orthogonal directions. However, by the idea of introducing four different beams all around the proof mass and make use of rotational modes, sensing in different directions became possible. Unlike the Z-axis one, the designed three-axis accelerometer has not been fabricated So far. So, the dimensions introduced in chapter 3.1.2.3 are just tuned in such a way that it theoretically could be fabricated although there will be for sure some predicted problems that will be discussed.

6.2 Fabrication Steps

In fabrication steps a procedure to be followed was defined to get the information required and finding the printing parameters applicable to printing of the final device.

6.2.1 Inkjet Printing of the Silver Electrodes

According to the studies in literature that we did on P(VDF-TrFE) which we selected as our piezoelectric polymer, this polymer requires some post treatments after inkjet printing to increase its crystallinity and active its piezoelectric character including annealing and polling. The annealing should be done at temperature more than 130 °C to be effective. This implied use of a high working T resin for printing of the prototypes with Stereolithography. It was bought from Sigma Aldrich. Due to the fact that it was an unknown resin, we had to understand the behavior of silver nanoparticle ink, which we selected as our conductive layer, inkjet printed on the surface of samples fabricated with this new resin. That is why some simple square samples were fabricated with new resin for preliminary tests. After inkjet printing of many patterns of silver nanoparticle ink with different printing parameters on these samples and characterization following conclusion can be made:
1- Considering the type of waveform normally used to print silver ink with Dimatix inkjet printer for the least possible droplet velocity (600m/s), the diameter of each spot on the surface reaches 100 um. Consequently, minimum feature size for electrode is 100um theoretically for an untreated substrate.
2- The surface possesses acceptable wettability for silver ink without any pretreatment like Corona treatment and there is the possibility of very precise electrode pattering.
3- The surface of the samples printed with new resin is super rough due to presence of large silica particles donating it mechanical stability. Having a rough surface possesses its own advantages and disadvantages. Of the advantages of the roughness is increase of the film adhesion to the substrate by mechanical interlocking. However, after annealing which is required to sinter the nanoparticles to form a conductive layer, the film becomes prone to form cracks especially where big particles are present. that is why corona pre-treatment for not so much long time, can decrease the film susceptibility by increasing the uniformity of the film avoiding the accumulation of the material locally.

4- Three layers of silver ink is enough for complete covering of the surface.

6.2.2 Inkjet Printing of the Piezoelectric Polymer

Generally, inkjet printing of the soluble polymers is faced with many difficulties due to complex rheological behavior of the inks containing polymer. According to the literature studies, the best type of waveform for inkjet printing compatible with rheological behavior of polymer-containing inks is the one introduced in Fig.5.16 although it depends also the type of the solvent. The solvent we used for printing of PVDF is a mixture of DMSO (70w) and MEK (30w) which is more compatible with Dimatix inkjet printer. According to our experience and characterizations we did, there are some points which should be considered during printing of this polymer:
1- The most important parameters which should be considered to have stable nozzles during printing with Dimatix inkjet printer are:
1-1: Printing frequency: So straight forward, it should be mention that there is not any possibility to have a fast printing and the printing frequency should be adjusted to less than 2KHz to have stable nozzles.
1-2: Nozzle temperature: For the type the ink we used the optimum value for the nozzle temperature to have stable nozzles and rounded droplets is something around 40 °C. Increase of nozzle temperature leads evaporation of the solvent at nozzle tip so clogging the nozzle. However, keeping the nozzle temperature in this range is of difficulties. If we prefer to have a fast solvent evaporation on the surface, which is the case to also increase the film uniformity, the plate temperature should be at it its maximum value which is 60 °C for Dimatix. Due to very close distance of the printhead with plate, the nozzles are heated up during printing and they do not assume the tuned temperature. One of the ways to avoid this problem is to run some cleaning cycles during printing or use of interlayer delays which consequently bring about the drawbacks of more ink consumption and increase of printing process time considerably. The other way is not to run many printing cycles but increasing the working distance to higher values to enhance the distance of the print-head with plate. For sure, it leads to loss of printing precision but considering the fact that we have an insulating material, it may not bring about any problem in case of proper designs.
1-3: The actuation voltage: It should not be reduced to values less than 35V although the droplet velocity exceeds its optimum range (600-1000 m/s) otherwise the nozzles get clogged after printing of some layers.
2- With the type of ink and printing parameters we used for each 10 layers, 700 nm of piezoelectric polymer is deposited. So, depending on the design, the number of printed layers should be tuned accordingly.
3- Using our solvent, the uniformity of the films on metallic surfaces is not satisfactory. However, it can be improved in such a way that by some considerations, the process is applicable to the fabrication of the final device. These considerations will be discussed in the final subchapter of the project prospective.

6.3 Prospective of the Project

Regarding the experiences of this project either in the design stage or in fabrication process, if a device is aimed to be designed and manufactured with almost the same idea of this project, some general attentions should be taken:
1- With this new resin, all the structures should be printed vertically using Stereolithography otherwise a lot of imperfections would appear on the surface.
2- During printing of the silver electrodes on the material printed with the new resin, at least 10 min of interlayer delay should be considered in order not to lose the uniformity of the film. The interlayer delay should be enhanced if thickness of the substrate is higher than 3mm.
3- Using the ink we developed for this project not so uniform film could be obtained if the ink is printed on metallic substrates. In order to improve film uniformity, PVDF pattern dimensions should be designed in such a way that at least 1mm distance between PVDF pattern and metallic one from each side is assumed so that the PVDF ink is trapped in to the roughness of the surface and is not accumulated at the center of the metallic film. This issue leads to increase of the size of the device considerably in order to avoid short circuits. One of the most important suggestion for future works is trying to develop a solvent more compatible with metallic electrodes are improving film uniformity by changing the printing parameters like droplet spacing whose value in our work was 20 um.
4- Before fabrication of any device, complete characterization of the printed piezoelectric films in terms of electromechanical coefficients should be done for various printing parameters and post processing including the annealing temperature.
5- Structures printed with this new resin encounters with considerable deflections during inkjet printing process and also post processing in which the temperature exceeds 100 °C. in order to control such deflections designing some support structures like a package is suggested.

Bibliography

1. Narasimhan, V., H. Li, and M. Jianmin, Micromachined high-g accelerometers: a review. Journal of Micromechanics and Microengineering, 2015. 25(3): p. 033001.
2. X. Wang, W. Xu, H. Luo and Y. Lee, "Theoretical Modeling, Numerical Simulations and Experimental Study of Micro Thermal Convective Accelerometers," in Journal of Microelectromechanical Systems, vol. 28, no. 5, pp. 790-798, Oct. 2019, doi: 10.1109/JMEMS.2019.2930065.
3. Biswas, S. and A.K. Gogoi. Design and simulation of piezoresistive MEMS accelerometer for the detection of pathological tremor. in IEEE SOUTHEASTCON 2014. 2014. IEEE.
4. Gomathi, T. and S.M. Shaby. Capacitive accelerometers for microelectromechanical applications: A review. in 2016 International Conference on Control, Instrumentation, Communication and Computational Technologies (ICCICCT). 2016. IEEE.
5. Hollocher, D., et al. A very low cost, 3-axis, MEMS accelerometer for consumer applications. in SENSORS, 2009 IEEE. 2009. IEEE.
6. Tez, S., et al., A bulk-micromachined three-axis capacitive MEMS accelerometer on a single die. Journal of Microelectromechanical Systems, 2015. 24(5): p. 1264-1274.
7. Biswas, K., S. Sen, and P.K. Dutta, MEMS capacitive accelerometers. Sensor Letters, 2007. 5(3-4): p. 471-484.
8. Alabqari, A. and B. Majlis. Electrostatic pull-in behavior in 50g force balanced MEMS accelerometer. in 2004 IEEE International Conference on Semiconductor Electronics. 2004. IEEE.
9. Tsuchiya, T. and H. Funabashi, A z-axis differential capacitive SOI accelerometer with vertical comb electrodes. Sensors and Actuators A: Physical, 2004. 116(3): p. 378-383.
10. Adams, T.M. and R.A. Layton, Piezoresistive transducers, in Introductory MEMS: Fabrication and Applications. 2010, Springer US: Boston, MA. p. 211-230.
11. Khir, M.H.M., P. Qu, and H. Qu, A low-cost CMOS-MEMS piezoresistive accelerometer with large proof mass. Sensors, 2011. 11(8): p. 7892-7907.
12. Kavitha, S., R.J. Daniel, and K. Sumangala, A simple analytical design approach based on computer aided analysis of bulk micromachined piezoresistive MEMS accelerometer for concrete SHM applications. Measurement, 2013. 46(9): p. 3372-3388.
13. Amarasinghe, R., et al., Development of miniaturized 6-axis accelerometer utilizing piezoresistive sensing elements. Sensors and Actuators A: Physical, 2007. 134(2): p. 310-320.
14. Sankar, A.R., S. Lahiri, and S. Das, Performance enhancement of a silicon MEMS piezoresistive

single axis accelerometer with electroplated gold on a proof mass. Journal of Micromechanics and Microengineering, 2009. 19(2): p. 025008.
15. Atwell, A.R., et al., Simulation, fabrication and testing of bulk micromachined 6H-SiC high-g piezoresistive accelerometers. Sensors and Actuators A: Physical, 2003. 104(1): p. 11-18. 16. Jiang, L. and R. Cheung, A review of silicon carbide development in MEMS applications. International Journal of Computational Materials Science and Surface Engineering, 2009. 2(3-4): p. 227-242.
17. Tadigadapa, S. and K. Mateti, Piezoelectric MEMS sensors: state-of-the-art and perspectives. Measurement Science and technology, 2009. 20(9): p. 092001.
18. Rosen, C., B.V. Hiremath, and R. Newnham, Piezoelectricity. 1992: Springer Science and Business Media.
19. Bauer, S. and F. Bauer, Piezoelectric polymers and their applications, in Piezoelectricity. 2008, Springer. p. 157-177.
20. Zhang, Q., V. Bharti, and X. Zhao, Giant electrostriction and relaxor ferroelectric behavior in electron-irradiated poly (vinylidene fluoride-trifluoroethylene) copolymer. Science, 1998. 280(5372): p. 2101-2104.
21. Bauer, F., Review on the properties of the ferrorelaxor polymers and some new recent developments. Applied Physics A, 2012. 107(3): p. 567-573.
22. Furukawa, T., Phase Transition 18 (1989) 143. Crossref.
23. Underwood, S. and P. Mulvaney, Effect of the solution refractive index on the color of gold colloids. Langmuir, 1994. 10(10): p. 3427-3430.
24. Petchsuk, A., Ferroelectric terpolymers, based on semicrystalline VDF/TRFE/CHLORO-containing termonomers: synthesis, electrical properties, and functionalization reactions. 2003.
25. Wegener, M. and S. Bauer, Microstorms in cellular polymers: A route to soft piezoelectric transducer materials with engineered macroscopic dipoles. ChemPhysChem, 2005. 6(6): p. 1014-1025.
26. Gerhard-Multhaupt, R., Less can be more. Holes in polymers lead to a new paradigm of piezoelectric materials for electret transducers. IEEE Transactions on Dielectrics and Electrical Insulation, 2002. 9(5): p. 850-859.
27. Lindner, M., et al., Charged cellular polymers with" ferroelectretic" behavior. IEEE Transactions on Dielectrics and Electrical Insulation, 2004. 11(2): p. 255-263.
28. Zhang, X., G.M. Sessler, and J. Hillenbrand, Improvement of piezoelectric coefficient of cellular polypropylene films by repeated expansions. Journal of electrostatics, 2007. 65(2): p. 94-100.
29. Zhang, X., J. Hillenbrand, and G.M. Sessler, Piezoelectric d 33 coefficient of cellular polypropylene subjected to expansion by pressure treatment. Applied physics letters, 2004. 85(7): p. 1226-1228.
30. Janas, V.F. and A. Safari, Overview of fineâscale piezoelectric ceramic-polymer composite processing. Journal of the American Ceramic Society, 1995. 78(11): p. 2945-2955.
31. Liu, Z., et al., Piezoelectric properties of PVDF/MWCNT nanofiber using near-field electrospinning. Sensors and Actuators A: Physical, 2013. 193: p. 13-24.
32. Arlt, K. and M. Wegener, Piezoelectric PZT/PVDF-copolymer 0-3 composites: aspects on film preparation and electrical poling. IEEE Transactions on Dielectrics and Electrical Insulation, 2010.

17(4): p. 1178-1184.
33. Hou, D., et al., Preparation and properties of PVDF composite hollow fiber membranes for desalination through direct contact membrane distillation. Journal of membrane science, 2012. 405: p. 185-200.
34. Ramadan, K.S., D. Sameoto, and S. Evoy, A review of piezoelectric polymers as functional materials for electromechanical transducers. Smart Materials and Structures, 2014. 23(3): p. 033001.
35. Graz, I., et al., Flexible active-matrix cells with selectively poled bifunctional polymer-ceramic nanocomposite for pressure and temperature sensing skin. Journal of Applied Physics, 2009. 106(3): p. 034503.
36. Chen, A., et al. Flexible tactile sensors based on nanoimprinted sub-20 NM piezoelectric copolymer nanograss films. in SENSORS, 2012 IEEE. 2012. IEEE.
37. Dahiya, R.S., et al., Towards tactile sensing system on chip for robotic applications. IEEE Sensors Journal, 2011. 11(12): p. 3216-3226.
38. Yuji, J.-i. and C. Sonoda. A PVDF tactile sensor for static contact force and contact temperature. in SENSORS, 2006 IEEE. 2006. IEEE.
39. Schulze, R., et al. Integration of piezoelectric polymer transducers into microsystems for sensing applications. in Proceedings of ISAF-ECAPD-PFM 2012. 2012. IEEE.
40. Jung, I., et al., Flexible piezoelectric polymer-based energy harvesting system for roadway applications. Applied energy, 2017. 197: p. 222-229.
41. Leung, A.M., et al. Micromachined accelerometer with no proof mass. in International Electron Devices Meeting. IEDM Technical Digest. 1997. IEEE.
42. Mukherjee, R., et al., A review of micromachined thermal accelerometers. Journal of Micromechanics and Microengineering, 2017. 27(12): p. 123002.
43. Garraud, A., et al., Frequency response analysis of an accelerometer based on thermal convection. Journal of Micromechanics and Microengineering, 2011. 21(3): p. 035017.
44. Kruth, J.-P., M.-C. Leu, and T. Nakagawa, Progress in additive manufacturing and rapid prototyping. CIRP Annals-Manufacturing Technology, 1998. 47(2): p. 525-540.
45. Huang, S.H., et al., Additive manufacturing and its societal impact: a literature review. The International Journal of Advanced Manufacturing Technology, 2013. 67(5-8): p. 1191-1203.
46. Vaezi, M., H. Seitz, and S. Yang, A review on 3D micro-additive manufacturing technologies. The International Journal of Advanced Manufacturing Technology, 2013. 67(5-8): p. 1721-1754.
47. Melchels, F.P., J. Feijen, and D.W. Grijpma, A review on stereolithography and its applications in biomedical engineering. Biomaterials, 2010. 31(24): p. 6121-6130.
48. Wong, K.V. and A. Hernandez, A review of additive manufacturing. International scholarly research notices, 2012. 2012.
49. Ikuta, K., S. Maruo, and S. Kojima. New micro stereo lithography for freely movable 3D micro structure-super IH process with submicron resolution. in Proceedings MEMS 98. IEEE. Eleventh Annual International Workshop on Micro Electro Mechanical Systems. An Investigation of Micro Structures, Sensors, Actuators, Machines and Systems (Cat. No. 98CH36176. 1998. IEEE.

50. Bertsch, A., J. Jezequel, and J. Andre, Study of the spatial resolution of a new 3D microfabrication process: the microstereophotolithography using a dynamic mask-generator technique. Journal of Photochemistry and Photobiology A: Chemistry, 1997. 107(1-3): p. 275-281.
51. Maruo, S. and S. Kawata, Two-photon-absorbed near-infrared photopolymerization for three-dimensional microfabrication. Journal of microelectromechanical systems, 1998. 7(4): p. 411-415.
52. Cummins, G. and M.P. Desmulliez, Inkjet printing of conductive materials: a review. Circuit world, 2012.
53. Hoath, S.D., Fundamentals of inkjet printing: the science of inkjet and droplets. 2016: John Wiley and Sons.
54. Ru, C., et al., A review of non-contact micro-and nano-printing technologies. Journal of Micromechanics and Microengineering, 2014. 24(5): p. 053001.
55. Haque, Rubaiyet Iftekharul, et al. Inkjet printing of high molecular weight PVDF-TrFE for flexible electronics. Flexible and Printed Electronics 1.1 (2015): 015001.
56. Mehdi Rezaeisaray, Mohamed El Gowini, Dan Sameoto, Don Raboud, Walied Moussa. Low frequency piezoelectric energy harvesting at multi vibration mode shapes. Sensors and Actuators A: Physical, Volume 228, 2015, Pages 104-111, https://doi.org/10.1016/j.sna.2015.02.036.